2023-05-01

Connectional analysis of brain regions associated with feeding

Kenichiro Negishi
University of Texas at El Paso

CONNECTIONAL ANALYSIS OF BRAIN REGIONS ASSOCIATED WITH FEEDING

KENICHIRO NEGISHI

Doctoral Program in Biosciences

APPROVED:

Arshad M. Khan, Ph.D., Chair

Bruce S. Cushing, Ph.D.

Andrew M. Poulos, Ph.D.

Edward Castañeda, Ph.D.

Manuel Miranda-Arango, Ph.D., Advocate

Stephen Crites, Ph.D.
Dean of the Graduate School & Associate Provost for Graduate Studies

Dedications

To my mates

CONNECTIONAL ANALYSIS OF BRAIN REGIONS ASSOCIATED WITH FEEDING

by

KENICHIRO NEGISHI, M.S.

DISSERTATION

Presented to the Faculty of the Graduate School of
The University of Texas at El Paso
in Partial Fulfillment
of the Requirements
for the Degree of

DOCTOR OF PHILOSOPHY

Department of Biological Sciences
THE UNIVERSITY OF TEXAS AT EL PASO
May 2023

Abstract of the Dissertation

Rodent models are invaluable for understanding the foundations of motivated behaviors. One major obstacle faced by these efforts is the lack of a 'wiring diagram' or a 'parts list' of structures that support motivated behaviors. Here, I present work that advances our knowledge of the structural organization of connections and chemoarchitecture of the diencephalon. Chapter 1 aims to clarify a wiring diagram of the medial prefrontal cortex (mPFC) following a recent demonstration of cortically-evoked feeding through this region. Chapter 2 clarifies the distributions of a subpopulation of tyrosine hydroxylase (TH) neurons in the hypothalamus. These disparate datasets were analyzed and interpreted using a Nissl-based mapping approach and nomenclature system that facilitates construction of a spatial model for motivated behaviors. Using this methodology, I describe widespread and topographically organized reciprocal connectivity between mPFC and thalamus as well as subregion-specific connectivity with the hypothalamus. I also demonstrate heterogeneity among hypothalamic TH neurons on the basis of their co-expression of the vesicular GABA transporter. Taken together, this work describes a general principle of mPFC connections with thalamus that has been overlooked, and it contributes important insights toward a comprehensive wiring diagram and parts list for feeding and other motivated behaviors.

Table of Contents

List of Tables

List of Figures

General Introduction

Motivated behaviors unfold as discrete and unitary sets of actions with clear goals. They can be neatly sorted into acquisition, consummatory, and termination phases. However, their underlying anatomy is far from clear or unitary and is a matter of vigorous debate (Watts et al., 2022). Ingestive behaviors are of particular importance because advances in our understanding have an immediate bearing on disorders related to weight regulation. Ingestive behaviors are also supported by the limbic system (MacLean, 1952), which coordinates affective and motivational contributions to foraging and the decision to eat. In the context of substance use disorders, it is difficult to escape the similarities in behaviors and neural circuitry engaged by addictive drugs and food as natural reward. Indeed, both fields tend to be mutually informative (Kelley and Berridge, 2002; Volkow and Wise, 2005). Therefore, a better understanding of the anatomy that supports feeding is of broader interest. The overall goal of this work is to provide strategies and insights toward a ‘wiring diagram’ of brain regions that drive feeding.

This dissertation will elaborate on two major research objectives of the Khan lab. The first aim is to describe the input and output connections of gray matter regions implicated in feeding, and the second aims to provide a structural account of the diverse cast of neurochemically-defined cell types in the hypothalamus. Both research directions examine elements of a ‘wiring diagram’ (nodes and edges) that are not always examined simultaneously. Part of my aim is to explore whether a Nissl-based atlas mapping strategy is suitable for combining these disparate datasets. I will provide an introduction to these topics with an emphasis on atlas-based mapping, as it is the unifying thread in the works presented.

Nissl-based mapping and standardized atlases

How do we define brain regions? Neuroscience, from the outset, has put forth many

answers to this question and the answers themselves evolved in parallel to technological and methodological advances in science. One enduring strategy, best exemplified by the works of neurologists Korbinian Brodmann (1909) and Elisha S. Gurdjian (1927), makes use of the Nissl stain to define brain regions. White matter and Golgi stains were also profitable for describing white matter tracts and inferring inter-regional connectivity (Millhouse, 1969). Later developments introduced histochemical enzymatic reactions, such as the acetylcholinesterase reaction, as an additional strategy for identifying brain regions. I have had success with performing some of these stains and I observe the same brain structures and features described by Brodmann or Gurdjian with remarkable regularity (**Figure 1**).

It is not surprising that the Nissl stain is a central part of standardized brain atlases produced a century later (Paxinos and Watson, 2014; Swanson, 2018). Nissl-defined structures occur with such regularity that we can devise stereotaxic coordinates that boast

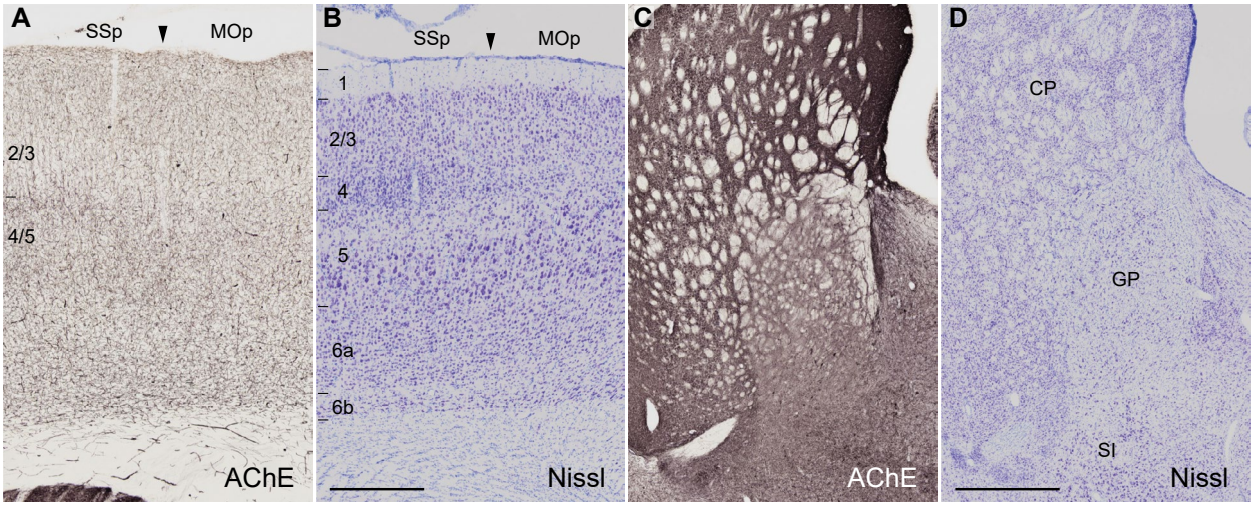

Figure 1. Histological identification of brain regions. Photomicrographs showing comparisons of brain structures identified with acetylcholinesterase (AChE) histochemistry (**A**, **C**) and the Nissl stain (**B**, **D**). In cortex, AChE is capable of distinguishing superficial and deep layers (A) whereas the Nissl stain allows clear identification of each layer (B). (C) shows that AChE staining can clearly resolve the boundary between the caudate-putamen (CP) and globus pallidus (GP) whereas this can be challenging with a Nissl stain alone (D). However, other boundaries, such as that separating the GP from the substantia innominata (SI) cannot be clearly identified. Scalebars: 500 µm in (A) and (B); 1 mm in (C) and (D). Abbreviations: Primary motor cortex (MOp); primary somatosensory cortex (SSp).

sub-millimeter precision for their experimental targeting (Paxinos and Watson, 2014). This advantage is also reflected by an increasing reliance on Nissl-based methods for reporting probe locations from functional experiments (Khan, 2013). Thus, analysis of cytoarchitecture has earned its position as the gold standard for anatomical localization and identification of brain regions. It may be surprising, then, to observe a shift away from these methods in recent years. It is worth clarifying some reasons for this shift in order to justify my commitment to Nissl-based mapping.

Beginning with the obvious, Nissl interpretation is challenging and time-consuming. Nissl interpretation is a hard-won skill, like those demanded for bird watching or aural identification of melodic and harmonic intervals. My experience teaching this skill to undergraduate and graduate students convinced me that fluency is only achieved after years of guided practice. Even at the expert level, informally assessed with Khan lab members and correspondence with the Swanson lab (R. H. Thompson and J. D. Hahn), boundary identification can take between 10 and 30 minutes for a single section. Faced with these technical hurdles, alternative strategies that involve automated atlas registration or neurochemical markers can have tremendous appeal.

Alternative standard atlases

The Allen Institute has led the development and application of atlas technologies in a multitude of ways. Most important for our discussion is the recently introduced Common Coordinate Framework (CCF) (Wang et al., 2020) that is widely used for automated atlas registration and high-throughput analysis of large datasets. This has become the method of choice for three-dimensional datasets gathered using light sheet microscopy or two-photon tomography (Madangopal et al., 2022). Automated registration to CCF can also be applied to image datasets (Wang et al., 2020), so it is worth understanding how the atlas was constructed and how it differs from traditional Nissl- and histochemistry-based atlases.

The CCF atlas template, in contrast to other atlases, was constructed by aligning

and averaging autofluorescence signals from thousands of mouse brains (Lein et al., 2007; Oh et al., 2014; Wang et al., 2020). An average template was constructed with a reported isotropic voxel resolution of 10 μm. Autofluorescence signal from the template allows some detection of boundaries, particularly in regions that are characterized by the differential presence of white matter. The vast majority of brain regions cannot be identified using the template, but each voxel was nonetheless assigned to a single brain structure. This was achieved by consulting the Allen Institute's impressive collection of gene expression (in situ hybridization and transgenic reporters), connectional, and Nissl data so that expert anatomists could make informed guesses about boundary locations. Nonetheless, the CCF is a monumental contribution that will continue to be used for high-throughput analysis of volumetric and image data.

The atlas registration problem: Inductive and deductive strategies

Let us predict that brain research will continue to move towards large datasets collected using light sheet microscopy, serial-tomography, or similar inventions. This requires rapid and large-scale atlas registration, meaning automated strategies will be overwhelmingly favored in place of slower Nissl-based registration used here. In my efforts to conceptualize both strategies, I realized we could draw from the philosophy of logic to understand atlas registration as either inductive or deductive processes. Framing it this way is powerful because all distinctions and implications of inductive vs. deductive reasoning can be applied equally to determine which strategy is appropriate for a given scientific goal. I will briefly describe both forms of atlas registration to clarify my reasons for choosing Nissl-based registration.

Deduction-based atlas registration. Deduction-based registration is a top-down strategy which applies a theoretical starting point, such as an atlas model, to form conclusions about boundary conditions in an experimental sample. Deduction-based

registration will always form the argument structure “if [p, q, r], then regional boundaries are as such.” The antecedents can be composed of landmarks such as brain and ventricular surfaces, white matter tracts, autofluorescence, or objectively defined anchor points. Once alignment is satisfied, all additional features (boundaries, stereotaxic coordinates, etc) are assumed to be coextensive.

There are certainly hazards to ‘copy-pasting’ atlas boundaries, but the accuracy of deduced boundaries improves with the quality and number of the antecedents. That is, using brain surfaces alone can be disastrous while alignment using white matter and well-defined anchor points can be highly effective (Hintiryan et al., 2016).

Induction-based atlas registration. Induction-based atlas registration is a bottom-up strategy and an inversion of the deductive approach. Here, the experimenter uses direct observation to identify boundaries on each sample to form conclusions at the theoretical level (standard atlas).

Induction-based registration is much more time-consuming because it involves constructing a bespoke atlas for every sample (Barbier et al., 2018). The advantage is that boundaries and conclusions are as accurate as the observation methods allow. For this reason, inductive methods are a long-standing preference for anatomists and there are well-documented practices we can observe to achieve rigorous outcomes (Simmons and Swanson, 2009).

Reasons to combine deductive and inductive strategies. Although both types of registration are mutually exclusive, we should aim to use them in complementary ways. Deductive strategies are best represented by atlas registration softwares such as the open-source ClearMap pipeline (Renier et al., 2016; Kirst et al., 2020) that is used for whole-brain volumetric analysis. This strategy is ideal for a rapid survey of brain volumes, but the outcome or insights are often beyond scrutiny. Beyond the resource-demanding

nature of these techniques, the anatomical renderings are not always convincing. Misregistered features are easy to spot in research articles, even in those published by the Allen Institute (in the worst instance, axons were seen registered outside the brain itself). It is not clear whether deduction-based strategies can be used to meaningfully assess other deduction-based strategies, the outcome is likely to reflect differences between pipelines themselves. Far from dismissing these findings, I would simply encourage using an inductive registration strategy or separate experiments to support key findings generated by the black box.

Insights that prompt refinements to analytical pipelines and standard atlases themselves are only gained with inductive registration methods. That is, because deductive registration by definition begins by asserting the theoretical validity of its framework. Inductive registration, by contrast, begins by asserting the validity of the observations. Mapping shown in my work begins by making observations on Nissl stained and immunolabeled samples. If these observations are taken to be valid, then they are used to make conclusions about our theoretical models (atlas boundaries or wiring diagrams), usually as mapped representations.

The strength of induction-based registration is demonstrated several times in Chapters 1 and 2, but one example can be introduced here. In the zona incerta (ZI), both Swanson and the Allen Reference Atlas (Dong, 2008) describe a conspicuous small cluster observed in Nissl preparations that they term the ZI “dopaminergic group” (ZIda; **Figure 2**). Upon alignment with sections containing immunolabeled tyrosine hydroxylase (TH), it becomes clear that the “ZIda” is in fact avoided by TH neurons. This insight, in addition to challenging nomenclature in standard atlases, introduces a novel question regarding the identity of this small neuronal cluster. A top-down deductive strategy would have simply asserted that the TH neurons are where they should be, and no new insights would have been gained.

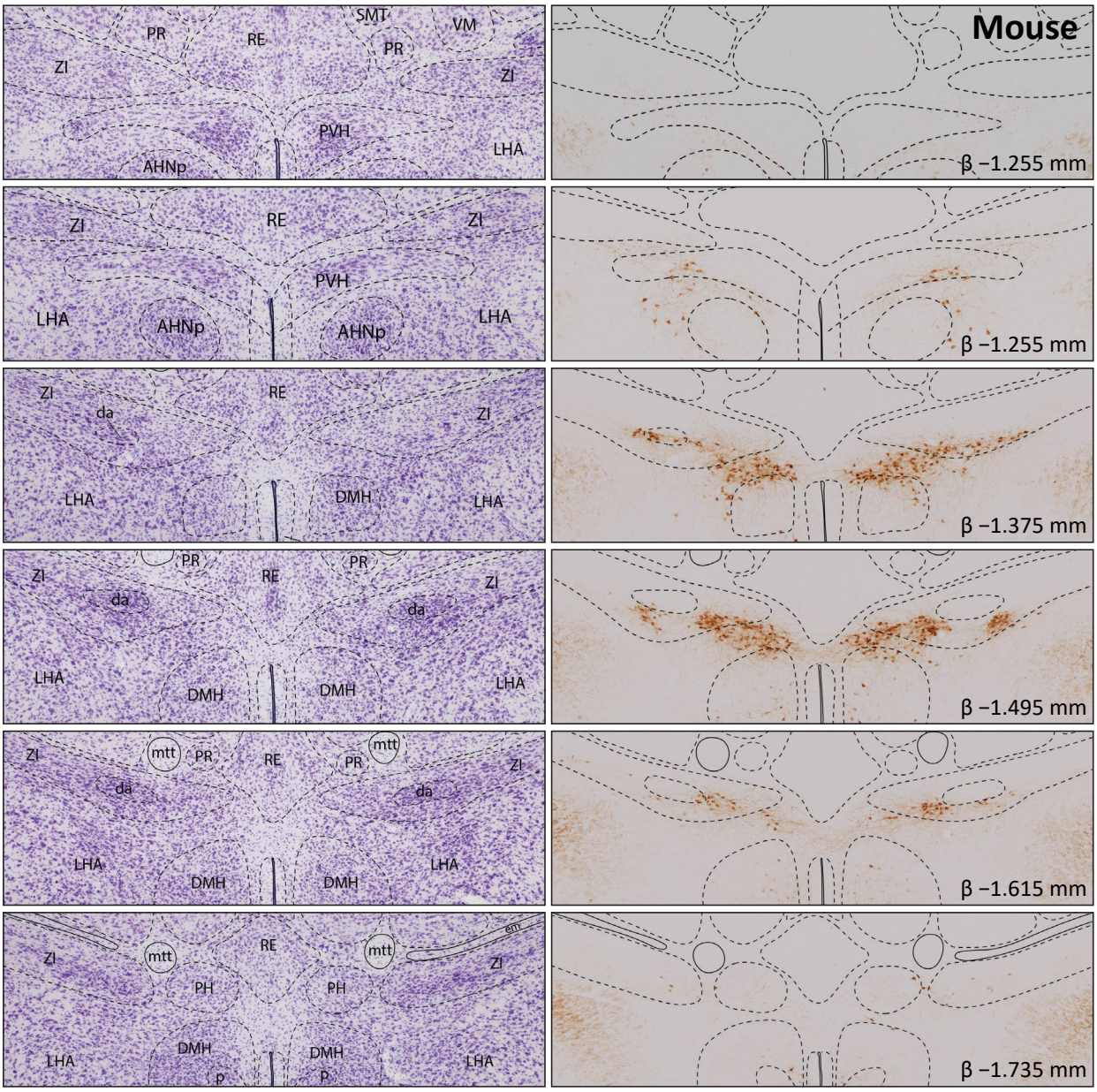

Figure 2. Induction-based distribution analysis of incerto-hypothalamic tyrosine hydroxylase neurons. (*left*) Nissl-stained sections of dorsal hypothalamic sections containing the zona incerta (ZI). (*right*) Tyrosine hydroxylase-expressing neurons labeled using an immunoperoxidase reaction. Overlaid boundaries were transposed after alignment with adjacent Nissl-stained sections (left). These experiments reveal that the A13 dopaminergic population does not neatly fall within Nissl-defined ZI boundaries. Numbers in the lower-right corners show approximate bregma positions based on the Allen Reference Atlas. Abbreviations: AHNp, anterior hypothalamic nucleus posterior part; DMHa, dorsomedial hypothalamic nucleus anterior part; DMHp, dorsomedial hypothalamic nucleus posterior part; LHA, lateral hypothalamic area; mtt, mammillothalamic tract; PH, posterior hypothalamic nucleus; PR, perireuniens nucleus; RE, nucleus reuniens; ZIda, zona incerta dopaminergic group

Conventional pathway tracing techniques vs viral tracing

Viral strategies for pathway tracing are growing in popularity for many reasons. To date, the Khan lab has mainly used conventional tracers (PHAL, CTB, BDA, Fluoro-Gold) for its projects (**Figure 3**). I should therefore clarify some key methodological differences as they pertain to my research goals, and discuss reasons to choose one over the other.

Viral vectors are highly customizable both at the level of gene cargo and capsid properties. They allow signal amplification and promoters can be used to restrict expression to neurons, avoiding leaving other cell types such as glial cells unaffected. Although PHAL can resolve morphology of distant axons with Golgi-like precision, the level of signal can fluctuate as a function of tracer concentration. This is not a problem viral tracing shares when reporter expression is amplified using the elongation factor 1 alpha or cytomegalovirus genes. Anterograde tracers are best interpreted when each traced neuron can be identified, this is challenging for PHAL because the compound is often concentrated in the parenchymal space of the injection site. With viruses, all observed signals result from endogenous expression of reporters so injection sites are highly interpretable.

Retrograde tracing is gradually embracing viral technologies as well. A recently created designer rAAV-retro was shown to retrogradely label more neurons than Fluoro-Gold (Tervo et al., 2016). An added advantage is the ability to characterize morphotypes of retrogradely-labeled neurons and fully characterize axon collaterals. A clear injection site is necessary to interpret retrograde tracing experiments. In the case of CTB, the extent of diffusion is clearly observed when immunolabeled, and viral tracing with rAAV-retro does not allow this. The glycoprotein-deleted rabies virus (RV-ΔG) method is an excellent alternative. For this strategy, “seed” neurons are marked by inducing expression of avian TVA receptors and G protein. Subsequent introduction of a pseudotyped rabies virus, composed of avian envelope protein and lacks a G protein, allows monosynaptic retrograde tracing of seed neurons (Wickersham et al., 2007; Callaway and Luo, 2015).

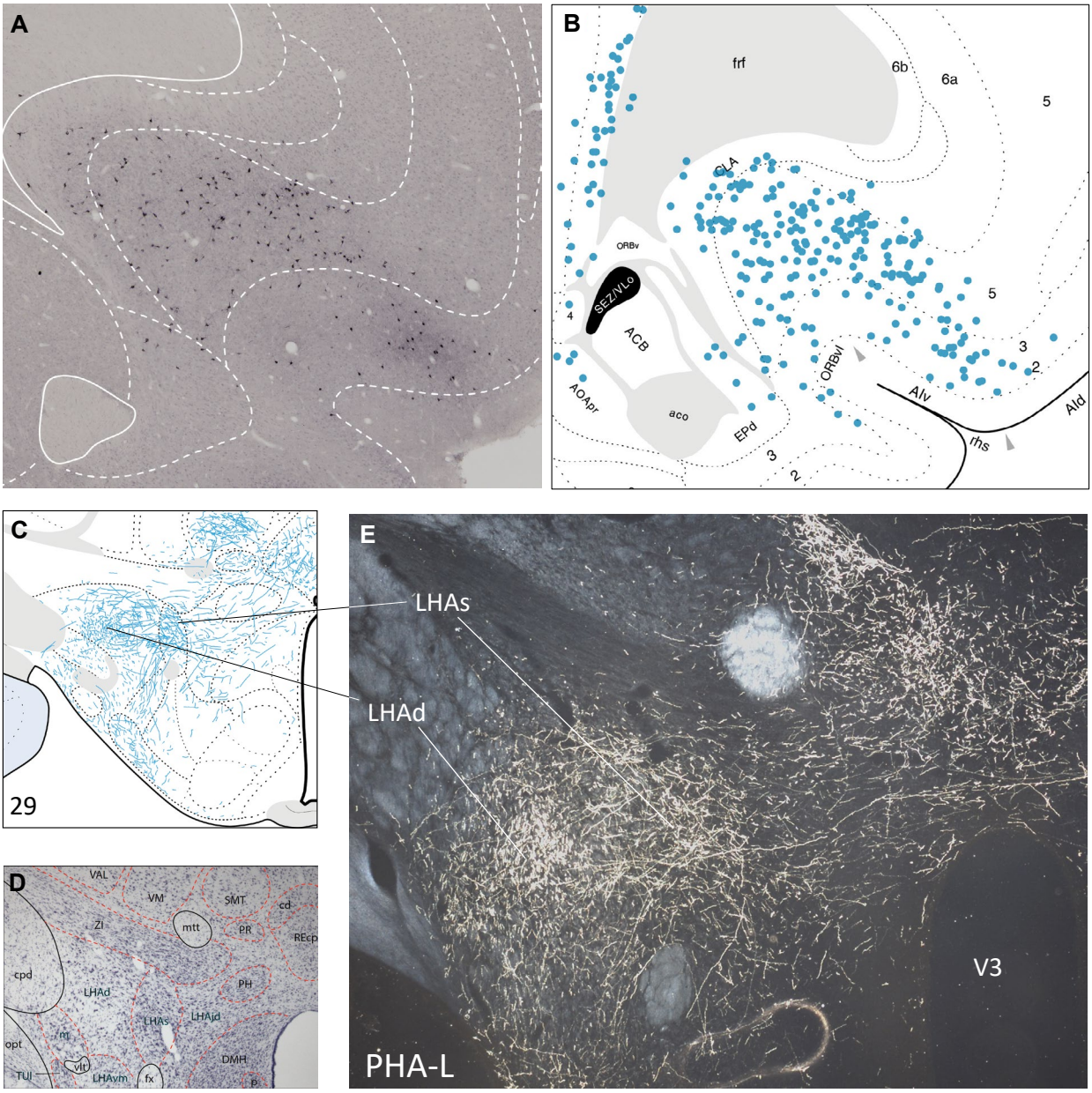

Figure 3. Examples of mapped cell bodies and axons. (**A**) Retrogradely labeled cells immunoreactive for CTB. White lines correspond to boundaries obtained using an adjacent Nissl-stained section. (**B**) Mapped representations of CTB-labeled neurons from (A). (**C**) Mapped representations of axons in hypothalamus from (E). (**D**) Nissl-stained section with boundaries drawn following definitions from Swanson (2018). (**E**) Darkfield photomicrographs showing anterogradely labeled axons in the lateral hypothalamic area (LHA). The supraformical (LHAs) and dorsal (LHAd) regions are indicated to relate histologically identified axons (E) to their mapped representations (C). See Table 1 from Chapter 1 for abbreviations.

In contrast to CTB, the RV-ΔG approach allows characterization of features within the injection site that are otherwise obscured by parenchymal tracer deposits.

It is important to recognize that although viral technologies have unlimited potential in their research applications, their development tends to outpace our ability to understand them. This is especially evident for those created using directed-evolution strategies, which are likely to display tissue tropisms that reflect the environment in which they evolved (Brown et al., 2021). For instance, the rAAV-retro that was engineered to trace substantia nigra and cerebellum (Tervo et al., 2016) are unlikely to have the same efficacy for applications in cortex or hypothalamus. Indeed, one study observed significant cell type and tissue-specific differences between rAAV-retro, RV-ΔG, and fluorescent retrobeads (Sun et al., 2019). Thus, it is important to establish whether viral tropism is suitable for tracing for each brain region, ideally by comparing efficacy with a gold-standard conventional tracer.

My goal was to simultaneously examine input and output connections of the mPFC. Perhaps this is very well suited for a RV-ΔG approach, but this technique would also require careful assessment of viral tropism for two viruses and tests to ensure specific mono-synaptic transduction through TVA-expressing neurons. Alternatively, viral cocktails could have been used, but given differential tropisms (Sun et al., 2019), it is unlikely that such an approach would represent input and output connections with equal fidelity. Therefore, combined injections of conventional tracers remains the cheaper and most effective option for the work shown in Chapter 1.

Introduction to Chapter 1

Research into cerebral hemisphere control of feeding primarily focused on the nucleus accumbens (ACB). Work pioneered by the late Ann Kelley demonstrated that pharmacological manipulation of this region produced voracious feeding that was comparable to direct activation of the lateral hypothalamic area (LHA) (Maldonado-Irizarry et al., 1995). This chapter was inspired by more recent work led by one of her students, who showed pharmacological stimulation of the medial prefrontal cortex (mPFC) also produced feeding (Mena et al., 2011). Both the ACB and LHA receive axonal projections from the mPFC, but a follow-up study proposed that only the LHA was necessary for mPFC-driven feeding (Mena et al., 2013).

My goal was to use tract-tracing to examine input and output connections of the mPFC. If one must posit a working hypothesis, it would be that mPFC connections with the hypothalamus are organized in a manner that can support mPFC control of feeding. This work, in my opinion, is best viewed as a discovery process. Detailed descriptions of connectivity tend to generate new areas to explore.

Chapter 1

Topographic organization of bidirectional connections between the medial prefrontal cortex and the diencephalon of the adult male rat

Kenichiro Negishi[1], Laura P. Montes[1], Lidice Soto[1], Cindy N. Oliveros[1], and Arshad M. Khan[1,2]

[1]Department of Biological Sciences, The University of Texas at El Paso, El Paso, Texas 79968

[2]Border Biomedical Research Center, The University of Texas at El Paso, El Paso, Texas 79968

Acknowledgments: This work was supported by NIH grants GM109817 and GM127251 (both to AMK), a Grand Challenges Grant from the UTEP Office of Research and Sponsored Projects (to AMK), and through a UTEP PERSIST (Program to Educate and Retain Students in STEM Tracks) training program funded by Howard Hughes Medical Institute (HHMI) grant 52008125 (PI: S. B. Aley, Co-PIs: L. Echegoyen, A. M. Khan, D. Villagrán, E. Greenbaum). KN is an Eloise E. and Patrick Wieland Graduate Fellow and was supported for this work by NIH grant GM109817 (to AMK). This work was also supported by the Border Biomedical Research Center, which is funded by the National Institute on Minority Health and Health Disparities (NIMHD; 2U54MD007592; PI: R. A. Kirken).

Abstract

The medial prefrontal cortex (mPFC) is a connectionally and functionally diverse structure. It uses far-reaching connections in every part of the central nervous system to promote adaptive changes to ongoing behaviors. mPFC is often described across functional and anatomical gradients, a dorsal-ventral gradient being the most prominent. Topographic organization is a general feature of the nervous system, and it is becoming clear that such spatial arrangements can reflect connectional, functional, and cellular differences. mPFC is known to form reciprocal connections with cortical areas and thalamus; however, these connectional features have not been described in detail. Here, we used co-injected anterograde (*Phaseolus vulgaris* leucoagglutinin) and retrograde (cholera toxin B subunit) tracers throughout the mPFC to identify zones of reciprocal connectivity in the diencephalon. Tracer distributions were observed using a Nissl-based atlas-mapping approach that facilitates description of topographic organization. This report describes connections of the infralimbic area (ILA) and dorsal part of the anterior cingulate area (ACAd) throughout the diencephalon. We found that corticothalamic connections are predominantly reciprocal, and that ILA and ACAd connections tended to be spatially segregated with minimal overlap. In hypothalamus, we found dense and specific ILA terminals in Swanson's dorsal (LHAd) and suprafornical (LHAs) divisions of the lateral hypothalamic area along with the parastriatal nucleus (PSTN), terete part of the tuberal nucleus (TUte), and an ill-defined dorsal cap of the medial mammillary nucleus (MM). We discuss these findings in the context of feeding behaviors.

Introduction

The medial prefrontal cortex (mPFC; alternatively, the 'cingulate region' [Swanson, 2015]) is critical for making adaptive changes to ongoing behaviors (Miller and Cohen, 2001). These functions leverage excitatory outputs to every major division of the central nervous system (Gabbott et al., 2005). Interestingly, the mPFC is the last brain region to fully mature (Paus et al., 1999), leaving wide opportunity for the environment and chance to shape the dynamics of behavior. It is therefore appropriate that considerable attention was committed towards understanding the mPFC and how it contributes to mental illness, substance use disorders, and other aberrations of motivated behaviors (Sapolsky, 2004).

Classical experiments with decerebrate animals have made it clear that diencephalon (alternatively, the 'interbrain' [Swanson, 2015]) is necessary for the expression of motivated behaviors as no spontaneous or intact behaviors were observed in these preparations (Grill and Norgren, 1978). Decorticate animals, on the other hand, were able to perform motivated behaviors but failed to integrate environmental information as indicated by their expression at inappropriate times, places, and a near-complete lack of anticipatory and social behaviors (Vanderwolf et al., 1978). At a structural level, motivated behaviors are supported by distributed and interconnected brain regions that are often described in a highly schematized manner (Watts et al., 2022).

Pursuing a comprehensive "wiring diagram" for motivated behaviors is technically challenging due to the well-recognized but poorly addressed phenomenon of topographic organization. That is, connections within discrete gray matter regions often form gradients or compartmental organization (Hintiryan et al., 2016) that require careful parsing across three dimensions. Moreover, topography is increasingly observed to align connectional, functional, cellular and gene-expression differences within individual brain regions (Mandelbaum et al., 2019; Mickelsen et al., 2020). Documentation of connectional topography alone will likely identify meaningful spatial patterns when merged with relevant functional and transcriptomic datasets.

We accordingly examined mPFC connections using a Nissl-based atlas-mapping approach that is profitably employed to uncover sub-regional architecture (Simmons and Swanson, 2009a). Bidirectional connections were revealed by co-injecting the anterograde and retrograde tracers *Phaseolus vulgaris* leucoagglutinin (PHAL) and cholera toxin B subunit (CTB) throughout the perigenual mPFC.

mPFC is commonly studied along a dorsoventral functional and anatomical gradient. The infralimbic area (ILA) and dorsal part of the anterior cingulate region (ACAd) are on opposite ends of this gradient, making them excellent starting points for elaborating mPFC connections. Here, we present the complete mappings of their bidirectional connections in the diencephalon with the goal of clarifying their precise spatial arrangements. This work, to our knowledge, is the first detailed representation of reciprocal connectivity between these mPFC structures and the diencephalon. Our mapping of ILA and ACAd connections in the present study, portions of which have been presented in preliminary form (Negishi et al., 2015; Negishi and Khan, 2017, 2019), prompts interpretive refinements to various thalamic and hypothalamic regions, especially regarding mPFC connections with the lateral hypothalamic zone and zona incerta (ZI).

Materials and Methods

Animals

Experiments were performed on adult male Sprague-Dawley rats (Harlan Labs, Indianapolis, IN) weighing 300–400 g. Animals were fed ad libitum and housed in a temperature-controlled vivarium under a 12-hour day/night cycle (lights on at 0700 h). All methods followed protocols approved by the The University of Texas at El Paso Institutional Animal Care and Use Committee and are in accordance with the NIH Guidelines for the Care and Use of Laboratory Animals (NRC, 2011).

Intracranial tracer injection

Rats were anesthetized with a mixture containing 50% ketamine, 5% xylazine, 10% acepromazine and 35% sterile saline at a dosage of 1 µL/g. Once anesthetized, animals were positioned in a Kopf stereotaxic frame and maintained on 1.5% isoflurane delivered with pure oxygen for the duration of the surgery. The frontal bone and Bregma fiducials were carefully exposed for craniotomy. Glass micropipettes with inner tip diameters ranging from 12 to 20 µm were selected and filled with a cocktail containing 2.5% PHAL (Vector Laboratories, catalog #L-1110) and 0.25% CTB (List Biological Laboratories, catalog #104) dissolved in 10 mM sodium phosphate solution. Stereotaxic coordinates targeting the ILA (AP +11.20 mm, ML –0.50 mm and DV –4.40 mm) and ACAd (AP +11.20 mm, ML –0.50 mm and DV –2.40 mm) were obtained using the Paxinos and Watson (2014) rat brain atlas. Tracers were ejected iontophoretically at a current of 5 µA through 7 sec on/off cycles for 10–15 min. Micropipettes were retracted slowly after a resting period of 10 min. Following surgery, animals received intramuscular injections of Flunazine (Bimeda-MTC Animal Health, Inc., catalog #200-387) as an analgesic and Gentamicin (Vedco, Inc., catalog #50989-040-12) for its antimicrobial and anti-inflammatory properties. Another injection of Flunazine was given 8 h after surgery if grimaces or other signs of pain were detected. Daily status evaluations were maintained for a survival period of 10–14 d to allow for tracer transport.

Transcardial perfusion and tissue preparation

Animals were sedated with isoflurane for two min and perfused transcardially with 200 mL of phosphate-buffered saline (PBS; pH 7.4 at room temperature), followed by fixation with 350 mL of ice-cold 4% paraformaldehyde (PFA) in 0.05 M PBS (pH 7.4 at room temperature). Brains were carefully dissected and post-fixed overnight in the same PFA solution at 4°C. Brains were transferred to PBS containing 10% sucrose (w/v) until fully saturated. Fixed brains were then blocked (a coronal cut at the level of the caudal end of the mammillary body) and frozen on a sliding microtome (Reichert Austria Nr. 15 156) stage using dry ice. Blocks were cut into coronal sections of 30 µm thickness collected

into 6 series. Sections were collected into 24-well plates containing cryoprotectant (50% phosphate buffer, 20% glycerol, and 30% ethylene glycol) and stored at –20°C until further processing.

Tissue processing and immunohistochemical detection of tracers

Sections were removed from cryoprotectant and placed in 0.05 M Tris-buffered saline (TBS; pH 7.4 at room temperature) for five washes, each for five min (5 × 5). Endogenous peroxidase activity was suppressed by incubating sections in a TBS solution containing 0.014% phenylhydrazine for 20 min and then rinsed in TBS (5 × 5). Following 2 h incubation in blocking solution consisting of 2% (v/v) normal donkey serum (EMD Millipore; Catalog #S30-100ML) and 0.1% Triton X-100 (Sigma-Aldrich; Catalog #T8532-500ML), sections were transferred into primary antiserum for about 48 hours at 4°C. Primary antisera contained antibodies raised against PHAL (species: rabbit; dilution: 1:4,000; Vector Labs Cat # AS-2224); RRID: AB_2313686) or CTB (species: goat; dilution: 1:10,000; List Biological Cat # 703; RRID: AB_10013220). Sections were then washed (5 × 5) in TBS and incubated in secondary antibody solution with biotinylated antibodies raised against rabbit (species: donkey; dilution: 1:1,000; Jackson ImmunoResearch Labs Cat# 711-065-152; RRID: AB_2340593) or goat (species: donkey; dilution: 1:1,000; Jackson ImmunoResearch Labs Cat# 705-065-147; RRID: AB_2340397). After a 5 h incubation period at room temperature, washes in TBS (5 × 5), signal amplification was achieved using an avidin-biotin-horseradish peroxidase complex (Vectastain ABC HRP Kit, Vector, 45 µl reagent A and B per 10 ml) in 0.05 M TBS containing 0.1% Triton X-100 (v/v) for 1 h. Reacted tissues were then developed in 0.05% 3, 3'-diaminobenzidine (DAB) (Sigma-Aldrich) mixed with 0.015% H_2O_2 in 0.05 M TBS for 10–20 min. Sections were then washed in TBS (5 × 5), mounted onto gelatin-coated slides and left to dry overnight at room temperature. Finally, tissue sections were dehydrated with ascending concentrations of ethanol (50–100%), defatted in xylene, and coverslipped with DPX mounting medium (Catalog # 06522; Sigma-Aldrich).

The same overall steps from DAB were used for immunofluorescent labeling. The phenylhydrazine reaction was omitted and secondary antibodies with fluorescent conjugates were used (see **Table 2**). After washing off secondary antiserum, freely-floating sections were mounted onto glass slides and coverslipped in sodium phosphate-buffered glycerol (0.05 M in 50% glycerol).

Double-label immunohistochemistry was performed using the identical steps as described above for immunoperoxidase staining. Steps and reagents used for nickel-intensified DAB stain were identical to that described above except for the DAB solution. Nickel-intensification was achieved with 0.05% DAB mixed with 0.005% H_2O_2, 0.1% ammonium nickel(II) sulfate dissolved in 0.05 M TBS. The phenylhydrazine step was omitted for the second stain that ended with a brown DAB product.

Antibody validation

Antisera for this study only contained antisera raised against PHAL and CTB. Specific staining was not observed for PHAL or CTB in animals that did not receive tracer co-injections. Additionally, specific staining was not evident for injection cases that did not effectively transport tracers. The same validation approach and outcome were found in other reports that cataloged the same antibodies (Hahn and Swanson, 2010, 2012).

Nissl staining

Sections were first washed (5 × 5) in 0.05 M TBS (pH 7.4 at room temperature) to remove cryoprotectant. Free-floating sections were mounted onto gelatin-coated glass slides and dried overnight at 60°C. Sections were dehydrated through ascending concentrations of ethanol (50%, 70%, 95%, and 100%) and defatted in xylenes for 25 min. Next, they were rehydrated and stained with a 0.25% thionin solution (thionin acetate, Catalog #T7029; Sigma-Aldrich Corporation, St. Louis, MO) and differentiated in 0.4% anhydrous glacial acetic acid. Stained slides were dehydrated again and coverslipped with DPX mounting medium and left to dry overnight.

Photography and post-acquisition image processing

Immunostained and Nissl-stained sections were visualized and photographed under brightfield and darkfield microscopy using a BX63 microscope (Olympus Corporation, Shinjuku, Japan) equipped with a DP74 color CMOS camera (cooled, 20.8 MP pixel-shift, 60 fps). Image acquisition with ×10 objectives (N.A. 0.4) , stitching (15% image overlap), and .TIFF image exporting were done with cellSens Dimension software (Version 2.3; Olympus Corporation). Images were adjusted for brightness and contrast using Adobe Photoshop (Version 13.0.1; Adobe Systems, Inc., San Jose, CA) and exported to Adobe Illustrator (AI; Version CC 18.0.0; Adobe Systems, Inc., San Jose, CA) for parcellation. mPFC sections stained for immunofluorescence were visualized with epifluorescence illumination using a Zeiss M2 AxioImager microscope equipped with an X-Y-Z motorized stage (Carl Zeiss Corporation, Thornwood, NY) and a 100 W halogen light source. An EXi Blue monochrome camera (Teledyne QImaging, Inc., Surrey, British Columbia, Canada) operated by Volocity Software (Version 6.1.1; Quorum Technologies, Puslinch, Ontario, Canada; installed on an Apple Mac Pro computer) was used to generate wide field mosaic images from multiple channels. The same equipment was used to generate bright field stitched images of adjacent Nissl-stained mPFC sections. Images were adjusted for brightness and contrast using Adobe Photoshop (Version 13.0.1; Adobe Systems, Inc., San Jose, CA) and exported to Adobe Illustrator (AI; Version CC 18.0.0; Adobe Systems, Inc., San Jose, CA) for parcellation.

Mapping of immunohistochemically detected tracer

The atlas-based mapping approach used here follows the cytoarchitectonic approach described by Swanson (1992, 1998, 2004, 2018). Briefly, formal cytoarchitecture-based definitions and nomenclature for gray matter regions were obtained for all areas examined (see Table C in Supplementary Information Folder 1 from Swanson [2018]), boundaries were drawn with Nissl-stained reference sections and then superimposed on DAB-stained sections to localize tracers. One of two approaches were used for this process. The first

involved making camera lucida pencil-on-paper drawings of cytoarchitectonic boundaries via drawing tube, aligning drawn boundaries to corresponding immunostained sections, and then transcribing histological data to digital atlas plates. The second approach involved placing images of Nissl- and immuno-stained tissues onto AI files as separate layers. Immunostained images were aligned to Nissl and boundary layers by relying on shared features (i.e., brain surfaces, white matter tracts, background staining, and blood vessels). These overlays informed the final transcription of data onto atlas plates on a different AI file. It should be emphasized that the transcription process, in our case, was a representation and never an attempt to simply fit or copy-paste information. Matching histological sections to atlas levels involved careful scrutiny of the histological plane-of-section and other forms of non-linear distortion (Simmons and Swanson, 2009a). Once the corresponding atlas levels were identified, maps were created using data from only the best-matched sections. Once histological sections were matched to atlas levels, axons were drawn using the pencil tool with high accuracy settings and cell bodies were plotted as ellipse objects. The goal was to accurately show spatial information with an attempt to also capture some morphological features such as connectional density, direction, and axonal morphology.

Semi-quantitative analysis

Mapped CTB datasets were used as a starting point to obtain a 0–5 scaling system for connectional strength. CTB-ir neuron counts across each diencephalic region at each atlas level was tabulated onto .CSV files. First, data were transformed using the natural logarithm and histograms were generated to confirm linearity. The highest log value was used to divide the dataset into quintiles, and the log values for each division was used to calculate thresholds for CTB connectional scores. Numerical thresholds for each score were calculated separately for each experiment (see **Supplemental Figure 1**)

To score PHAL axonal density, photos were examined in bins of 128 × 128 pixels (roughly 120μm ×120μm). **Supplemental Figure 1** shows representative snapshots

for each 0–5 score category. Scores were determined by obtaining bins from each diencephalic region and comparing them to the representative snapshots.

Results

Neuroanatomical connections of the mPFC

Immunodetected injection sites for PHAL and CTB injections into mPFC were localized with the aid of an adjacent Nissl-stained reference section and injection site maps show the extent of coverage in our study (**Figure 1**). Cytoarchitectonic parceling of the mPFC followed descriptions found in Brain Maps 4.0 (Krettek and Price, 1977; Vogt and Peters, 1981). Although delivered from the same micropipettes, co-injected PHAL and CTB were treated as individual experiments because they differ in their diffusion properties and uptake mechanisms (Gerfen and Sawchenko, 1984; Luppi et al., 1990). We found that co-injected tracers largely overlapped in their distributions but marginal differences, typically a wider spread for CTB, were observed. From a total of 39 co-injection experiments, five were selected to investigate mPFC connectional distributions within the diencephalon (**Figure 1**). These include two injections centered in the ACAd and three injections centered in the ILA. One of our mapped experiments, #15-113, is located in a ventral part of the ILA in levels 9 and 10 from Swanson (2018) (**Figure 2**). This roughly corresponds with the so-called “dorsal peduncular cortex” (Paxinos and Watson, 2014; Akhter et al., 2014), which has a slightly cell-sparse layer 2/3. PHAL-filled cell bodies were most abundant in layer 5 and adjacent layers. CTB spread was also concentrated in layer 5 but showed less immunoreactivity in layer 6. The ACAd injection (experiment #15-131) was restricted to level 9 of Swanson (2018), PHAL-immunoreactive (-ir) cells were concentrated in the boundary of layers 3 and 5, with a separate cluster in layer 6. CTB had a circular spread contained mainly in layers 3 and 5.

Our analysis of mPFC connectivity focused on the entire diencephalon. Connectivity maps showing tracer distributions were drawn from level 16 to level 34 (approx. 4.5 mm,

ranging between +0.10 mm and −4.45 mm from Bregma) are shown in **Figure 3**. Our data were also summarized using semi-quantitative scores (**Table 3**) to facilitate the assembly of connectomes.

For simplicity, our account of efferent and afferent ILA and ACAd connections will proceed across major divisions of thalamus and hypothalamus. And, given that mPFC connections have been characterized by many others (see Discussion), we will privilege the novel findings that result from our atlas-resolution mapping and bidirectional connectivity.

Description of fiber systems used by the ILA and ACAd to enter the diencephalon (PHAL anterograde tracing)

ILA axons innervating the diencephalon arrive through two routes. The primary route involves axons forming a lateral segment of the medial forebrain bundle (mfb) (**Figure 3**). This fiber system appears to be the origin of all ILA axons that are found in the hypothalamus (Negishi and Khan, 2019). In more caudal parts of hypothalamus, a substantial group of mfb collaterals ascend dorsomedially to target caudal parts of thalamus and the midbrain periaqueductal gray (PAG) (**Fig. 3n**–**s**). ILA axons in the mfb continued as far as the cerebral peduncles. The second route involves corticofugal axons that form fascicles in a ventromedial part of the caudoputamen (CP). This group, in our samples, appeared to enter the stria terminalis (alternatively, the 'terminal stria' [Swanson, 2015]) to innervate the bed nuclei of the stria terminalis (BST) (**Fig. 3n**–**s**). It is not clear if this route contributes ILA axons to rostral thalamus. Instead, ILA axons were often noted exiting the mfb in the direction of thalamus.

ACAd axons were not found in the mfb, instead they exclusively used the lateral forebrain system (lfb). Substantial groupings of passing fibers were observed in the internal capsule until they exited as thalamic radiations through the reticular nucleus (RT) at about −1.33 mm from Bregma (**Fig. 3h**–**k**). A subset of ACAd axons continued through the internal capsule until exiting through the ZI to arrive at ventral thalamus (**Fig. 3m**).

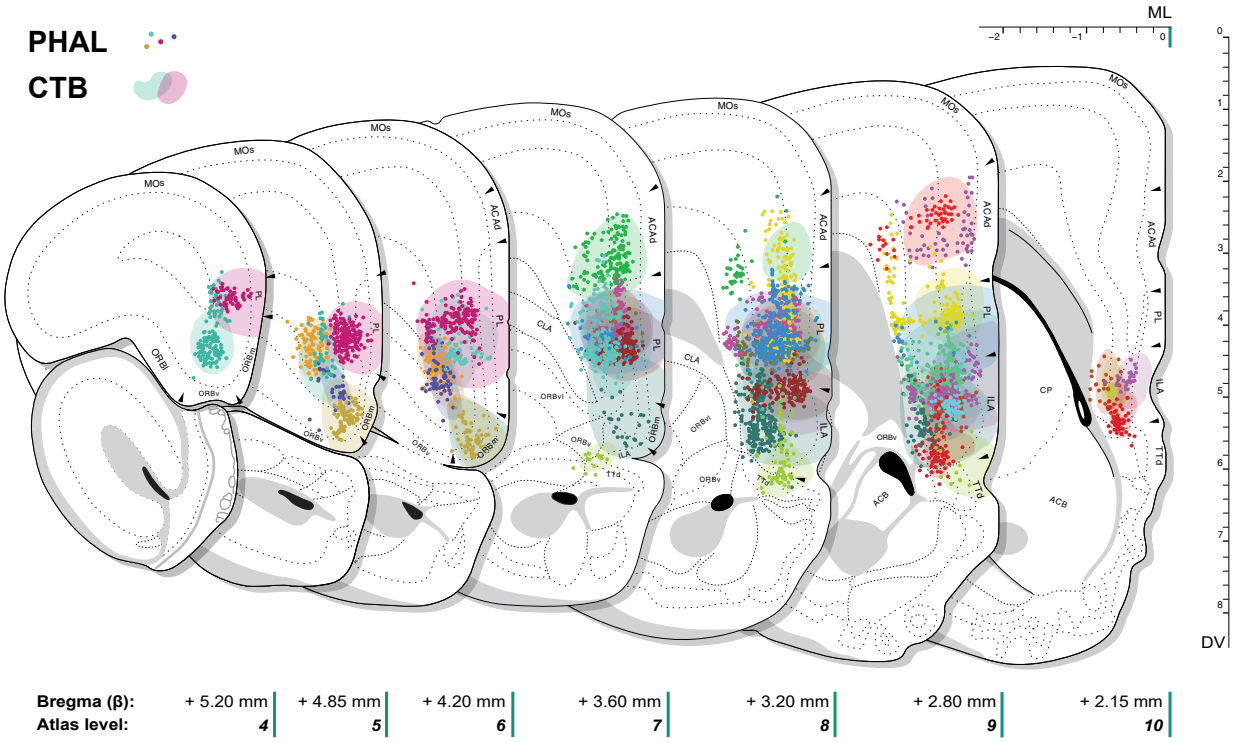

Figure 1. Maps showing PHAL and CTB injection sites in the medial prefrontal cortex (mPFC). Each experiment is coded with a unique color, with PHAL-ir cells shown as circles and CTB injection spread represented with contours. The scales on the edges indicate mediolateral (*top*), dorsoventral (*right*), and anteroposterior (*bottom*) dimensions based on atlas levels from *Brain Maps 4.0* (*BM4.0;* Swanson, 2018). See **Table 1** for abbreviations.

More caudally, ACAd axons exited the internal capsule entirely to innervate the caudal hypothalamus and PAG (**Fig. 3r, s**).

Projections from ILA and ACAd to hypothalamus (PHAL anterograde tracing)

We observed that although ILA axons were present throughout the hypothalamus, they were concentrated in a few regions. In more rostral sections, ILA axons in the anterior region of LHA (LHAa) took the form of passing fibers in the mfb (**Fig. 3i**–**k**). Once LHAa transitioned to the dorsal region (LHAd), massive collaterals were observed in the amygdala-bound ansa peduncularis and towards the LHAd and suprafornical region (LHAs) (**Fig. 3l**–**n** and **Figure 4**). This collateral system continued until the appearance of the subthalamic nucleus (**Fig. 3n, o**). These collaterals occupied an anterior-posterior distance between approximately −2.00 mm to −2.85 mm from Bregma. It is important to

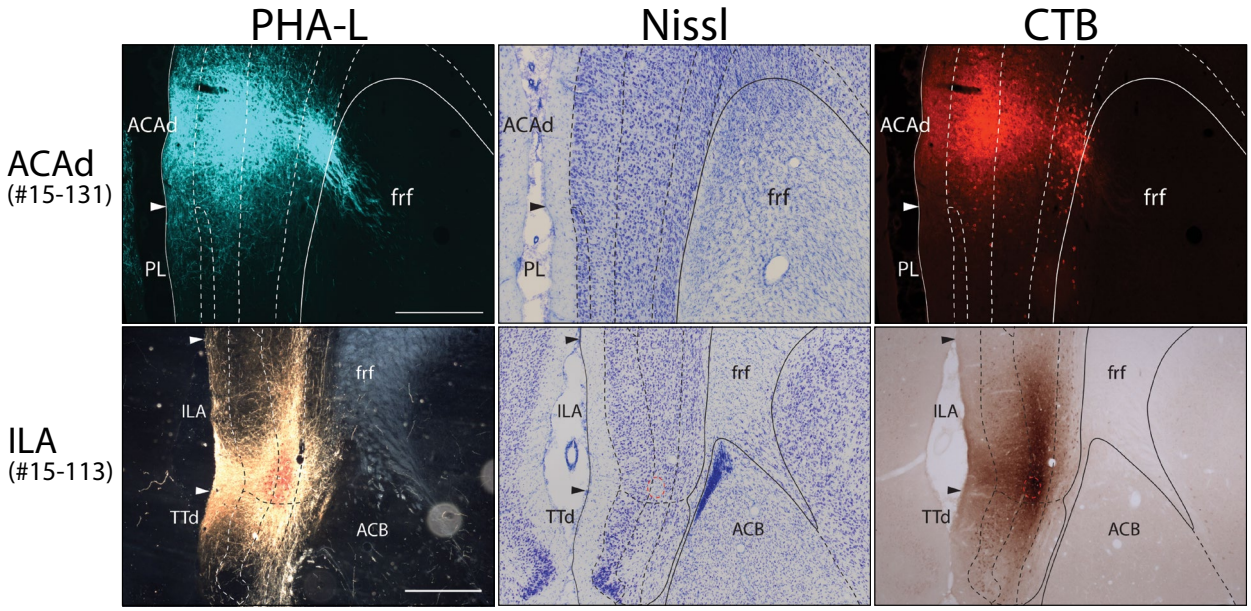

Figure 2. Photomicrographs showing the centers of PHAL and CTB injections into the ILA and ACAd**.** Regional boundaries derived from adjacent Nissl-stained sections (*middle*) were superimposed on immunostained images of PHAL (*left*) and CTB (*right*). Immunostained images shown here for ACAd and ILA were visualized with epifluorescence and DAB reactions, respectively. Scale bars: 500 μm. See **Table 1** for abbreviations.

note that LHAa and LHAd, as Nissl-defined regions, are distinguished on the basis of cell density (Swanson, 2018). Here, we observed that the cell-sparse LHAd is coincident with a sizable increase in axon collaterals. In more caudal sections, another major terminal was observed in the parasubthalamic nucleus (PSTN). ILA terminals to PSTN were remarkably restricted within its cytoarchitectonic boundaries (**Fig. 3q**–**r**). A subset of mfb collaterals formed dense terminals in the cytoarchitectonically distinct terete part of the tuberal nucleus (TUte) (**Fig. 5a, b**), this terminal field formed a compact tube shape at the base of the hypothalamus (**Fig. 3o**–**r**). By far the densest ILA projections were found in a horizontal band immediately ventral to the posterior hypothalamic nucleus (PH) and supramammillary nucleus (SUM) (**Fig. 3r, s**). There is no clear cytoarchitecture related to this ILA terminal field, but it is likely the dorsal cap of the MM that includes its median part (MMme) (**Fig. 5c, d**).

ACAd axons in hypothalamus were sparse. However, a notable increase in axon densities was apparent in the PH (**Fig. 3q**–**s**). ACAd axons were also present in the

subthalamic nucleus (STN) and PMd, regions that were avoided by ILA axons.

Hypothalamic afferents to the ILA and ACAd (CTB retrograde tracing)

CTB-labeled neurons in hypothalamus were far fewer than compared to thalamus. The LHAa contained and lateral preoptic area (LPO) contained, by far, the most retrogradely labeled neurons from ILA (**Fig. 3d**–**k**). Though few in numbers, ILA-projecting neurons were always present in hypothalamic volumes that contained dense axon terminals. These included the TUte, LHAd, LHAs, and PSTN (**Fig. 3l**–**r**).

Retrograde labeling from the ACAd was virtually undetected in the hypothalamus. The LPO contained the most CTB-ir from the ACAd whereas the adjacent LHAa contained scant labeling (**Fig. 3d**–**h**).

Bidirectional ILA and ACAd connections with thalamus (distributions of PHAL and CTB)

Two general observations can be made regarding mPFC connections with thalamus. Connectivity between mPFC and thalamus, with few exceptions, tended to form reciprocal connections. PHAL-ir axon terminals and CTB-ir neurons were tightly coupled in space, with the submedial (SMT), central medial (CM), and rhomboid (RH) thalamic nuclei being the only regions that showed unidirectional connections (**Fig. 3h**–**r**). ILA and ACAd connections were segregated in thalamus. Thalamic regions that connected with both ILA and ACAd, such as the mediodorsal nucleus (MD), tended to occupy non-overlapping compartments (**Fig. 3h**–**r**). The reuniens (RE) and paratenial (PT) were the only regions in which ILA and ACAd connections overlapped (**Fig. 3i**–**l**).

Most mPFC connections with thalamus, in both volume and density, were formed in the MD (**Fig. 3h**–**r**). The ILA and ACAd were respectively connected with the medial (MDm) and lateral (MDl) parts of MD, both cortical areas appeared to skirt around the central part. mPFC connections in the caudal half of MD appeared to withdraw towards its dorsal boundary (**Fig. 3n**–**q**). In the most caudal parts of MD, the ACAd connections were

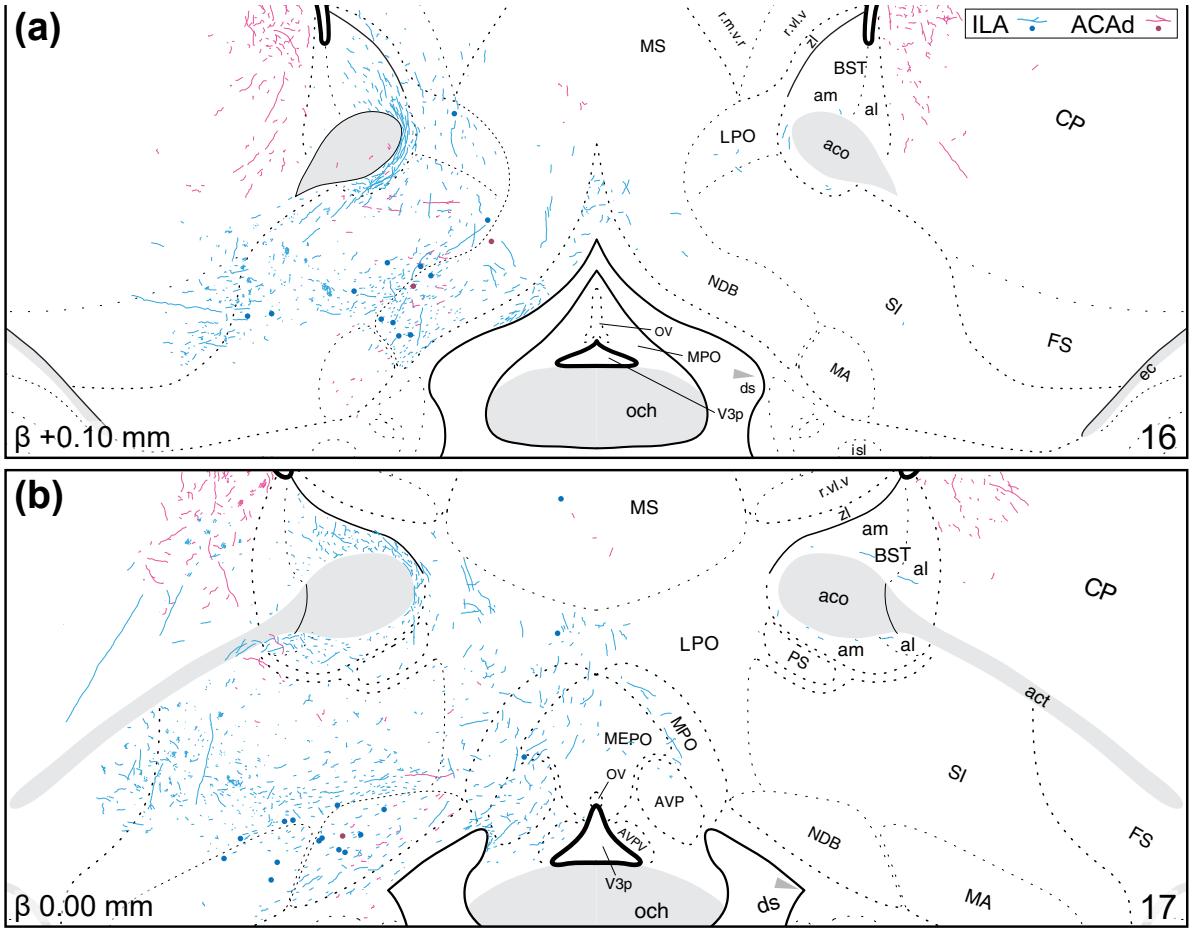

Figure 3. Representative maps showing distributions of immunoreactive PHAL and CTB throughout the diencephalon. Color-coded tracers from ACAd (purple; experiment #15-131) and ILA (blue; experiment #15-113) were localized using boundaries deduced from Nissl-stained sections. Inferred anterior-posterior positions, indicated as Bregma values in the lower-left corners, were derived from *BM4.0* (Swanson, 2018). Atlas levels from *BM4.0* are indicated in the lower-right corners. See **Table 1** for abbreviations.

densely aggregated in a space between the central lateral nucleus (CL) and MD, forming the ventrolateral perimeter of the lateral habenula (LH) (**Fig. 3p**–**r**).

Dense bidirectional ACAd connectivity was observed in the CM, initially appearing as a small circular cluster beneath the PT (**Fig. 3i**–**l** and **Figure 6**). High-magnification revealed numerous instances of putative axo-somatic contacts between PHAL-ir axons and CTB-ir neurons (**Fig. 6c**–**f**). ACAd connections with CM abruptly ended as the SMT emerged (AP approx. −2.45 mm from Bregma). The most caudal part of CM was bidirectionally connected with the ILA (**Fig. 3p**–**r**), PHAL-ir axons in this segment were passing dorsally towards the paraventricular nucleus (PVT).

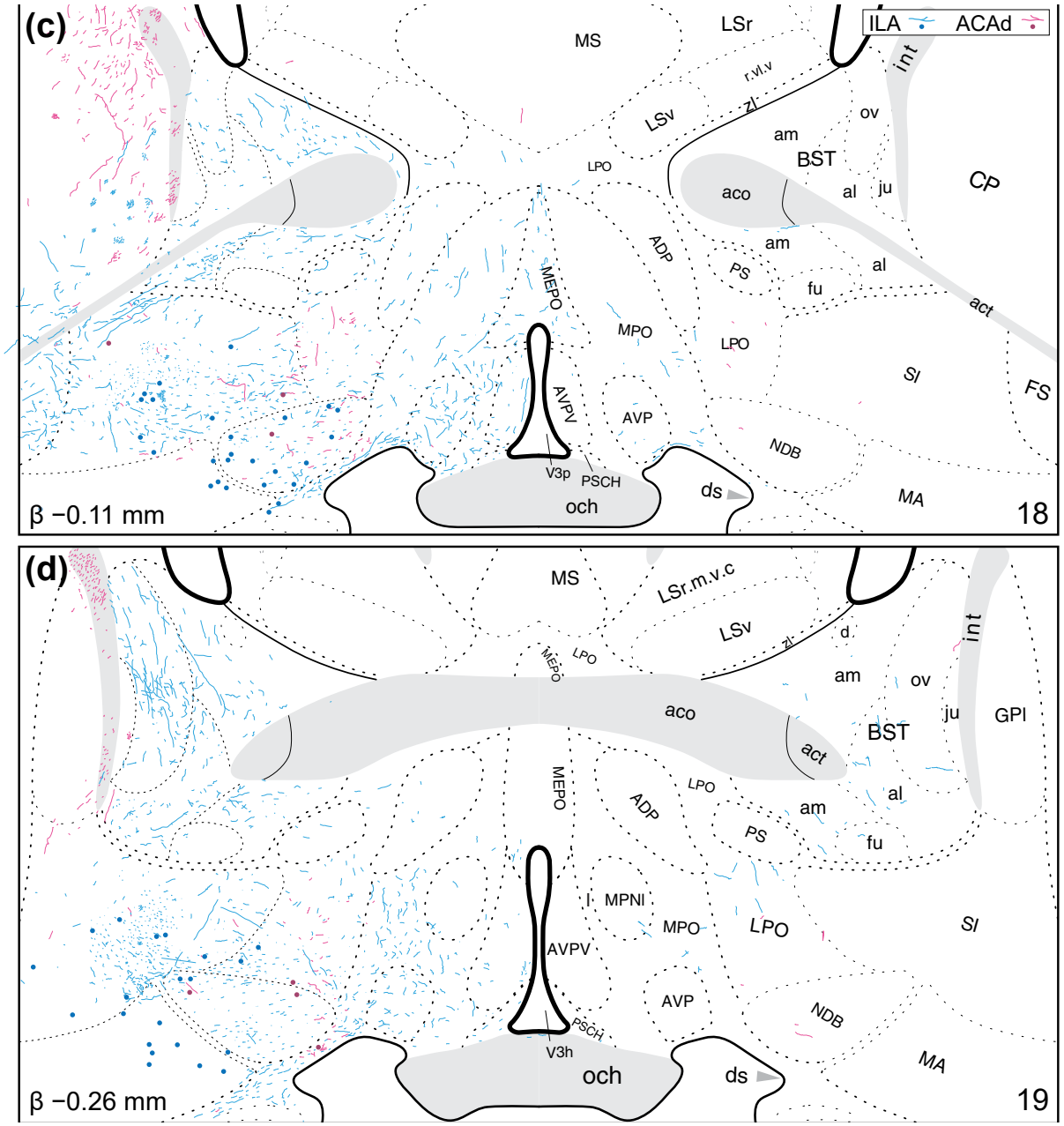

Figure 3 continued.

A ventral bidirectional cluster of ACAd connections was found in an ill-defined space immediately ventral to the mammillothalamic tract (**Fig. 3l, m**). This cluster was initially thought to be in the ZI, but examination with an adjacent Nissl-stained section revealed a cell-sparse zone separating this cluster from the ZI (**Fig. 7a, b**). Moreover, examination at higher magnification revealed several instances of putative axo-somatic contacts between PHAL-ir axons and CTB-ir neurons (**Fig. 7c**–**e**). It is unclear whether

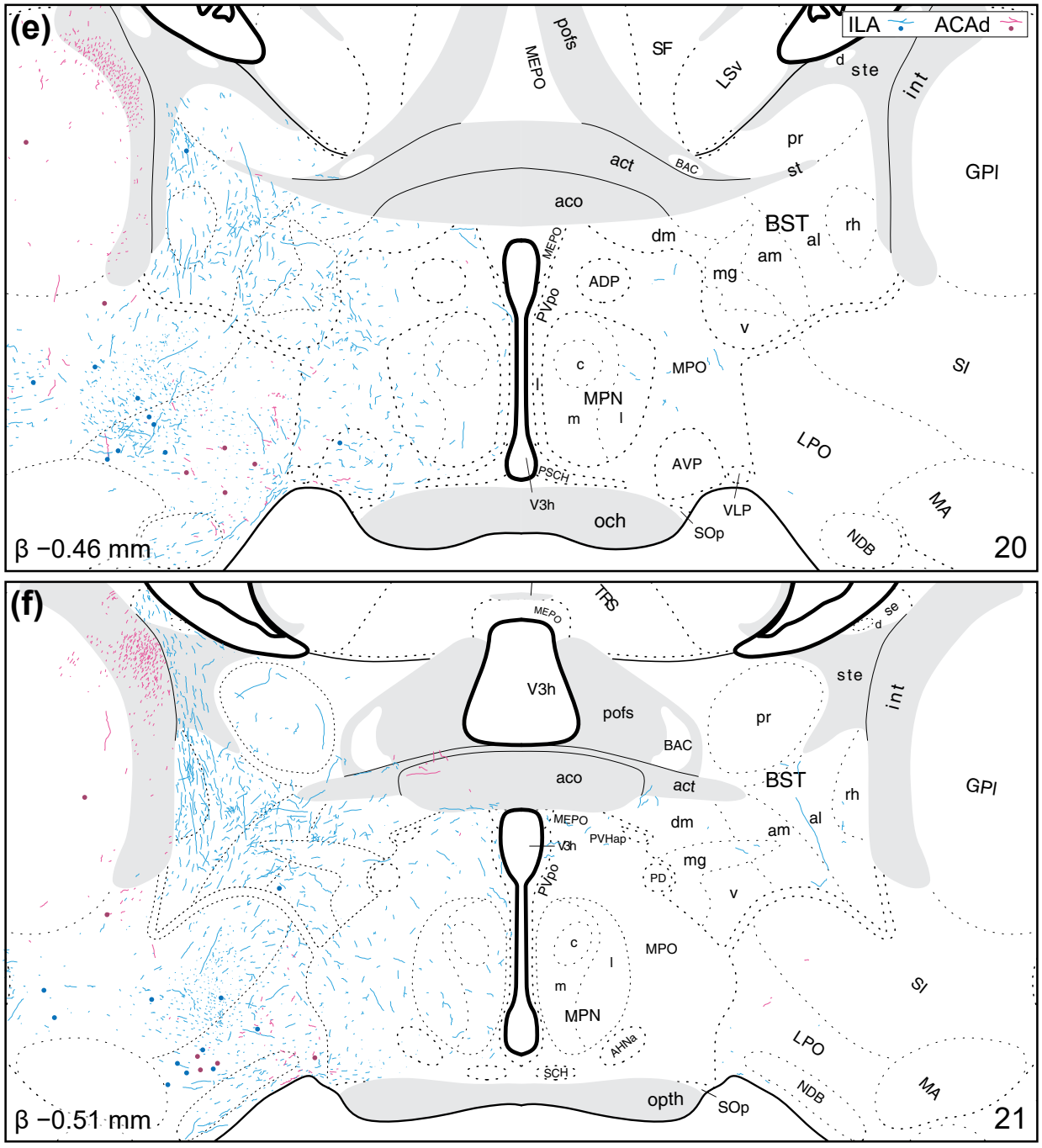

Figure 3 continued.

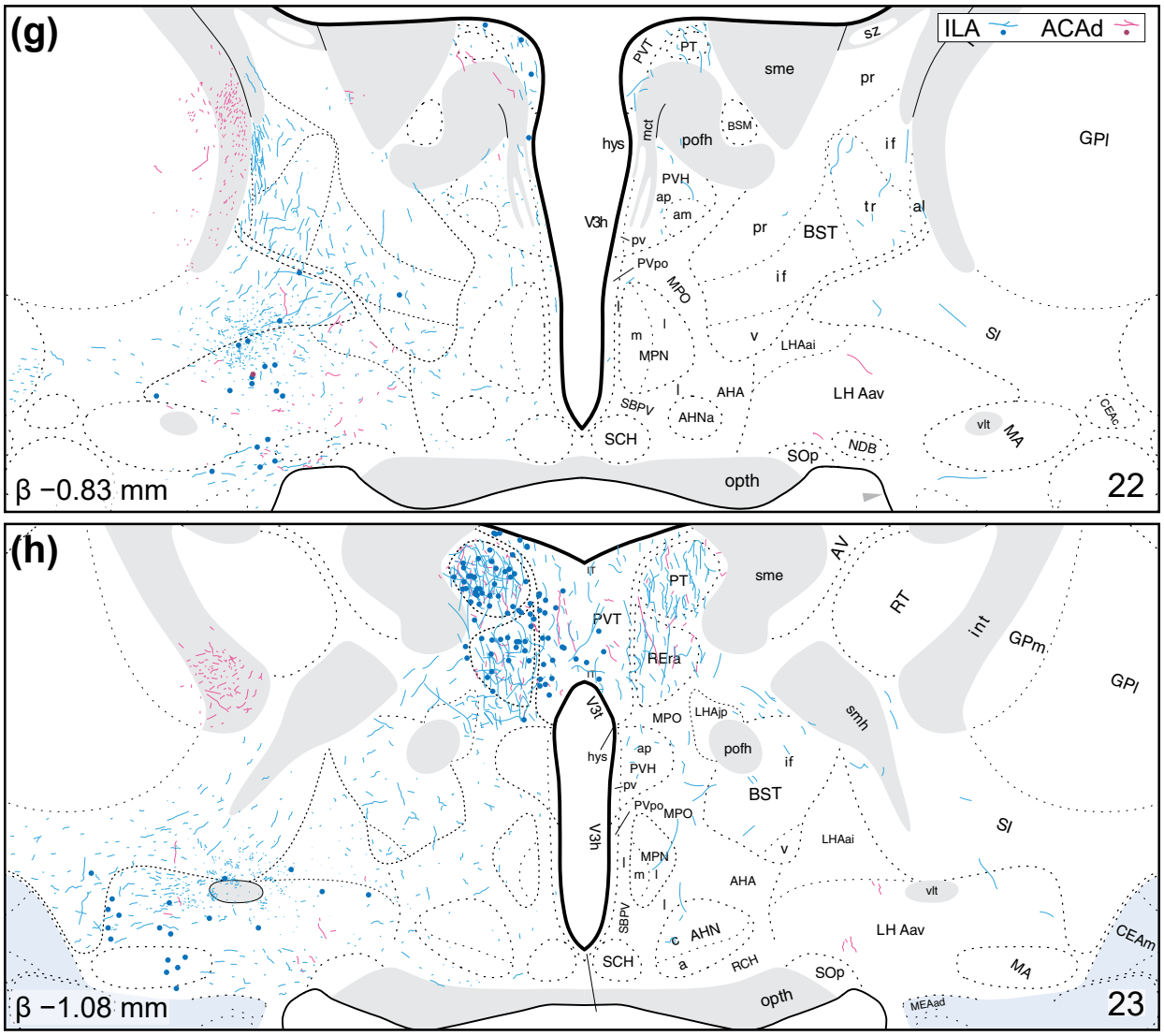

Figure 3 continued.

these ACAd connections are with the perireuniens (PR) or the ventral medial (VM) nucleus as it is centered between them. ACAd projections likely enter this cluster through the group of axons that pass through the RT and ventral part of anteromedial nucleus (AMv). ILA connections did not contribute to this sub-mammillothalamic cluster, but bidirectional connectivity was observed in the adjacent PR and RE.

Moderate retrograde labeling from the ILA was present in every level of PVT. These connections were bidirectional although ILA axons were slightly more concentrated in its caudal half (**Fig. 3Gg**–**r**). ILA and ACAd axons were present in the rostral half of PVT,

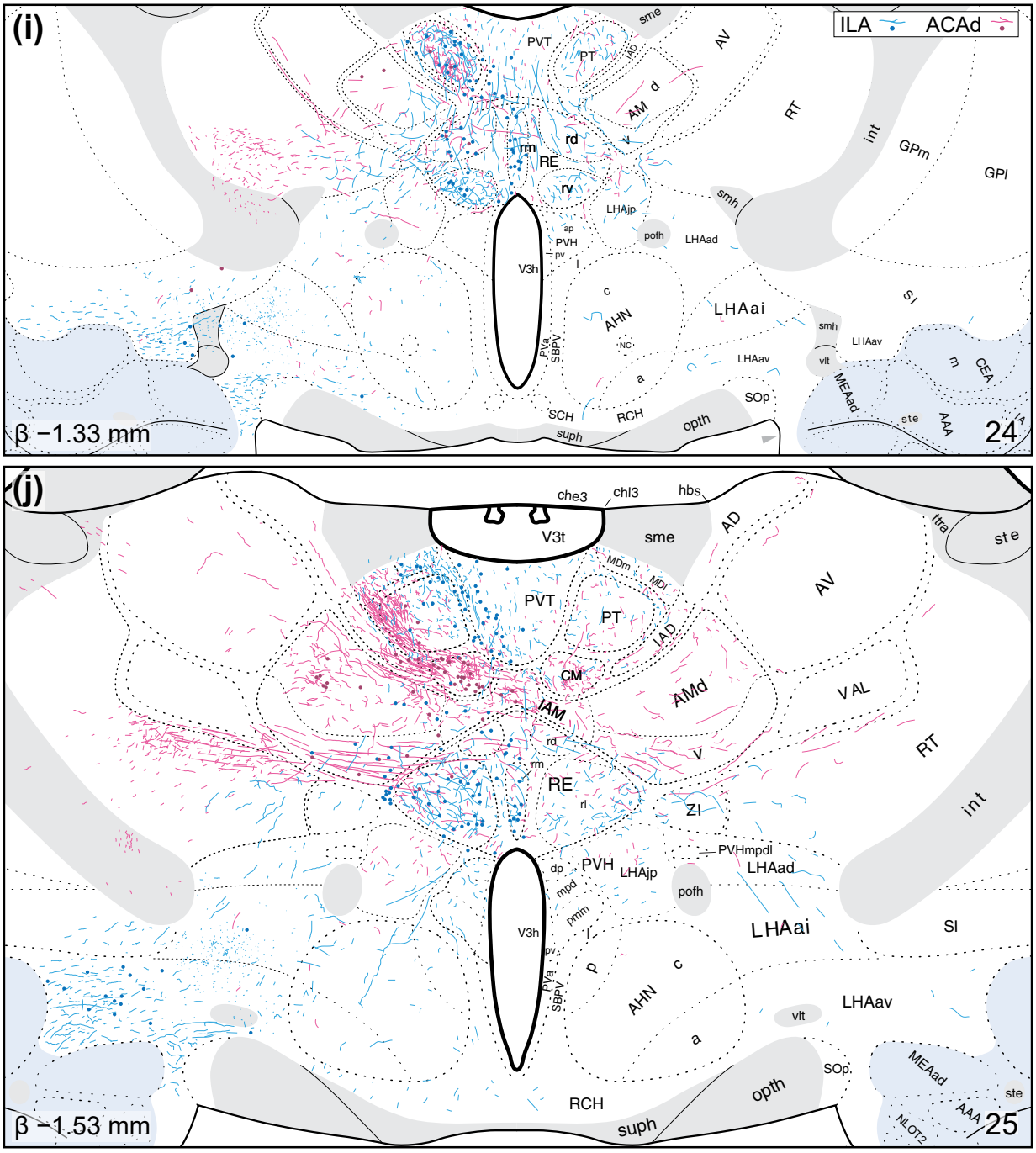

Figure 3 continued.

but they were sparse and had the morphology of axons-of-passage (**Fig. 3g**–**l**). Taken together, the PVT appears to be largely unidirectional with respect to ILA connectivity.

The AM and interanteromedial nucleus (IAM) were predominantly connected with the ACAd (**Fig. 3i**–**l**). Some ILA projections were detected in the AMv, but our samples

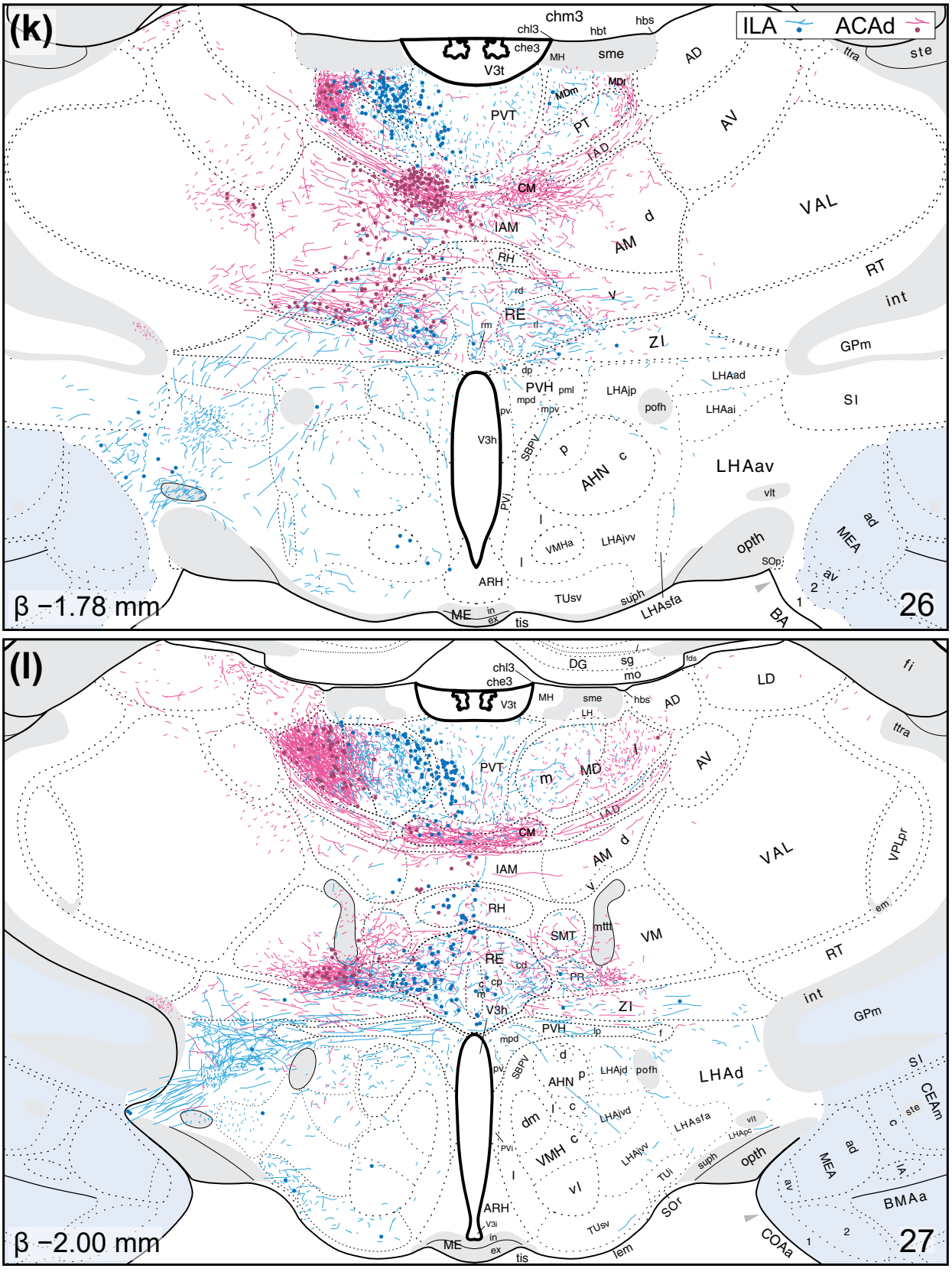

Figure 3 continued.

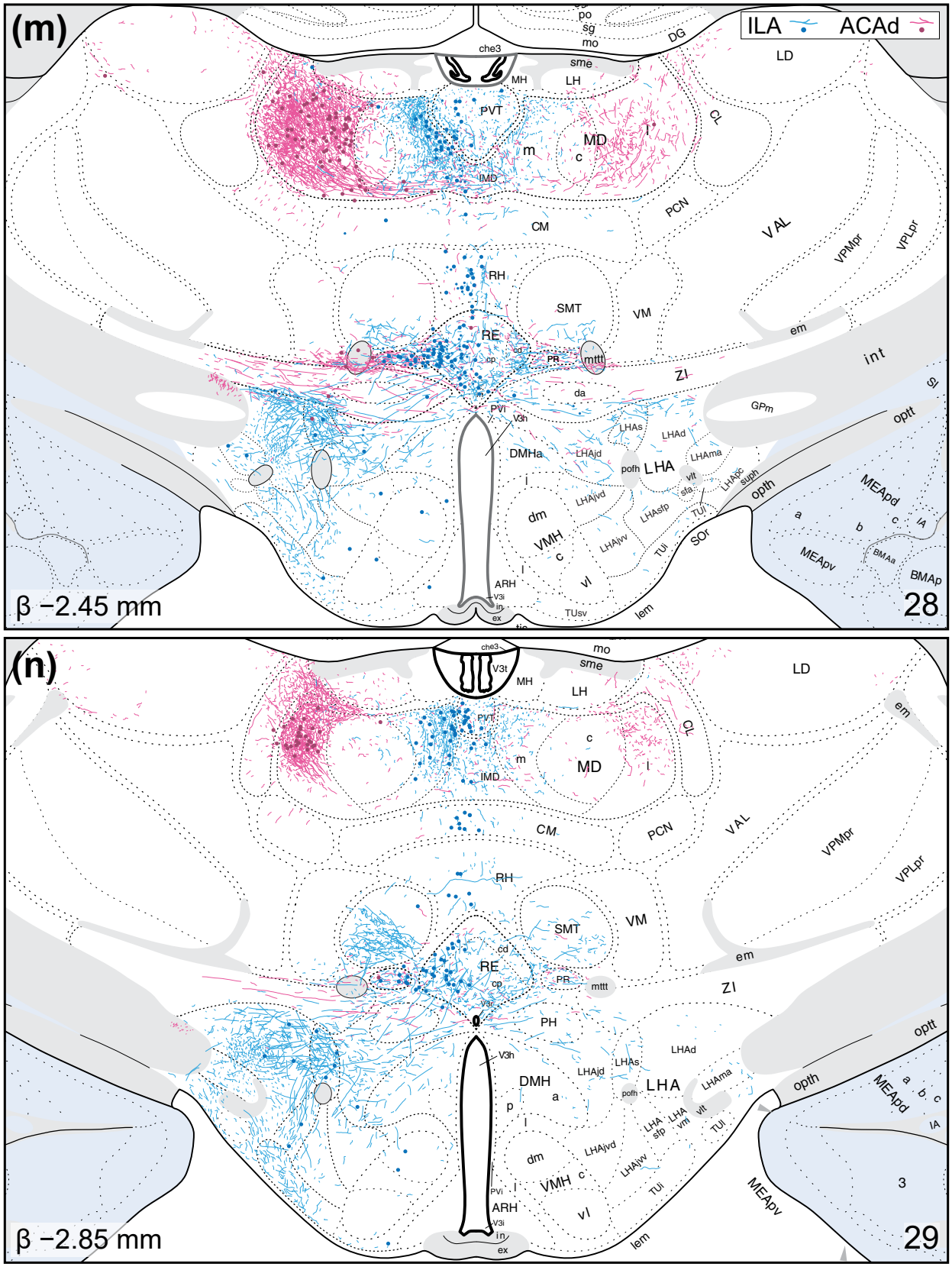

Figure 3 continued.

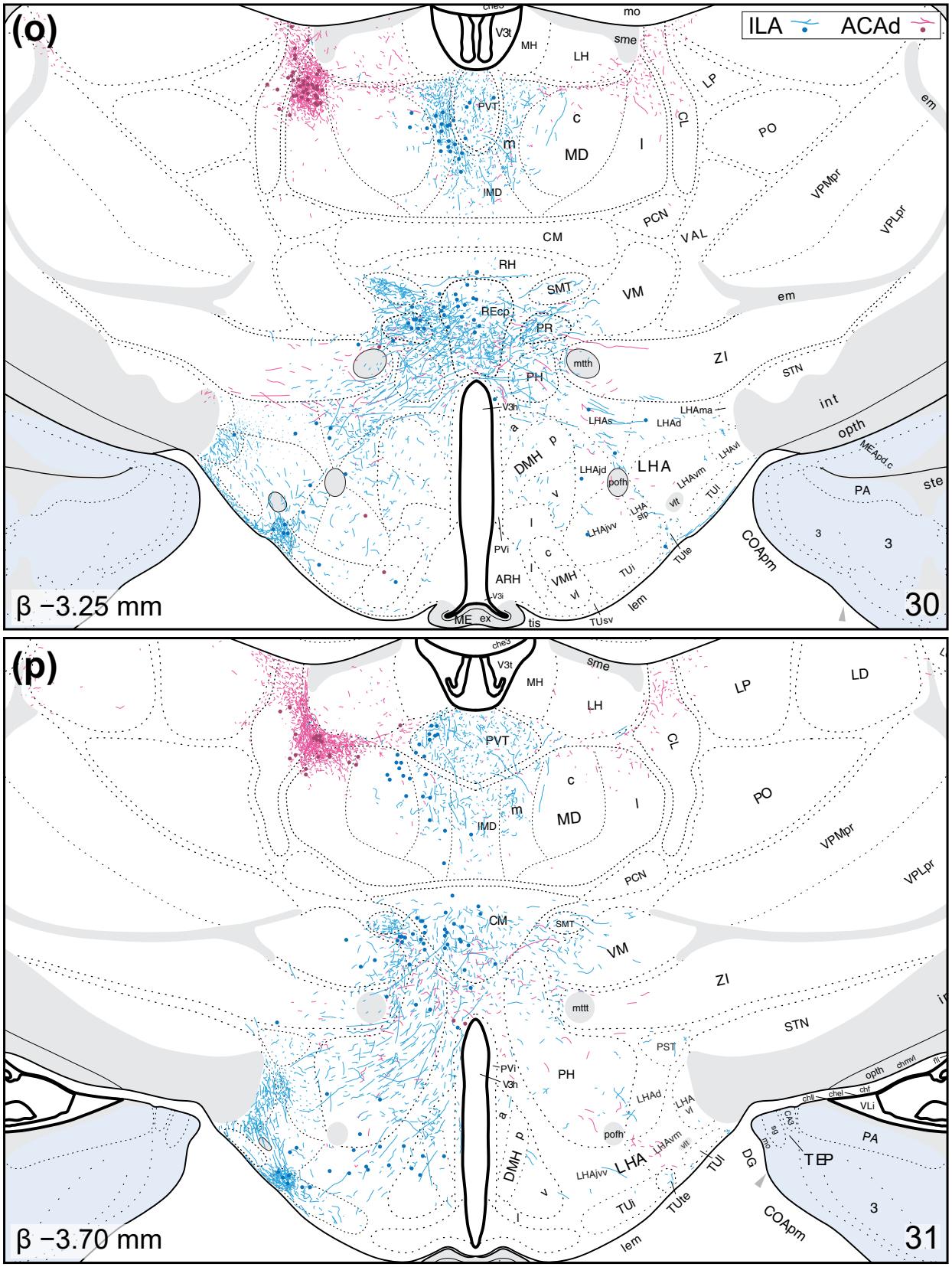

Figure 3 continued.

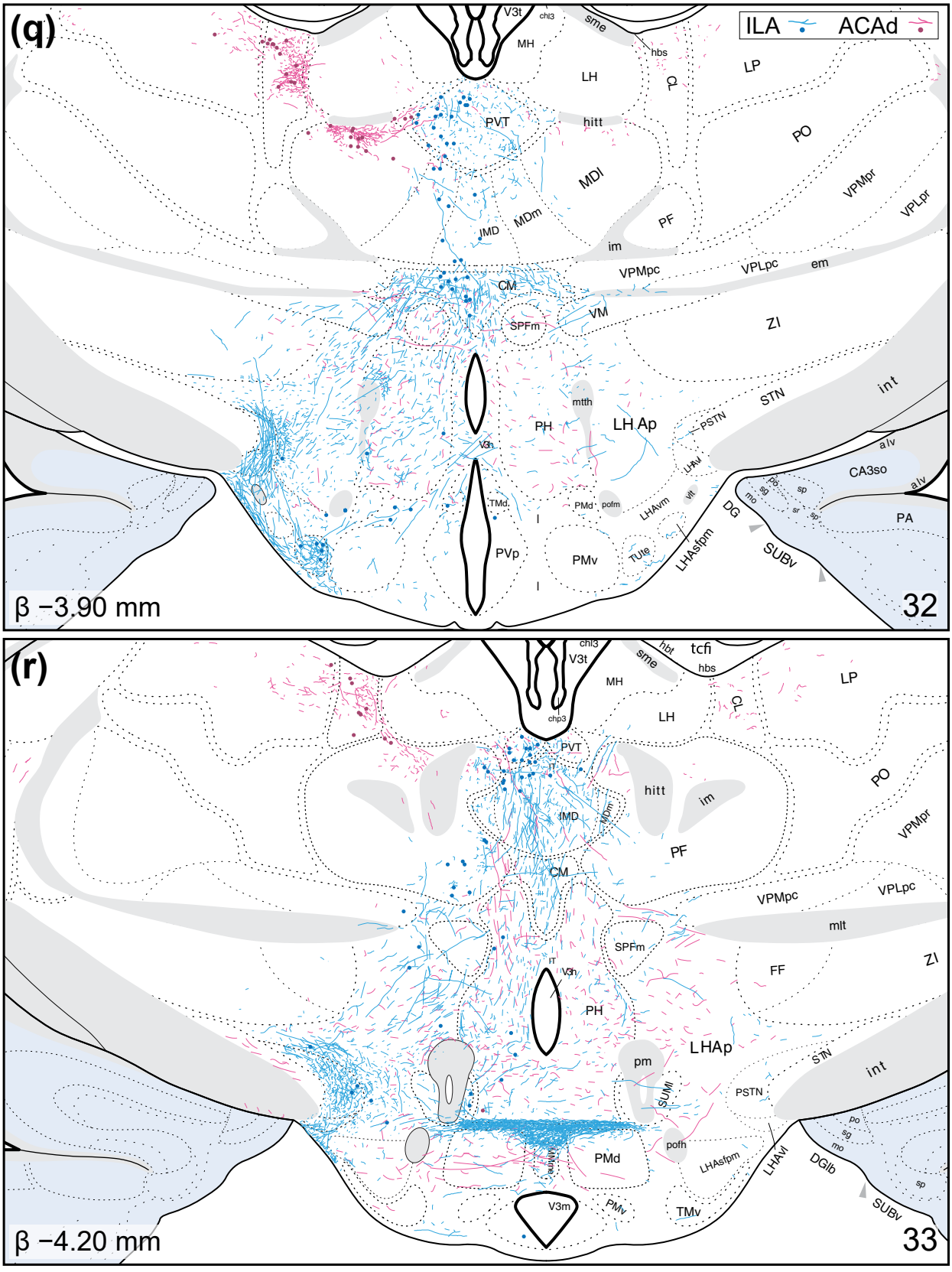

Figure 3 continued.

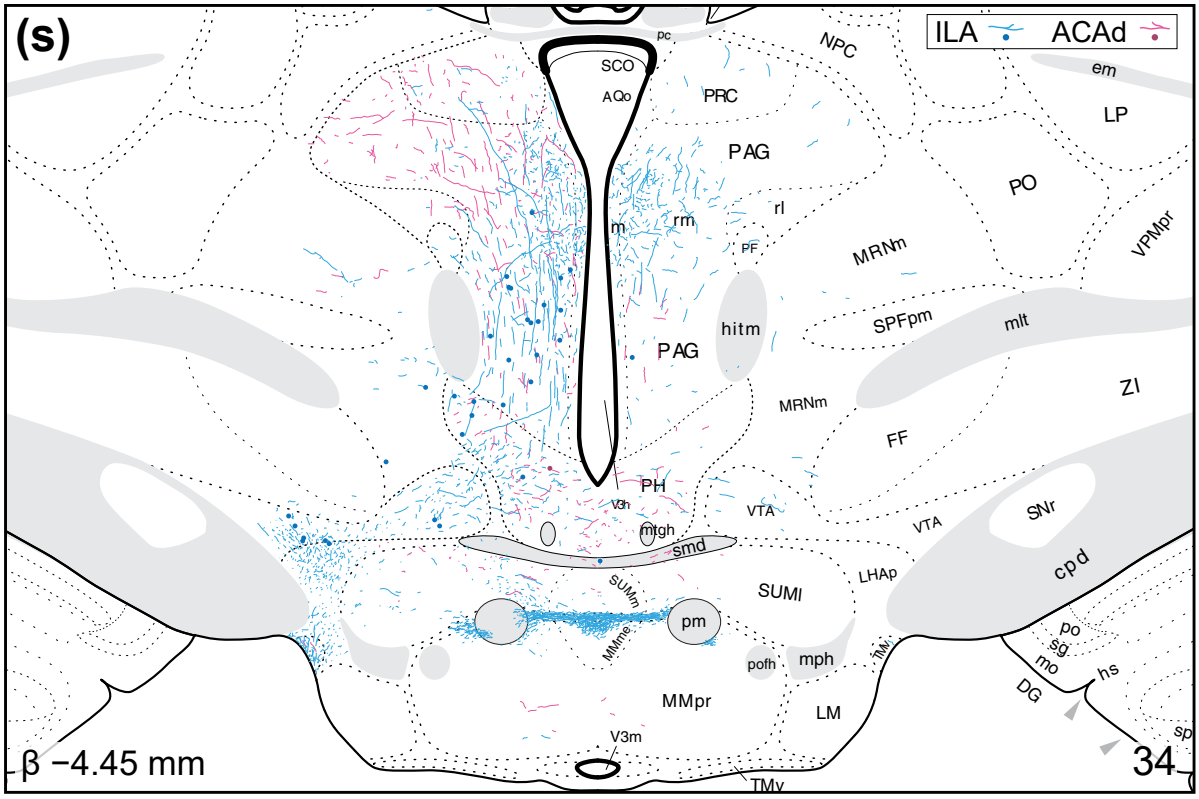

Figure 3 continued.

mostly contained retrograde labeling of AM.

There were a few examples of unidirectional connectivity among mPFC connections with thalamus. ILA axons to the SMT were densely concentrated in its ventral and caudal halves (**Fig. 3l**–**p**). Retrograde labeling from ILA was almost absent in this structure. The RH, by contrast, mostly contained retrograde labeling from ILA whereas anterograde labeling was sparse (**Fig. 3k**–**o**). Finally, ACAd axons were observed in the ZI, primarily appearing to be fibers of passage (**Fig. 3k**–**o**). ZI afferents to ACAd, however, were rarely observed in our experiments. In contrast to this, ZI showed retrograde labeling from the ILA with little indication of PHAL-ir axon terminals.

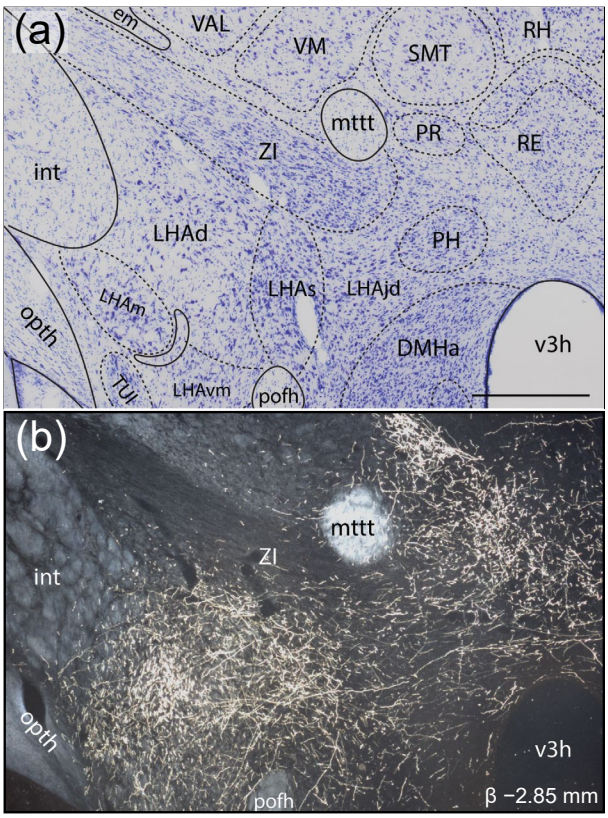

Figure 4. Photomicrographs showing PHAL-ir axons from the ILA in the dorsal (LHAd) and suprafornical (LHAs) regions of the lateral hypothalamic area. **(a)** Adjacent Nissl-stained section with boundaries and terminology based on Swanson (2018). **(b)** Darkfield photomicrograph showing PHAL-ir axons. Spatial alignment, labels, and scalebar were derived from the reference Nissl-stained section in (a). Scalebar: 500 µm. See **Table 1** for abbreviations.

Discussion

In this study, we co-injected anterograde and retrograde tracers to describe the structural organization of bidirectional macro-connections between the mPFC and diencephalon. We produced, to our knowledge, the highest spatial resolution maps for ILA and ACAd connectivity to date. This enabled a precise mapping of connectional topography and descriptions within challenging and poorly differentiated structures, such as the lateral hypothalamic zone. Each identified gray matter connection was then compared with peer reviewed datasets to establish a degree of coherence within the mPFC pathway tracing literature. Our maps, in addition to being largely harmonious with the existing literature, emphasize the relevance of connectional topography and reciprocity towards the study of mPFC and motivated behaviors.

Methodological considerations

Pathway tracing can be done with a wide variety of tracers, each with different sensitivities, effective time windows, and uptake mechanisms. There is some discussion about the variable efficacies of tracers (Bota et al., 2003; Lanciego and Wouterlood, 2006), but little work has been done to systematically compare and validate them (Ter Horst et al., 1984; Wang et al., 2014; Calabrese et al., 2015). The tracer combination

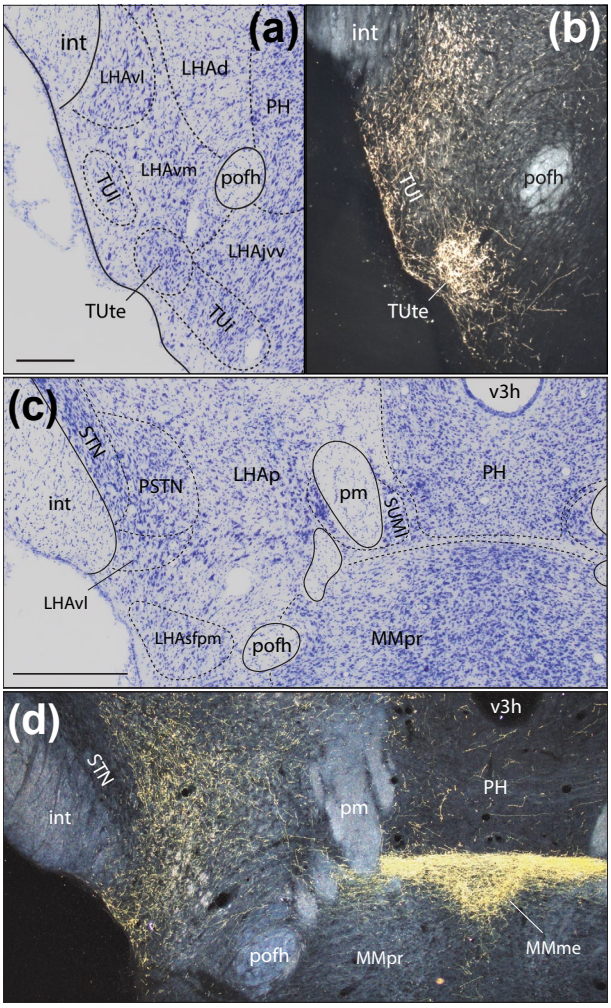

Figure 5. Photomicrographs showing PHAL-ir axons from the ILA (experiment # 15-113) in the terete part (TUte) of the tuberal nucleus **(a, b)**, the parastriatal nucleus (PSTN) and median part (MMme) of the medial mammillary nucleus **(c, d)**. Adjacent Nissl-stained sections showing the TUte **(a)** and PSTN **(c)**. Boundaries and terminology were based on Swanson (2018) and superimposed on darkfield photomicrographs showing PHAL-ir axons in the TUte **(b)**, PSTN and MMme **(d)**. Scalebars: 200 µm in (a); 500 µm in (c). See **Table 1** for abbreviations.

of PHAL and CTB used here was based on their resistance to uptake by fibers-of-passage. PHAL uptake preferentially occurs through dendrites and possibly cell bodies; with rare exceptions, PHAL is only transported in the anterograde direction (Gerfen and Sawchenko, 1984). From all of our experiments, only a single retrogradely labeled PHAL cell body was observed in the field CA1 of the hippocampus (not shown). We operated, as customarily done, with the assumption that PHAL-labeled axons detected in the diencephalon originated from mPFC cell bodies that were clearly filled with PHAL. CTB transport, by contrast, is known to have both anterograde and retrograde properties (Luppi et al., 1990). Uptake by damaged fibers-of-passage has not been shown to occur for CTB and the necrosis dealt through the injection process is largely avoided with the iontophoretic approach. Nonetheless, the mPFC and cortex in general is not recognized as a route for passing fibers. We can therefore conclude that the caveats associated with our anterograde tracers are not relevant to this study.

Atlas-based mapping was used here to localize injection sites and tracer transport. This was achieved using the cytoarchitectonic definitions of gray matter regions described

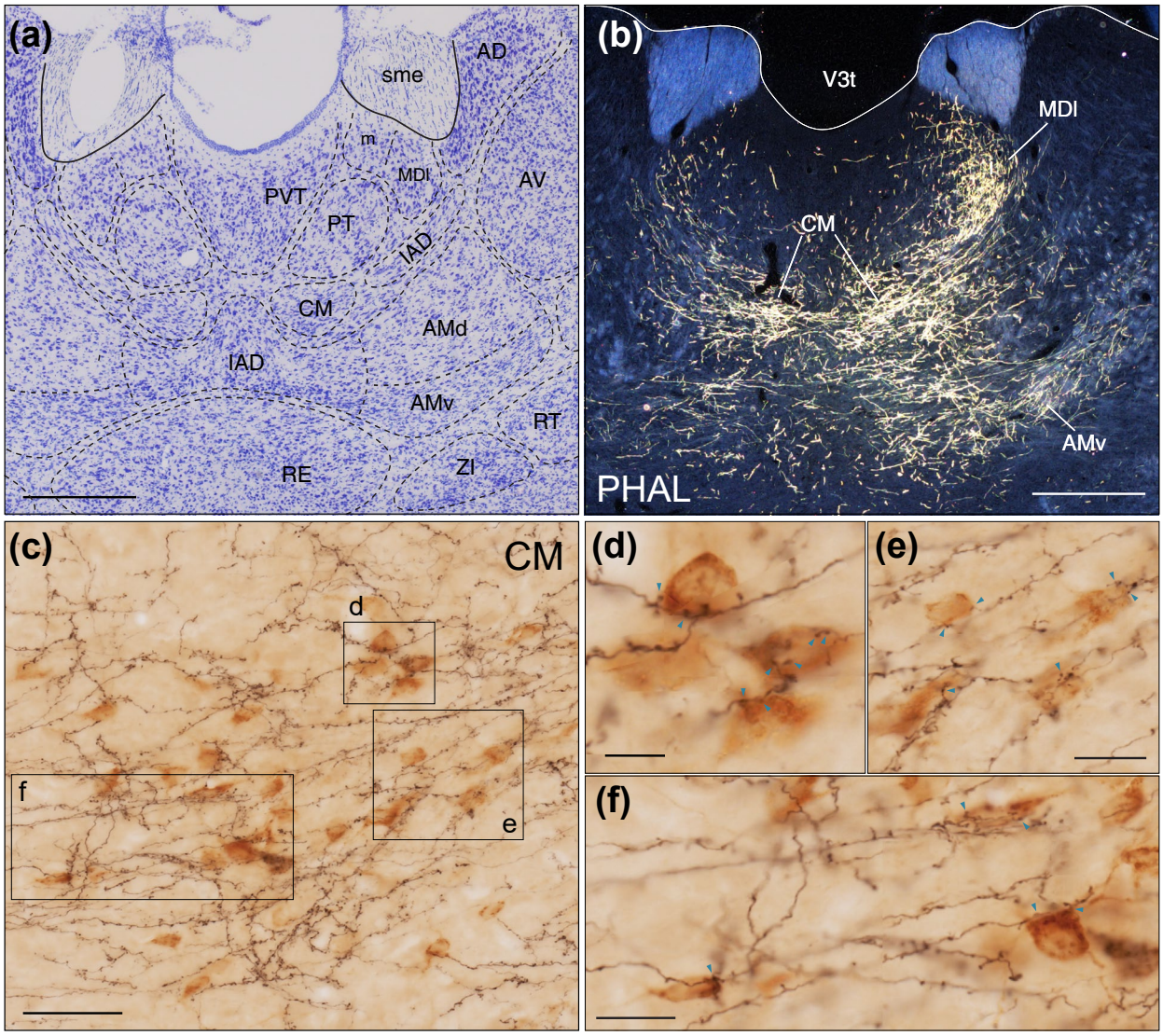

Figure 6. Photomicrographs showing ACAd axons (experiment #15-131) in rostral thalamus and the formation of putative monosynaptic reciprocal connectivity in the central medial nucleus (CM). **(a)** Adjacent Nissl-stained photomicrograph showing superimposed boundaries and regional terms based on Swanson (2018). **(b)** Darkfield photomicrographs showing labeling in the CM, mediodorsal and anteromedial nuclei based on the Nissl stain in (a). **(c)** Extended-focus image showing PHAL-ir axons (black) and CTB-ir neurons (brown) in the CM captured with ×100 objectives. **(d, e, f)** Mosaics made with single z-plane images to show putative appositions (blue arrowheads) from regions indicated in (c). Scalebars: 500 µm in (a) and (b); 50 µm in (c); 10 µm in (d); 20 µm in (e) and (f). See **Table 1** for abbreviations.

in Brain Maps 4.0 (Swanson, 2018). Nissl-defined boundaries are advantageous because they facilitate stable and unambiguous representations of histological data, allowing us to locate and precisely relate the same anatomical space from several brains. We leveraged this to represent all of our findings with atlas-level precision. The approach itself has been widely used to represent anatomical information and some recent advances in the

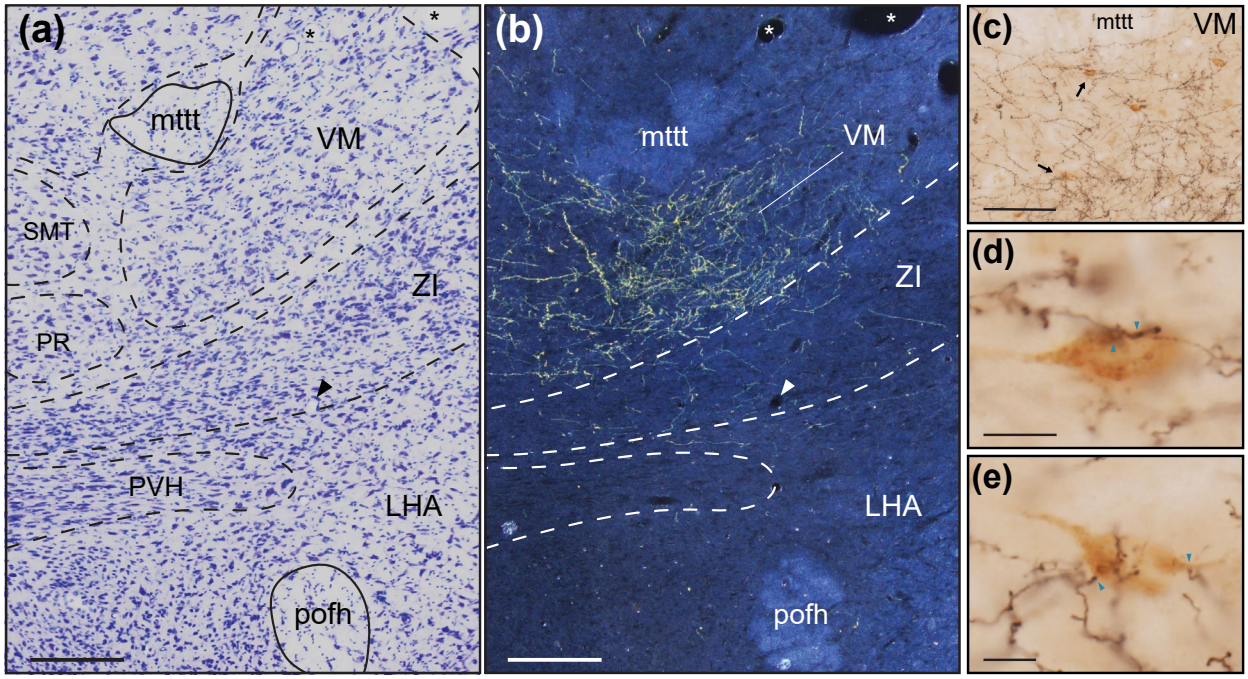

Figure 7. Photomicrographs showing ACAd axon terminals (experiment #15-131) in a rostromedial part of the ventral medial thalamic nucleus (VM), and not the zona incerta (ZI). **(a)** Adjacent Nissl-stained photomicrograph showing superimposed boundaries and regional terms based on Swanson (2018). **(b)** Darkfield photomicrographs showing labeling in the VM immediately ventral to the thalamic mammillothalamic tract (mttt). Asterisks and arrowheads in (a) and (b) show common vasculature between both sections. **(c)** Extended-focus image showing PHAL-ir axons (black) and CTB-ir neurons (brown) in the VM captured with ×100 objectives. **(d, e)** Mosaics made with single z-plane images to show putative appositions (blue arrowheads) on neurons indicated with arrows in (c). Scalebars: 200 µm in (a) and (b); 100 µm in (c); 10 µm in (d) and (e). See **Table 1** for abbreviations.

use and development of metadata analysis tools should be highlighted. Cytoarchitectonic regularity is such that stereotaxic coordinates can be inferred from them (Khan et al., 2018) and datasets derived from different brains can be combined (Khan, 2013). The latter feature was well-represented in a study that combined gene expression and connectional data to describe a subregional architecture of the hippocampus (Bienkowski et al., 2018). Combination of anatomical datasets was also instrumental for a recent series of connectomic studies (Bota et al., 2015; Swanson et al., 2016; Swanson et al., 2017; Swanson et al., 2018; Hahn et al., 2019; Swanson et al., 2019a; Swanson et al., 2019b). Such metadata analyses necessitate the use of a standardized and hierarchically organized nomenclature system (Swanson, 2018). Maps shown here satisfy these criteria

and they show connectional information at atlas-level resolution.

Comparison of findings with other tract-tracing studies

Input and output connections of the rat mPFC are among the most intensely studied. Decades of research involving several successions of pathway-tracing strategies have described the general features of mPFC connections (Nauta, 1964; Domesick, 1969; Krettek and Price, 1977; Brittain, 1988; Sesack et al., 1989; Hoover and Vertes, 2007). However, previous studies did not represent mPFC connectivity bidirectionally or achieve a similar level of spatial resolution. Doing so allowed us to observe mPFC connections in the diencephalon with high subregional precision.

In the following sections, we describe how our work aligns with other pathway tracing studies that involved injections into the mPFC or diencephalon. Several reports have examined ILA efferents throughout the diencephalon using the PHAL method (Brittain, 1988; Sesack et al., 1989; Hurley et al., 1991; Vertes, 2004) but fewer PHAL studies have focused on ACAd efferents (Sesack et al., 1989), though there is some coverage achieved with the biotinylated dextran amine method (Balfour et al., 2006). mPFC afferents from the diencephalon are best captured by a retrograde study using Fluoro-Gold (Hoover and Vertes, 2007) and an earlier report involving Diamidino Yellow and True Blue (Condé et al., 1995). The above reports, despite differences in methodologies, were remarkably well-aligned with our findings.

Hypothalamus

mPFC connections with the hypothalamus were predominantly observed in our ILA injections and they favored a top-down direction (**Table 3**). As in thalamus, mPFC axons were commonly observed bilaterally but were always less dense on the contralateral side. mPFC inputs from hypothalamus did show contralateral innervation, a feature not applicable to thalamus (**Figure 3**). For simplicity, we will discuss our findings for hypothalamus across three major divisions: The periventricular (HYp), medial (HYm), and

lateral (HYl) zones (Swanson, 2015).

Periventricular hypothalamic zone (HYp)

mPFC connections with the periventricular hypothalamic zone (HYp) tended to be weak in both directions. In general, connectivity in the HYp took the form of diffuse, low density ILA axons with only a few retrogradely labeled cells. Retrograde studies support our observed ILA and ACAd projections for the MEPO (Saper and Levisohn, 1983), PV anterior zone (PVaa) (De Haro, 2015), MPO (Kita and Oomura, 1982; Chiba and Murata, 1985), ARH (Magoul et al., 1993a, 1993b; Martinez, 2017), DMH (Thompson and Swanson, 1998), PH (Abrahamson and Moore, 2001). Retrograde labeling from the mPFC was sparse in the HYp. The few ILA afferents found in a caudal and ventral part of the DMH were not supported by other retrograde studies in the ILA (Condé et al., 1995; Hoover and Vertes, 2007); likewise, PHAL injections into the DMH did not produce labeling of the mPFC (ter Horst and Luiten, 1986; Thompson et al., 1996). mPFC inputs from the PH are, in part, supported by one PHAL study (Vertes et al., 1995).

The PVH is an especially confounding structure. It is a small, neurochemically diverse region that contains a plurality of subdivisions (Simmons and Swanson, 2009b; Biag et al., 2011). PVH connectivity is likewise difficult to resolve. Our preparations showed ILA axons throughout the PVH (**Figure 3**), a finding that is in agreement with other PHAL studies (Brittain, 1988; Sesack et al., 1989; Vertes, 2004) but others, including several retrograde studies of the PVH, have not reported labeling in the mPFC (Silverman et al., 1981; Sawchenko and Swanson, 1983; Hurley et al., 1991; De Haro, 2015).

Medial hypothalamic zone (HYm)

mPFC connections in the HYm tended to follow the same diffuse, low densities as in the HYp (**Table 3**). Light ILA innervation of the MPN was consistent with one retrograde tracing study (Simerly and Swanson, 1986). We did not observe MPN subdivision specificity but another investigation showed dense ILA axons in the lateral part of the MPN (Brittain,

1988). Retrograde tracing, in the present and other reports, have not shown transport to the MPN (Condé et al., 1995; Hoover and Vertes, 2007). However, PHAL injections into the MPN showed terminals in layer 6 of the ILA (Simerly and Swanson, 1988). Most anterograde studies showed ILA projections to the AHN (Brittain, 1988; Hurley et al., 1991; Vertes, 2004); there were no retrograde tracing studies in the AHN, to our knowledge, that corroborate this. CTB labeling of AHN was not observed in our experiments, the same lack of labeling was observed in one other retrograde tracer study (Condé et al., 1995). There are nonetheless at least two reports that show AHN projections to the ILA (Risold et al., 1994; Hoover and Vertes, 2007). Our work and others have not identified mPFC projections to the VMH (Brittain, 1988; Hurley et al., 1991; Vertes, 2004; Toth et al., 2010; Shimogawa et al., 2015). We did, however, observe retrograde labeling in the VMH from CTB injections in ILA and ACAd. This finding has some support (Condé et al., 1995; Canteras et al., 1994) but VMH projections to the mPFC were largely not observed in other studies (Saper et al., 1976; Krieger et al., 1979; Hoover and Vertes, 2007; Shimogawa et al., 2015). Retrograde labeling was not detected in the ventral mammillary nucleus (PMv) although its projections to the ILA have been described (Canteras et al., 1992), this may be due to a slight spillover of injected PHAL into the TUte laterally.

The medial mammillary nucleus (MM) contained the densest ILA terminals observed. We have localized this to a dorsal part of the MM, specifically the MMme, and not the more caudal SUM (**Figure 5c, d**). Our observations, of both the localization and density of this terminal, were also demonstrated with WGA-HRP injections into the mPFC by Allen and Hopkins (1989). Subsequent retrograde tracers deposited into the MM showed that these projections almost exclusively originated from a part of the ILA that corresponded to the “dorsal peduncular cortex” (Paxinos and Watson, 2014). This projection is not described in the majority of ILA pathway tracing studies (Sesack et al., 1989; Vertes, 2004) but the same conclusion was reached by one other group (Hurley et al., 1991).

Lateral hypothalamic zone (HYl)

mPFC projections to the LPO have been described in some detail in anterograde tracing studies (Brittain, 1988; Hurley et al., 1991; Vertes, 2004), but we were unable to locate complementary retrograde studies of the LPO to support these observations in the rat. LPO outputs to the mPFC shown here are supported by at least two other reports (Swanson, 1976; Hoover and Vertes, 2007). The LHAa contained the most retrograde labeling in the hypothalamus. This can also be observed in maps produced by Vertes (2004) but here we localized it to the LHAa and, more precisely, to its ventral region (LHAav). Unfortunately, the input and output connections of the LHAa have not been studied in much detail. We were only able to locate one study that reported ILA projections to the LHAav (Thompson and Swanson, 2010) and a PHAL study showed that a medial part of LHAav did not project to mPFC (Canteras et al., 2011). One study in mice recently showed bidirectional connectivity between mPFC and both LPO and LHAa (Hahn et al., 2022). Their experiments showed preferential connectivity with ventral mPFC predominantly with the LHAa.

Connections found in the LHAjv were well-supported by other reports (Gabbot et al., 2005; Hoover and Vertes, 2007; Hahn and Swanson, 2015; Reppucci and Petrovich, 2016). mPFC connections with the LHAjp and LHAjd were also in line with other tract tracing studies (Condé et al., 1995; Gabbot et al., 2005; Yoshida et al., 2006; Hahn and Swanson, 2010, 2012). ILA and ACAd projections to the subfornical region were supported in studies that covered a wide portion of the LHA with retrograde injections (Gabbott et al., 2005; Repucci and Petrovich, 2016). Projections to the LHAs were confirmed with small injections of retrograde tracers (Yoshida et al., 2006; Hahn and Swanson, 2010). mPFC afferents from the subfornical region were shown in the LHAsfa (Goto et al., 2005) but a small injection to the LHAs failed to produce any anterograde labeling in the mPFC (Hahn and Swanson, 2010).

We have demonstrated a dense and restricted ILA projection to the TUte (**Fig.**

5a, b). This projection was noted in an ILA study by Hurley et al. (1991), but it was not ascribed to the TUte (see their Figure 5D). mPFC projections to the tuberal nucleus have received little attention compared to the rest of the hypothalamus. Only one report incidentally labeled the TUl as part of an injection covering the ventral half of the LHA (Repucci and Petrovich, 2016). mPFC afferents from TUi and TUte were demonstrated in one PHAL study (Canteras et al., 1994).

The ventral region of the LHA has received little attention and, consequently, none of the connections described here have LHAv injections to compare with. There is strong agreement with other mPFC tracing studies (Brittain, 1988; Hurley et al., 1991; Vertes, 2004) but LHA projections in the mPFC have not been described with clear attention to this structure (Condé et al., 1995; Hoover and Vertes, 2007).

We described the morphology of ILA axons in the LHAd, where numerous mfb collaterals were formed and bore the characteristics of axon terminals (**Fig. 3l**–**n**). Several retrograde tracing studies support this with large injections into LHA (Hurley et al., 1991; Gabbott et al., 2005; Yoshida et al., 2006) and small PHAL and CTB co-injections restricted to the LHAd revealed retrograde but not anterograde labeling in the mPFC (communications with J. D. Hahn and V. I. Navarro).

Another set of dense mPFC collaterals was observed in the PSTN and LHAp (**Fig. 3q, r**). The existence of ILA terminals in the PSTN has been mentioned but not shown in a retrograde study of the PSTN (Chometton et al., 2015). We additionally noted a few retrogradely labeled PSTN neurons from CTB injections to the ILA. These were not detected in other retrograde studies of the mPFC (Condé et al., 1995; Hoover and Vertes, 2007) but Goto and Swanson (2004) reported, with anterograde injections into the PSTN, that its projections were remarkably specific to the ILA. We showed ACAd axons in the STN. Canteras et al. (1990) likewise showed ACAd projections to a caudal part of the STN.

Although we demonstrated remarkable specificity in mPFC projections to the

hypothalamus, it is important to note that a failure to discover mPFC axons within a given nucleus should not constitute an absence of connectivity. It is understood that hypothalamic neurons can form long dendrites that extend well beyond their nuclear boundaries (Millhouse, 1969).

Thalamus

Our discussion of mPFC connections with thalamus is divided according to its two major divisions: The ventral and dorsal parts (Swanson, 2015).

Ventral part of thalamus (THv)

ACAd and ILA projections to the ZI were observed in several retrograde studies (Mitrofanis and Mikuletic, 1999; Chometton et al., 2017; Chou et al., 2018). However, our demonstration of dense ACAd and ILA terminals in dorsally and ventrally adjacent areas highlights an important interpretive caveat; specifically, that slight spillover of tracers or infused compounds could result in effects that are not specific to ZI. ACAd terminals in ZI are nevertheless supported by at least two reports that used anterograde tracers (Mitrofanis and Mikuletic, 1999; Balfour et al., 2006). Retrograde labeling from the mPFC to the ZI reported here were previously shown (Condé et al., 1995; Hoover and Vertes, 2007); but anterograde studies of the ZI failed to produce mPFC labeling (Wagner et al., 1995; Sita et al., 2007), possibly due to the locations of deposited tracers. mPFC projections to the RT were demonstrated here with ACAd injections. This connection is corroborated by one retrograde tracer study of the RT (Cornwall et al., 1990).

Dorsal part of thalamus (THd)

The midline thalamic nuclei are among the most interconnected with the mPFC. Every subdivision of the RE was bidirectionally connected with the ILA in moderate or high densities, as shown in other reports (Van der Werf et al., 2002; Vertes, 2002; McKenna and Vertes, 2004; Vertes et al., 2006; Varela et al., 2014). ILA tracing labeled the PVT bidirectionally, consistent with a number of studies (Groenewegen, 1988; Chen and Su,

1990; Berendse and Groenewegen, 1991; Hurley et al., 1991; Moga et al., 1995; Van der Werf et al., 2002; Vertes, 2002; Gabbott et al., 2005; Vertes and Hoover, 2008). However, the same caveat offered for ZI is applicable here as PVT is surrounded by regions that are strongly connected with ILA. Bidirectional connectivity between the PT and both ILA and ACAd was evident from previous work as well (Berendse and Groenewegen, 1991; Chen and Su, 1990; Van der Werf et al., 2002; Vertes, 2002; McDonald et al., 1999; Vertes and Hoover, 2008; Varela et al., 2014).

Anterior thalamic nuclei were mainly connected with the ACAd. Bidirectional connectivity between the AM and ACAd has been shown previously (Shibata, 1993; van Groen et al., 1999; Shibata and Naito, 2005) with its ventral part being the most strongly connected (Vertes, 2002; Hoover and Vertes, 2007; de Lima et al., 2017). ACAd injections from other reports also revealed slightly less dense connections with the IAM (Vertes, 2002; Hoover and Vertes, 2007) and the IAD (Vertes, 2002).

The medial thalamic nuclei are also well-connected with the mPFC. Bidirectional connectivity with the PR, with a pronounced topographic organization, is in line with other studies (Van Der Werf, 2002; Vertes, 2002; Hoover and Vertes, 2007). Our finding of dense ILA terminals in a ventrocaudal half of the SMT was observed in one other report (Hurley et al., 1991) but was absent in most studies that described ILA outputs (Brittain, 1988; Sesack et al., 1989; Vertes, 2002, 2004). This difference is likely due to our inclusion of a more caudal and ventral portion of the ILA than typically observed in studies of this region. This conclusion is supported by an investigation of SMT that reported retrograde labeling in the ventral half of the caudal ILA but not in the TTd (Yoshida et al., 1992). mPFC connections with the MD and IMD have been examined in several earlier reports (Leonard, 1969; Krettek and Price, 1977; Groenewegen, 1988) but none have highlighted the extent of spatial overlap between input and output connections (**Fig. 3j**–**r**); moreover, the precise topographic organization of MD connections has yet to be characterized.

Intralaminar thalamic nuclei were variably connected with the mPFC and exhibited

pronounced spatial topography (**Fig. 3k**–**r**). In agreement with other studies, the rostral CM showed strong, bidirectional connectivity with the ACAd (**Figure 6**) (Berendse and Groenewegen, 1991; Vertes, 2002; Van der Werf, 2002; Vertes et al., 2012). CM projections to the ILA arose from slightly more caudal parts (Van der Werf, 2002; Hoover and Vertes, 2007; Vertes et al., 2012). ILA retrograde labeling identified RH projections; these were previously shown to only target the ventral ILA (Van der Werf, 2002). A few anterograde studies focused on the CL did not identify projections to the ACAd (Van der Werf, 2002; Wang and Shyu, 2004). This can be explained by the locations of CL injections, which were ventral and rostral to the parts where we observed retrograde labeling (**Fig. 3m**–**r**; Vertes, 2002; Hoover and Vertes, 2007). Anterograde and retrograde tracing of the PF did not show connectivity with the mPFC (Cornwall and Phillipson, 1988; Berendse and Groenewegen, 1991; Van der Werf, 2002). We, and others, have shown low density ILA and ACAd connections with the PF in its more dorsal and medial parts (Condé et al., 1995; Vertes, 2002; Hoover and Vertes, 2007).

A few ventral thalamic nuclei were shown to be connected with the ACAd. ACAd inputs and outputs to the VAL have been shown by others (Vertes, 2002; Hoover and Vertes, 2007), but our preparations only showed bidirectional ACAd connectivity restricted to a rostral aspect of the VAL (**Fig. 3k, l**). Previously described ACAd inputs from the VM were identified here (Hoover and Vertes, 2007), but were present well within the VM (Vertes, 2002; Balfour et al., 2006). We observed dense ACAd terminals immediately ventral to the mammillothalamic tract (**Fig. 3l, m** and **Figure 7**), this connection was noted in one other study and was interpreted as part of the RE (Vertes, 2002).

Finally, mPFC connections with the epithalamus were previously described (Vertes, 2002; Kim and Lee, 2012). We found ILA and mainly ACAd projections terminating in similar parts of the LH.

Networks, second-order connections

Recent work has focused on the assembly of connectomes based on data curated

from the tract tracing literature. So far, this project has examined the cerebral cortex (Bota et al., 2015; Swanson et al., 2017, 2018), cerebral nuclei (Swanson et al., 2016, 2018), diencephalon (Hahn et al., 2019; Swanson et al., 2019a, 2019b), and midbrain (Swanson et al., 2021). Modularity analysis performed on connectomes for cerebral cortex and cerebral nuclei ("basal ganglia") structures consistently placed the ILA and ACAd in separate modules (Swanson et al., 2018). The ILA was grouped in a module that was associated with somatic and visceral information whereas the ACAd was associated with the default mode network (DMN) (Swanson et al., 2018). In agreement with this, recent work has shown that chemogenetic silencing of the ACAd altered DMN activity, resulting in less time spent sitting still and more time engaging in rearing (Tu et al., 2020). A more recent analysis of the forebrain connectome placed the ILA in a subsystem that supports pheromonal sensorimotor functions while the ACAd contributes to a subsystem that supports voluntary eye and nose movements (Swanson et al., 2020). The forebrain connectome was arranged into two subsystems at the highest level. One subsystem was associated with voluntary control of behaviors and the second with innate survival behaviors and physiology (Swanson et al., 2020). Intriguingly, these subsystems were respectively associated with the lateral forebrain bundle (internal capsule) and mfb. This finding aligns remarkably well with our description of fiber systems used by ACAd and ILA projections.

Connectomes do well to illustrate that regions can leverage second-order connections when direct projections are not available. Several instances of this have been reported for mPFC. For example, we and others have shown weak ILA projections to the PVH (Vertes, 2004), a region directly involved in the release of signals regulating hormone secretion from the pituitary gland (Swanson and Sawchenko, 1983). Unexpectedly, lesions delivered to the mPFC increased PVH activation following restraint stress, likely due to a reduction in excitatory tone from mPFC inputs to PVH-projecting GABA neurons in the BST (Radley et al., 2009). Similarly, mPFC connections with the suprachiasmatic

hypothalamic nucleus are virtually absent (**Figure 3**). A transneuronal tracing study demonstrated a disynaptic input from the SCH to the ILA that involved a relay through the PVT (Sylvester et al., 2002).

ACAd outputs to the hypothalamus are sparse. They instead target the thalamus in places distinguishable from ILA terminals. The AM is reciprocally connected with the ACAd (**Figs. 3j, k**). This region, in turn, projects to the mPFC, anteromedial and posteromedial visual areas, perirhinal area, retrosplenial area, presubiculum, lateral part of the entorhinal area, temporal association areas, all members of the so-called default mode network in rats (Lu et al., 2012; de Lima et al., 2017). Interestingly, each of these cortical areas also receive direct projections from the ACAd (Vogt and Miller, 1983; Jones et al., 2005; Jones and Witter, 2007; Shibata and Naito, 2008). These connectional features suggest that the ACAd is strongly interconnected with members of the default mode network through both direct (cortico-cortical) and indirect (corticothalamic) pathways.

In addition to polysynaptic connections, mPFC and other cortical outputs can participate in parallel and convergent pathways (Swanson, 2000). ILA projections directly target the LHAa (**Figure 3**) and a dorsomedial part of the nucleus accumbens (ACB), which also projects to the LHAa (Thompson and Swanson, 2010). Similar observations were made in the bed nuclei of the stria terminalis (BST; Dong and Swanson, 2003, 2004, 2006), the central (CEAl; Barbier et al., 2018a, 2018b), medial (Canteras et al., 1995), and basomedial amygdalar nuclei (Reppucci and Petrovich, 2016) with respect to axon terminals converging on the LHAs and LHAd. This pattern of descending cortical inputs to striatal and pallidal structures, and the convergence of their projections in the hypothalamus has been hypothesized for the control of motivated behaviors (Swanson, 2000). Upon closer examination, there is a remarkable degree of spatial overlap between projections from the ILA (**Figure 3**), CEA (Barbier et al., 2018a), and BST (Dong and Swanson, 2003, 2004, 2006). Specifically, they all converged in a small part of the LHA that was consistent with the LHAs and LHAd (approx. −2.45 mm from Bregma). It is important to point out

that the LHAd is cytoarchitectonically characterized as a cell-sparse region relative to neighboring structures (Swanson, 2018). Given that ILA, CEA, BMA, and BST all formed similarly dense collaterals in the LHAd, it is plausible that cell-sparsity in this region reflects sheer space needed to form collaterals from many regions. Our description matches that of a classic Golgi study of the mfb which showed a massive group of axon collaterals exiting the mfb at roughly the same location, anteroposterior span, and orientation as those in the LHAd (Millhouse, 1969). Previous work has identified the LHAd as the region with the most hypocretin/orexin and melanin-concentrating hormone neurons (Hahn, 2010). Finally, recent functional mapping of LHA found that optic stimulation, specifically in a stereotaxic space corresponding to LHAd, was sufficient to induce feeding and self-stimulation (Urstadt and Berridge, 2020). Therefore, the provisional description of a Nissl-defined boundary between the LHAa and LHAd indicates a transition that is meaningful on connectional, neurochemical, and functional grounds.

Topography of thalamocortical connections

Models for cerebral hemisphere organization often include descriptions of parallel and segregated circuits that include components of cortex, striatum, and pallidum (Alexander et al., 1990; Swanson, 2000). At the level of cortico-striatal pathways, recent work combining tract-tracing and atlas-based mapping in the mouse delineated the dorsal striatum into 29 distinct domains on the basis of cortico-striatal projections (Hinitiryan et al., 2016). Similarly, our spatial framework allows detection of distinct topographic organization within the corticothalamic projectome (**Figure 3**). This is particularly applicable to the MD, where mPFC connections occupied minimally overlapping domains that varied across three dimensions. The topography of MD neurons projecting to the PFC has been explored (Alcaraz et al., 2016) but has yet to be done with high spatial resolution analysis or with an atlas-based framework that would allow comparisons with other neuroanatomical datasets.

Our observed ACAd connections with MDl were strikingly similar to a description

of projections from the nucleus incertus diffuse par (NId) (see Fig. 7D, E from Goto et al., 2001). NId terminals, like the ACAd axons (**Figure 7**), were clustered in a space between the mammillothalamic tract and the ZI which they referred to as the rostromedial tip of the VM (Goto et al., 2001). Both the MDl and VM project to a part of the secondary somatomotor area that is considered the “frontal eye field” in the rat (Reep et al., 1984). ACAd outputs can therefore leverage multiple thalamic regions that control visual attention.

Our co-injection studies demonstrated a remarkable degree of spatial overlap between mPFC connections in the thalamus; a similar observation was made with HRP implants in the macaque prefrontal cortex (Preuss and Goldman-Rakic, 1987). Analysis of reciprocal connections at high-magnification frequently revealed close appositions of anterogradely labeled axons on retrogradely labeled somata in the thalamus. Although this should not be taken for evidence of monosynaptic loops, it is nonetheless a structural requirement for their existence. Moreover, our observation that mPFC inputs and outputs are tightly coupled in space suggests that reciprocal loops may be a general feature of corticothalamic connections. It is still unclear how reciprocal connectivity might contribute to mPFC and thalamic functions. There is evidence that the MD contributes to attentional control by amplifying cortical activity during task engagement (Schmitt et al., 2017). Parallel and segregated loops, in this manner, may allow mPFC ensembles to self-maintain local activity during tasks. At the level of single-cell morphology, individual MD neurons are known to target multiple and widespread cortical areas (Kuramoto et al., 2016). It was also shown that individual thalamic neurons, at least those in the RH and parafascicular nucleus, formed dense terminals in the striatum in addition to the cortex (Fujiyama et al., 2019). This suggests that reciprocal connectivity between mPFC and thalamus is likely coupled with thalamostriatal and corticostriatal pathways.

Functional significance of ILA connections in the context of ingestive behaviors

ILA projections in the lateral hypothalamic zone primarily branched from the medial forebrain bundle. ILA collaterals mainly targeted dorsal parts of the LHAd and LHAs

(**Figs. 3** and **4**), both parts of LHA that are connectionally positioned to modulate ingestive behavior (Hahn and Swanson, 2010). In line with this, chemogenetic activation of the ILA was shown to induce feeding in the absence of hunger (Mena et al., 2011), ostensibly by increasing neural activation in a part of the LHA dorsal to the fornix (Mena et al., 2013). The space described roughly corresponds to the LHAs and LHAd, and may recruit H/O neurons among other populations (Mena et al., 2013). ILA stimulation is also known to increase arterial blood pressure, an effect that can be reversed by silencing the LHAd/s (Fisk and Wyss, 2000). ILA projections to this area are therefore capable of affecting motivational as well as autonomic outcomes.

ILA axons also densely innervated the PSTN more caudally (**Figure 3**). Input and output connections of the PSTN are well-described (Goto and Swanson, 2004; Chometton et al., 2015). PSTN projections heavily target hindbrain regions involved in processing gustatory and viscerosensory information as well as preganglionic parasympathetic cell groups that control autonomic responses (Goto and Swanson, 2004). The PSTN stands out as a part of the lateral zone that virtually lacks GABAergic neurons, a marked contrast with the nearby GABA-rich LHAs and LHAd (Chometton et al., 2015). It is still unclear how ILA contributes to PSTN functions. Recent work described a basal ganglia-like circuit motif which included the insular cortex, central nucleus of the amygdala, and substantia innominata (alternatively, the ‘innominate substance’ [Swanson, 2015]) (Barbier et al., 2020). Subsequent chemogenetic inhibition was used to demonstrate that PSTN activity was necessary to suppress feeding during illness and, to some extent, neophobia (Barbier et al., 2020). Here, we showed that ILA contributes substantial innervation to the PSTN. Moreover, our injection experiments and work done by Vertes (2004) show strong ILA projections to the feeding “no-go” circuit. It is therefore worth examining how ILA contributes to PSTN-mediated control of behaviors.

mPFC activity is thought to support the associative learning of—and the ability to act on—food-related cues (Petrovich, 2011). Indeed, Pavlovian conditioning depends

on an intact mPFC to trigger feeding in sated rats (Petrovich et al., 2007). Recent work has also shown that sated rats could be induced to overeat by infusing μ-opioid receptor agonists into the ventral mPFC (Mena et al., 2011). Overeating driven by associative learning and the endocannabinoid system clearly engage ventral mPFC structures, but the degree to which they share neural substrates is not well-understood. Both approaches have demonstrated selective Fos induction in H/O-ir neurons dorsal to the fornix at the level of the DMH (Petrovich et al., 2012; Mena et al., 2013). This region likely corresponds to the LHAs and LHAd, which contain a large proportion of hypothalamic H/O neurons (Swanson et al., 2005; Hahn, 2010). Here we showed that ILA projections, mostly from the caudal part, gave rise to terminal fields in the LHAs (**Fig. 3h**). The possibility of ILA projections forming monosynaptic contacts on H/O neurons has been explored in one study which found that ILA axons formed putative appositions with at least 22% of H/O cells (Yoshida et al., 2006).

Concluding Remarks

This work was inspired, in part, by the findings that mPFC could potently control feeding behaviors and hedonic processes (Mena et al., 2011; Castro and Berridge, 2017). As part of a structural complement to these findings, we provided detailed maps of mPFC connections in the diencephalon that highlight potential pathways that mediate these effects. Our maps provide sub-millimeter precision for targeting mPFC terminals. Given that optogenetic and chemogenetic manipulation of axon terminals actually affect fiber systems rather than individual terminals, mPFC “tractography” allows scrutiny of pathways that are inadvertently affected during such manipulations. A major problem in the study of prefrontal cortex is confusion in the nomenclature and boundary definitions across and within models (Laubach et al., 2018). We demonstrated that connectivity between mPFC and thalamus was predominantly reciprocal and non-overlapping in the case of ILA and ACAd. One can imagine a redefinition of mPFC boundaries based on degree of overlap

or using connectional “fingerprints.” In this sense, brain atlases would function more as stable coordinate systems in which boundaries are iteratively redrawn as we continue to understand the brain in its own language (Buzsáki, 2019).

References

Abrahamson, E. E., Moore, R. Y. (2001). The posterior hypothalamic area: chemoarchitecture and afferent connections. *Brain Res, 889*(1–2), 1–20. https://doi.org/10.1016/s0006-8993(00)03015-8

Akhter, F., Haque, T., Sato, F., Kato, T., Ohara, H., Fujio, T., Tsutsumi, K., Uchino, K., Sessle, B. J., Yoshida, A. (2014). Projections from the dorsal peduncular cortex to the trigeminal subnucleus caudalis (medullary dorsal horn) and other lower brainstem areas in rats. *Neuroscience, 266*, 23–37. https://doi.org/10.1016/j.neuroscience.2014.01.046

Alcaraz, F., Marchand, A. R., Courtand, G., Coutureau, E., Wolff, M. (2016). Parallel inputs from the mediodorsal thalamus to the prefrontal cortex in the rat. *Eur J Neurosci, 44*(3), 1972–1986. https://doi.org/10.1111/ejn.13316

Alexander, G. E., Crutcher, M. D., DeLong, M. R. (1990). Basal ganglia-thalamocortical circuits: parallel substrates for motor, oculomotor, "prefrontal" and "limbic" functions. *Prog Brain Res, 85*, 119–146. https://doi.org/10.1016/S0079-6123(08)62678-3

Allen, G. V., Hopkins, D. A. (1989). Mamillary body in the rat: topography and synaptology of projections from the subicular complex, prefrontal cortex, and midbrain tegmentum. *J Comp Neurol, 286*(3), 311–336. https://doi.org/10.1002/cne.902860303

Balfour, M. E., Brown, J. L., Yu, L., Coolen, L. M. (2006). Potential contributions of efferents from medial prefrontal cortex to neural activation following sexual behavior in the male rat. *Neuroscience, 137*(4), 1259–1276. https://doi.org/10.1016/j.neuroscience.2005.11.013

Barbier, M., Fellmann, D., Risold, P.-Y. (2018a). Characterization of McDonald's

intermediate part of the central nucleus of the amygdala in the rat. *J Comp Neurol, 526*(14), 2165–2186. https://doi.org/10.1002/cne.24470

Barbier, M., Fellmann, D., Risold, P.-Y. (2018b). Morphofunctional organization of the connections from the medial and intermediate parts of the central nucleus of the amygdala into distinct divisions of the lateral hypothalamic area in the rat. *Front Neurol, 9*, 688. https://doi.org/10.3389/fneur.2018.00688

Barbier, M., Chometton, S., Pautrat, A., Miguet-Alfonsi, C., Datiche, F., Gascuel, J., Fellman, D., Peterschmitt, Y., Coizet, V., Risold, P.-Y. (2020). A basal ganglia-like cortical-amygdalar-hypothalamic network mediates feeding behavior. *Proc Natl Acad Sci U S A, 117*(27), 15967–15976. https://doi.org/10.1073/pnas.2004914117

Berendse, H. W., Groenewegen, H. J. (1991). Restricted cortical termination fields of the midline and intralaminar thalamic nuclei in the rat. *Neuroscience, 42*(1), 73–102. https://doi.org/10.1016/0006-8993(90)91570-7

Biag, J., Huang, Y., Gou, L., Hintiryan, H., Askarinam, A., Hahn, J. D., Toga, A. W., Dong, H.-W. (2011). Cyto- and chemoarchitecture of the hypothalamic paraventricular nucleus in the C57BL/6J male mouse: A study of immunostaining and multiple fluorescent tract tracing. *J Comp Neurol, 520*(1), 6–30. https://doi.org/10.1002/cne.22698

Bienkowski, M. S., Bowman, I., Song, M. Y., Gou, L., Ard, T., Cotter, K., Zhu, M., Benavidez, N. L., Yamashita, S., Abu-Jaber, J., Azam, S., Lo, D., Foster, N. N., Hintiryan, H., Dong, H.-W. (2018). Integration of gene expression and brain-wide connectivity reveals the multiscale organization of mouse hippocampal networks. *Nat Neurosci, 21*(11), 1628–1643. https://doi.org/10.1038/s41593-018-0241-y

Bota, M., Dong, H.-W., Swanson, L. W. (2003). From gene networks to brain networks. *Nat Neurosci, 6*(8), 795–799. https://doi.org/10.1038/nn1096

Bota, M., Sporns, O., Swanson, L. W. (2015). Architecture of the cerebral cortical association connectome underlying cognition. *Proc Natl Acad Sci U S A, 112*(16),

E2093–E2101. https://doi.org/10.1073/pnas.1504394112

Brittain, D. A. (1988). The efferent connections of the infralimbic cortex in the rat. Doctoral dissertation. University of California, San Diego.

Buzsáki, G. (2019). *The brain from inside out*. Oxford: Oxford University Press. https://psycnet.apa.org/doi/10.1093/oso/9780190905385.001.0001

Calabrese, E., Badea, A., Cofer, G., Qi, Y., Johnson, G. A. (2015). A diffusion MRI tractography connectome of the mouse brain atlas and comparison with neuronal tracer data. *Cereb Cortex, 25*(11), 4628–37. https://doi.org/10.1093/cercor/bhv121

Canteras, N. S., Shammah-Lagnado, S. J., Silva, B. A., Ricardo, J. A. (1990). Afferent connections of the subthalamic nucleus: a combined retrograde and anterograde horseradish peroxidase study in the rat. *Brain Res, 513*(1), 43–59. https://doi.org/10.1016/0006-8993(90)91087-w

Canteras, N. S., Simerly, R. B., Swanson, L. W. (1992). Projections of the ventral premammillary nucleus. *J Comp Neurol, 324*(2), 195–212. https://doi.org/10.1002/cne.903240205

Canteras, N. S., Simerly, R. B., Swanson, L. W. (1994). Organization of projections from the ventromedial nucleus of the hypothalamus: a Phaseolus vulgaris-leucoagglutinin study in the rat. *J Comp Neurol, 348*(1), 41–79. https://doi.org/10.1002/cne.903480103

Canteras, N. S., Simerly, R. B., Swanson, L. W. (1995). Organization of projections from the medial nucleus of the amygdala: a PHAL study in the rat. *J Comp Neurol, 360*(2), 213–245. https://doi.org/10.1002/cne.903600203

Canteras, N. S., Ribeiro-Barbosa, E. R., Goto, M., Cipolla-Neto, J., Swanson, L. W. (2011). The retinohypothalamic tract: comparison of axonal projection patterns from four major targets. *Brain Res Rev, 65*(2), 150–183. https://doi.org/10.1016/j.brainresrev.2010.09.006

Castro, D. C., Berridge, K. C. (2017). Opioid and orexin hedonic hotspots in rat orbitofrontal

cortex and insula. *Proc Natl Acad Sci U S A, 114*(43), E9125–E9134. https://doi.org/10.1073/pnas.1705753114

Chen, S., Su, H. S. (1990). Afferent connections of the thalamic paraventricular and parataenial nuclei in the rat—a retrograde tracing study with iontophoretic application of Fluoro-Gold. *Brain Res, 522*(1), 1–6. https://doi.org/10.1016/0006-8993(90)91570-7

Chiba, T., Murata, Y. (1985). Afferent and efferent connections of the medial preoptic area in the rat: a WGA-HRP study. *Brain Res Bull, 14*(3), 261–272. https://doi.org/10.1016/0361-9230(85)90091-7

Chometton, S., Pedron, S., Peterschmitt, Y., Van Waes, V., Fellmann, D., Risold, P.-Y. (2015). A premammillary lateral hypothalamic nuclear complex responds to hedonic but not aversive tastes in the male rat. *Brain Struct Funct, 221*(4), 2183–2208. https://doi.org/10.1007/s00429-015-1038-3

Chometton, S., Charrière, K., Bayer, L., Houdayer, C., Franchi, G., Poncet, F., Fellmann, D., Risold, P.-Y. (2017). The rostromedial zona incerta is involved in attentional processes while adjacent LHA responds to arousal: c-Fos and anatomical evidence. *Brain Struct Funct, 222*(6), 2507–2525. https://doi.org/10.1007/s00429-016-1353-3

Chou, X.-L., Wang, X., Zhang, Z.-G., Shen, L., Zingg, B., Huang, J., Zhong, W., Mesik, L., Zhang, L. I., Tao, H. W. (2018). Inhibitory gain modulation of defense behaviors by zona incerta. *Nat Commun, 9*(1), 1151. https://doi.org/10.1038/s41467-018-03581-6

Condé, F., Maire-Lepoivre, E., Audinat, E., Crépel, F. (1995). Afferent connections of the medial frontal cortex of the rat. II. Cortical and subcortical afferents. *J Comp Neurol, 352*(4), 567–593. https://doi.org/10.1002/cne.903520407

Cornwall, J., Phillipson, O. T. (1988). Afferent projections to the parafascicular thalamic nucleus of the rat, as shown by the retrograde transport of wheat germ agglutinin.

Brain Res Bull, 20(2), 139–150. https://doi.org/10.1016/0361-9230(88)90171-2

Cornwall, J., Cooper, J. D., Phillipson, O. T. (1990). Projections to the rostral reticular thalamic nucleus in the rat. *Exp Brain Res, 80*(1), 157–171. https://doi.org/10.1007/bf00228857

De Haro, B. (2015). *Structural organization of the connections between neurons of the paraventricular and lateral hypothalamic regions in the adult male rat*. Master's Thesis. The University of Texas, El Paso.

de Lima, M. A., Baldo, M. V., Canteras, N. S. (2017). A role for the anteromedial thalamic nucleus in the acquisition of contextual fear memory to predatory threats. *Brain Struct Funct, 222*(1), 113–129. https://doi.org/10.1007/s00429-016-1204-2

Domesick, V. B. (1969). Projections from the cingulate cortex in the rat. *Brain Res, 12*(2):296–320. https://doi.org/10.1016/0006-8993(69)90002-x

Dong, H.-W., Swanson, L. W. (2003). Projections from the rhomboid nucleus of the bed nuclei of the stria terminalis: implications for cerebral hemisphere regulation of ingestive behaviors. *J Comp Neurol, 463*(4), 434–472. https://doi.org/10.1002/cne.10758

Dong, H.-W., Swanson, L. W. (2004). Organization of axonal projections from the anterolateral area of the bed nuclei of the stria terminalis. *J Comp Neurol, 468*(2), 277–298. https://doi.org/10.1002/cne.10949

Dong, H.-W., Swanson, L. W. (2006). Projections from bed nuclei of the stria terminalis, dorsomedial nucleus: implications for cerebral hemisphere integration of neuroendocrine, autonomic, and drinking responses. *J Comp Neurol, 494*(1), 75–107. https://doi.org/10.1002/cne.20790

Fisk, G. D., Wyss, J. M. (2000). Descending projections of infralimbic cortex that mediate stimulation-evoked changes in arterial pressure. *Brain Res, 859*(1), 83–95. https://doi.org/10.1016/s0006-8993(00)01935-1

Fujiyama, F., Unzai, T., Karube, F. (2019). Thalamostriatal projections and striosome-

matrix compartments. *Neurochem Int, 125*, 67–73. https://doi.org/10.1016/j.neuint.2019.01.024

Gabbott, P. L., Warner, T. A., Jays, P. R., Salway, P., Busby, S. J. (2005). Prefrontal cortex in the rat: projections to subcortical autonomic, motor, and limbic centers. *J Comp Neurol, 492*(2), 147–177. https://doi.org/10.1002/cne.20738

Gerfen, C. R., Sawchenko, P. E. (1984). An anterograde neuroanatomical tract tracing method that shows the detailed morphology of neurons, their axons and terminals: immunohistochemical localization of an axonally transported plant lectin, Phaseolus vulgaris leucoagglutinin (PHAL). *Brain Res, 1644*, 42–45. https://doi.org/10.1016/j.brainres.2015.12.040

Goto, M., Swanson, L. W., Canteras, N. S. (2001). Connections of the nucleus incertus. J *Comp Neurol, 438*(1), 86–122. https://doi.org/10.1002/cne.1303

Goto, M., Swanson, L. W. (2004). Axonal projections from the parasubthalamic nucleus. *J Comp Neurol, 469*(4), 581–607. https://doi.org/10.1002/cne.11036

Goto, M., Canteras, N. S., Burns, G., Swanson, L. W. (2005). Projections from the subfornical region of the lateral hypothalamic area. *J Comp Neurol, 493*(3), 412–438. https://doi.org/10.1002/cne.20764

Grill, H. J., Norgren, R. (1978). Neurological tests and behavioral deficits in chronic thalamic and chronic decerebrate rats. *Brain Res, 143*(2), 299–312. https://doi.org/10.1016/0006-8993(78)90570-x

Groenewegen, H. J. (1988). Organization of the afferent connections of the mediodorsal thalamic nucleus in the rat, related to the mediodorsal-prefrontal topography. *Neuroscience, 24*(2), 379–431. https://doi.org/10.1016/0306-4522(88)90339-9

Hahn, J. D. (2010). Comparison of melanin-concentrating hormone and hypocretin/orexin peptide expression patterns in a current parceling scheme of the lateral hypothalamic zone. *Neurosci Lett, 468*(1), 12–17. https://doi.org/10.1016/j.neulet.2009.10.047

Hahn, J. D., Swanson, L. W. (2010). Distinct patterns of neuronal inputs and outputs of the juxtaparaventricular and suprafornical regions of the lateral hypothalamic area in the male rat. *Brain Res Rev, 64*(1), 14–103. https://doi.org/10.1016/j.brainresrev.2010.02.002

Hahn, J. D., Swanson, L. W. (2012). Connections of the lateral hypothalamic area juxtadorsomedial region in the male rat. *J Comp Neurol, 520*(9), 1831–1890. https://doi.org/10.1002/cne.23064

Hahn, J. D., Swanson, L. W. (2015). Connections of the juxtaventromedial region of the lateral hypothalamic area in the male rat. *Front Syst Neurosci, 9*, 66. https://doi.org/10.3389/fnsys.2015.00066

Hahn, J. D., Sporns, O., Watts, A. G., Swanson, L. W. (2019). Macroscale intrinsic network architecture of the hypothalamus. *Proc Natl Acad U S A, 116*(16), 8018–8027. https://doi.org/10.1073/pnas.1819448116

Hahn, J. D., Gao, L., Boesen, T., Gou, L., Hintiryan, H., Dong, H.-W. (2022). Macroscale connections of the mouse lateral preoptic area and anterior lateral hypothalamic area. *J Comp Neurol, 530*(13), 2254–2285. https://doi.org/10.1002/cne.25331

Hintiryan, H., Foster, N. N., Bowman, I., Bay, M., Song, M. Y., Gou, L., Yamashita, S., Bienkowski, M. S., Zingg, B., Zhu, M., Yang, X. W., Shih, J. C., Toga, A. W., Dong, H.-W. (2016). The mouse cortico-striatal projectome. *Nat Neurosci 19*(8), 1100–1114. https://doi.org/10.1038/nn.4332

Hoover, W. B., Vertes, R. P. (2007). Anatomical analysis of afferent projections to the medial prefrontal cortex in the rat. *Brain Struct Funct, 212*(2), 149–179. https://doi.org/10.1007/s00429-007-0150-4

Hurley, K. M., Herbert, H., Moga, M. M., Saper, C. B. (1991). Efferent projections of the infralimbic cortex of the rat. *J Comp Neurol, 308*(2), 249–276. https://doi.org/10.1002/cne.903080210

Jones, B. F., Groenewegen, H. J., Witter, M. P. (2005). Intrinsic connections of

the cingulate cortex in the rat suggest the existence of multiple functionally segregated networks. *Neuroscience, 133*(1), 193–207. https://doi.org/10.1016/j.neuroscience.2005.01.063

Jones, B. F., Witter, M. P. (2007). Cingulate cortex projections to the parahippocampal region and hippocampal formation in the rat. *Hippocampus, 17*(10), 957–976. https://doi.org/10.1002/hipo.20330

Khan, A. M. (2013). Controlling feeding behavior by chemical or gene-directed targeting in the brain: what's so spatial about our methods?. *Front Syst Neurosci, 7*, 1–49. https://doi.org/10.3389/fnins.2013.00182

Khan, A. M., Perez, J. G., Wells, C. E., Fuentes, O. (2018). Computer vision evidence supporting craniometric alignment of rat brain atlases to streamline expert-guided, first-order migration of hypothalamic spatial datasets related to behavioral control. *Front Syst Neurosci, 12*, 7. https://doi.org/10.3389/fnsys.2018.00007

Kim, U., Lee, T. (2012). Topography of descending projections from anterior insular and medial prefrontal regions to the lateral habenula of the epithalamus in the rat. Eur *J Neurosci, 35*(8), 1253–1269. https://doi.org/10.1111/j.1460-9568.2012.08030.x

Kita, H., Oomura, Y. (1982). An HRP study of the afferent connections to rat medial hypothalamic region. *Brain Res Bull, 8*(1), 53–62. https://doi.org/10.1016/0361-9230(82)90027-2

Krettek, J. E., Price, J. L. (1977). The cortical projections of the mediodorsal nucleus and adjacent thalamic nuclei in the rat. *J Comp Neurol, 171*(2), 157–191. https://doi.org/10.1002/cne.901710204

Krieger, M. S., Condrad, L. C., Pfaff, D. W. (1979). An autoradiographic study of the efferent connections of the ventromedial nucleus of the hypothalamus. *J Comp Neurol, 183*(4), 785–815. https://doi.org/10.1002/cne.901830408

Kuramoto, E., Pan, S., Furuta, T., Tanaka, Y. R., Iwai, H., Yamanaka, A., Ohno, S., Kaneko, T., Goto, T., Hioki, H. (2016). Individual mediodorsal thalamic neurons project to

multiple areas of the rat prefrontal cortex: A single neuron-tracing study using virus vectors. *J Comp Neurol, 525*(1),166–185. https://doi.org/10.1002/cne.24054

Lanciego, J. L., Wouterlood, F. G. (2006). Multiple Neuroanatomical Tract-Tracing: Approaches for Multiple Tract-Tracing. In: Zaborszky, L., Wouterlood, F. G., Lanciego, J. L. (eds.) *Neuroanatomical Tract-Tracing 3*. New York: Springer. pp. 336–365.

Laubach, M., Amarante, L. M., Swanson, K., White, S. R. (2018). What, if anything, is rodent prefrontal cortex?. *eNeuro, 5*(5), ENEURO.0315-18.2018. https://doi.org/10.1523/eneuro.0315-18.2018

Leonard, C. M. (1969). The prefrontal cortex of the rat. I. Cortical projection of the mediodorsal nucleus. II. Efferent connections. *Brain Res, 12*(2), 321–343. https://doi.org/10.1016/0006-8993(69)90003-1

Lu, H., Zou, Q., Gu, H., Raichle, M. E., Stein, E. A., Yang, Y. (2012). Rat brains also have a default mode network. *Proc Natl Acad Sci U S A, 109*(10), 3979–3984. https://doi.org/10.1073/pnas.1200506109

Luppi, P. H., Fort, P., Jouvet, M. (1990). Iontophoretic application of unconjugated cholera toxin B subunit (CTB) combined with immunohistochemistry of neurochemical substances: a method for transmitter identification of retrogradely labeled neurons. *Brain Res, 534*(1–2), 209–224. https://doi.org/10.1016/0006-8993(90)90131-t

Magoul, R., Dubourg, P., Benjelloun, W., Tramu, G. (1993a). Direct and indirect enkephalinergic synaptic inputs to the rat arcuate nucleus studied by combination of retrograde tracing and immunocytochemistry. *Neuroscience, 55*(4), 1055–1066. https://doi.org/10.1016/0306-4522(93)90319-b

Magoul, R., Onteniente, B., Benjelloun, W., Tramu, G. (1993b). Tachykinergic afferents to the rat arcuate nucleus. A combined immunohistochemical and retrograde tracing study. *Peptides, 14*(2), 275–286. https://doi.org/10.1016/0196-9781(93)90042-f

Martinez A. (2017). *The metabolically sentient arcuate nucleus: A functional,*

chemoarchitectural and connectional study in the adult male rat. Doctoral dissertation. University of Texas, El Paso.

Mandelbaum, G., Taranda, J., Haynes, T. M., Hochbaum, D. R., Huang, K. W., Hyun, M., Umadevi Venkataraju, K., Straub, C., Wang, W., Robertson, K., Osten, P., Sabatini, B. L. (2019). Distinct cortical-thalamic-striatal circuits through the parafascicular nucleus. *Neuron, 102*(3), 636–652.e7. https://doi.org/10.1016/j.neuron.2019.02.035

McDonald, A. J., Shammah-Lagnado, S. J., Shi, C., Davis, M. (1999). Cortical afferents to the extended amygdala. *Ann N Y Acad Sci, 877*, 309–338. https://doi.org/10.1111/j.1749-6632.1999.tb09275.x

McKenna, J. T., Vertes, R. P. (2004). Afferent projections to nucleus reuniens of the thalamus. *J Comp Neurol, 480*(2), 115–142. https://doi.org/10.1002/cne.20342

Mena, J. D., Sadeghian, K., Baldo, B. A. (2011). Induction of hyperphagia and carbohydrate intake by μ-opioid receptor stimulation in circumscribed regions of frontal cortex. *J Neurosci, 31*(9), 3249–3260. https://doi.org/10.1523/jneurosci.2050-10.2011

Mena, J. D., Selleck, R. A., Baldo, B. A. (2013). Mu-opioid stimulation in rat prefrontal cortex engages hypothalamic orexin/hypocretin-containing neurons, and reveals dissociable roles of nucleus accumbens and hypothalamus in cortically driven feeding. *J Neurosci, 33*(47), 18540–18552. https://doi.org/10.1523/jneurosci.3323-12.2013

Mickelsen, L. E., Flynn, W. F., Springer, K., Wilson, L., Beltrami, E. J., Bolisetty, M., Robson, P., Jackson, A. C. (2020) Cellular taxonomy and spatial organization of the murine ventral posterior hypothalamus. *Elife, 9*, e58901. https://doi.org/10.7554/elife.58901

Miller, E. K., Cohen, J. D. (2001). An integrative theory of prefrontal cortex function. *Annu Rev Neurosci, 24*, 167–202. https://doi.org/10.1146/annurev.neuro.24.1.167

Millhouse, O. E. (1969). A Golgi study of the descending medial forebrain bundle. *Brain*

Res, 15(2), 341–363. https://doi.org/10.1016/0006-8993(69)90161-9

Mitrofanis, J., Mikuletic, L. (1999). Organisation of the cortical projection to the zona incerta of the thalamus. *J Comp Neurol, 412*(1),173–185. https://doi.org/10.1002/(SICI)1096-9861(19990913)412:1%3C173::AID-CNE13%3E3.0.CO;2-Q

Moga, M. M., Weis, R. P., Moore, R. Y. (1995). Efferent projections of the paraventricular thalamic nucleus in the rat. *J Comp Neurol, 359*(2), 221–238. https://doi.org/10.1002/cne.903590204

Nauta, W. J. H. (1964). Some efferent connections of the prefrontal cortex in the monkey. In: Warren, J. M., Akert, K. (eds.) *The Frontal Granular Cortex and Behavior*. New York: McGraw Hill. pp. 397–409.

Negishi, K., Hamdan, J., Khan, A. M. (2015). Initial chemoarchitectural and connectional characterization of polymodal association cortical structures with the diencephalon: Immunohistochemical and tract tracing studies. Program No. 616.14. *2015 Neuroscience Meeting Planner*. Chicago, IL. Society for Neuroscience, 2015. Online.

Negishi, K., Khan, A. M. (2017). Mapping the connections between the medial prefrontal cortex and the diencephalon: A combined anterograde and retrograde tract-tracing study in the adult male rat. Program No. 604.07. *2017 Neuroscience Meeting Planner*. Washington, DC. Society for Neuroscience, 2017. Online.

Negishi, K., Khan, A. M. (2019). The contribution of axonal projections from infralimbic area neuronal populations to the medial forebrain bundle: analysis of morphology and interactions with hypocretin/orexin neurons in the rat. Program No. 149.24. *2019 Neuroscience Meeting Planner*. Chicago, IL: Society for Neuroscience, 2019. Online.

NRC [National Research Council (US) Committee for the Update of the Guide for the Care and Use of Laboratory Animals]. (2011). *Guide for the care and use of laboratory animals*, 8th edition. Washington, D.C.: National Academies Press.

Paus, T., Zijdenbos, A., Worsley, K., Collins, D. L., Blumenthal, J., Giedd, J. N., Rapoport, J. A., Evans, A. C. (1999). Structural maturation of neural pathways in children and adolescents: in vivo study. *Science, 283*(5409),1908–11. https://doi.org/10.1126/science.283.5409.1908

Paxinos, G., Watson, C. (2014). *The Rat Brain in Stereotaxic Coordinates* (7th ed.). San Diego: Elsevier Academic Press.

Petrovich, G. D., Ross, C. A., Holland, P. C., Gallagher, M. (2007). Medial prefrontal cortex is necessary for an appetitive contextual conditioned stimulus to promote eating in sated rats. *J Neurosci, 27*(24),6436–41. https://doi.org/10.1523/jneurosci.5001-06.2007

Petrovich, G. D. (2011). Forebrain circuits and control of feeding by learned cues. *Neurobiol Learn Mem, 95*(2),152–158. https://doi.org/10.1016/j.nlm.2010.10.003

Petrovich, G. D., Hobin, M. P., Reppucci, C. J. (2012). Selective Fos induction in hypothalamic orexin/hypocretin, but not melanin-concentrating hormone neurons, by a learned food-cue that stimulates feeding in sated rats. *Neuroscience, 224*,70–80. https://doi.org/10.1016/j.neuroscience.2012.08.036

Preuss, T. M., Goldman-Rakic, P. S. (1987). Crossed corticothalamic and thalamocortical connections of macaque prefrontal cortex. *J Comp Neurol, 257*(2),269–81. https://doi.org/10.1002/cne.902570211

Radley, J. J., Gosselink, K. L., Sawchenko, P. E. (2009). A discrete GABAergic relay mediates medial prefrontal cortical inhibition of the neuroendocrine stress response. *J Neurosci, 29*(22),7330–7340. https://doi.org/10.1523/jneurosci.5924-08.2009

Reep, R. L., Corwin, J. V., Hashimoto, A., Watson, R. T. (1984). Afferent connections of medial precentral cortex in the rat. *Neurosci Lett, 44*,247–252. https://doi.org/10.1016/0304-3940(84)90030-2

Reppucci, C. J., Petrovich, G. D. (2016). Organization of connections between the amygdala, medial prefrontal cortex, and lateral hypothalamus: a single and double

retrograde tracing study in rats. *Brain Struct Funct, 221*(6),2937–62. https://doi.org/10.1007/s00429-015-1081-0

Risold, P.-Y., Canteras, N. Y., Swanson, L. W. (1994). Organization of projections from the anterior hypothalamic nucleus: a *Phaseolus vulgaris*-leucoagglutinin study in the rat. *J Comp Neurol, 348*(1),1–40. https://doi.org/10.1002/cne.903480102

Saper, C. B., Swanson, L. W., Cowan, W. M. (1976). The efferent connections of the ventromedial nucleus of the hypothalamus of the rat. *J Comp Neurol, 169*(4),409–42. https://doi.org/10.1016/j.neures.2014.10.016

Saper, C. B., Levisohn, D. (1983). Afferent connections of the median preoptic nucleus in the rat: anatomical evidence for a cardiovascular integrative mechanism in the anteroventral third ventricular (AV3V) region. *Brain Res, 288*(1–2),21–31. https://doi.org/10.1016/0006-8993(83)90078-1

Sapolsky, R. M. (2004). The frontal cortex and the criminal justice system. *Philos Trans R Soc Lond B Biol Sci, 359*(1451),1787–96. https://doi.org/10.1098/rstb.2004.1547

Sawchenko, P. E., Swanson, L. W. (1983). The organization of forebrain afferents to the paraventricular and supraoptic nuclei of the rat. *J Comp Neurol, 218*(2),121–44. https://doi.org/10.1002/cne.902180202

Schmitt, LI., Wimmer, R. D., Nakajima, M., Happ, M., Mofokham, S., Halassa, M. M. (2017). Thalamic amplification of cortical connectivity sustains attentional control. *Nature, 545*,219–223. https://doi.org/10.1038/nature22073

Sesack, S. R., Deutch, A. Y., Roth, R. H., Bunney, B. S. (1989). Topographical organization of the efferent projections of the medial prefrontal cortex in the rat: an anterograde tract-tracing study with *Phaseolus vulgaris* leucoagglutinin. *J Comp Neurol, 290*(2),213–42. https://doi.org/10.1002/cne.902900205

Shibata, H. (1993). Efferent projections from the anterior thalamic nuclei to the cingulate cortex in the rat. *J Comp Neurol, 330*(4),533–42. https://doi.org/10.1002/cne.903300409

Shibata, H., Naito, J. (2005). Organization of anterior cingulate and frontal cortical projections to the anterior and laterodorsal thalamic nuclei in the rat. *Brain Res, 1059*(1),93–103. https://doi.org/10.1016/j.brainres.2005.08.025

Shibata, H., Naito, J. (2008). Organization of anterior cingulate and frontal cortical projections to the retrosplenial cortex in the rat. *J Comp Neurol, 506*(1),30–45. https://doi.org/10.1002/cne.21523

Shimogawa, Y., Sakuma, Y., Yamanouchi, K. (2015). Efferent and afferent connections of the ventromedial hypothalamic nucleus determined by neural tracer analysis: implications for lordosis regulation in female rats. *Neurosci Res, 91*,19–33. https://doi.org/10.1016/j.neures.2014.10.016

Silverman, A. J., Hoffman, D. L., Zimmerman, E. A. (1981). The descending afferent connections of the paraventricular nucleus of the hypothalamus (PVN). *Brain Res Bull, 6*(1),47–61. https://doi.org/10.1016/s0361-9230(81)80068-8

Simerly, R. B., Swanson, L. W. (1986). The organization of neural inputs to the medial preoptic nucleus of the rat. *J Comp Neurol, 246*(3),312–342. https://doi.org/10.1002/cne.902460304

Simerly, R. B., Swanson, L. W. (1988). Projections of the medial preoptic nucleus: a *Phaseolus vulgaris* leucoagglutinin anterograde tract-tracing study in the rat. *J Comp Neurol, 270*(2),209–242. https://doi.org/10.1002/cne.902700205

Simmons, D. M., Swanson, L. W. (2009a). Comparing histological data from different brains: sources of error and strategies for minimizing them. *Brain Res Rev, 60*(2),349–367. https://doi.org/10.1016/j.brainresrev.2009.02.002

Simmons, D. M., Swanson, L. W. (2009b). Comparison of the spatial distribution of seven types of neuroendocrine neurons in the rat paraventricular nucleus: Toward a global 3D model. *J Comp Neurol, 516*(5),423–41. https://doi.org/10.1002/cne.22126

Sita, L. V., Elias, C. F., Bittencourt, J. C. (2007). Connectivity pattern suggests that incerto-hypothalamic area belongs to the medial hypothalamic system. *Neuroscience,*

148(4),949–969. https://doi.org/10.1016/j.neuroscience.2007.07.010

Swanson, L. W. (1976). An autoradiographic study of the efferent connections of the preoptic region in the rat. *J Comp Neurol, 167*(2), 227–256. https://doi.org/10.1002/cne.901670207

Swanson, L. W. (1992). *Brain Maps: Structure of the Rat Brain* (1st ed.). Amsterdam: Elsevier.

Swanson, L. W. (1998). *Brain Maps: Structure of the Rat Brain. A Laboratory Guide with Printed and Electronic Templates for Data, Models and Schematics* (2nd ed.). Amsterdam: Elsevier.

Swanson, L. W. (2000). Cerebral hemisphere regulation of motivated behavior. *Brain Res, 886*,113–164. https://doi.org/10.1016/s0006-8993(00)02905-x

Swanson, L. W. (2004). *Brain Maps: Structure of the Rat Brain* (3rd ed.). San Diego: Academic Press.

Swanson, L. W. (2015). *Neuroanatomical Terminology: A lexicon of classical origins and historical foundations*. Oxford: Oxford University Press.

Swanson, L. W. (2018). *Brain maps 4.0—Structure of the rat brain*: An open access atlas with global nervous system nomenclature ontology and flatmaps. *J Comp Neurol, 526*(6), 935–943. https://doi.org/10.1002/cne.24381

Swanson, L. W., Sawchenko, P. E. (1983). Hypothalamic integration: Organization of the paraventricular and supraoptic nuclei. *Ann Rev Neurosci, 6*, 269–324. https://doi.org/10.1146/annurev.ne.06.030183.001413

Swanson, L. W., Sanchez-Watts, G., Watts, A. G. (2005). Comparison of melanin-concentrating hormone and hypocretin/orexin mRNA expression patterns in a new parceling scheme of the lateral hypothalamic zone. *Neurosci Lett, 387*(2), 80–84. https://doi.org/10.1016/j.neulet.2005.06.066

Swanson, L. W., Sporns, O., Hahn, J. D. (2016). Network architecture of the cerebral nuclei (basal ganglia) association and commissural connectome. *Proc Natl Acad*

Sci U S A, 113(40), E5971–E5981. https://doi.org/10.1073/pnas.1613184113

Swanson, L. W., Hahn, J. D., Sporns, O. (2017). Organizing principles for the cerebral cortex network of commissural and association connections. *Proc Natl Acad Sci U S A, 114*(45), E9692–E9701. https://doi.org/10.1073/pnas.1712928114

Swanson, L. W., Hahn, J. D., Jeub, L. G. S., Fortunato, S., Sporns, O. (2018). Subsystem organization of axonal connections within and between the right and left cerebral cortex and cerebral nuclei (endbrain). *Proc Natl Acad Sci U S A, 115*(29), E6910–E16919. https://doi.org/10.1073/pnas.1807255115

Swanson, L. W., Sporns, O., Hahn, J. D. (2019a). The network architecture of rat intrinsic interbrain (diencephalic) macroconnections. *Proc Natl Acad Sci U S A, 116*(52), 26991–27000. https://doi.org/10.1073/pnas.1915446116

Swanson, L. W., Sporns, O., Hahn, J. D. (2019b). The network organization of rat intrathalamic macroconnections and a comparison with other forebrain divisions. *Proc Natl Acad Sci U S A, 116*(27), 13661–13669. https://doi.org/10.1073/pnas.1905961116

Swanson, L. W., Hahn, J. D., Sporns, O. (2020). Structure-function subsystem models of female and male forebrain networks integrating cognition, affect, behavior, and bodily functions. *Proc Natl Acad Sci U S A, 117*(49), 31470–31481. https://doi.org/10.1073/pnas.2017733117

Swanson, L. W., Hahn, J. D., Sporns, O. (2021). Subsystem macroarchitecture of the intrinsic midbrain neural network and its tectal and tegmental subnetworks. *Proc Natl Acad Sci U S A, 118*(20), e2101869118. https://doi.org/10.1073/pnas.2101869118

Sylvester, C. M., Krout, K. E., Loewy, A. D. (2002). Suprachiasmatic nucleus projection to the medial prefrontal cortex: a viral transneuronal tracing study. *Neuroscience, 114*(4), 1071–1080. https://doi.org/10.1016/s0306-4522(02)00361-5

Ter Horst, G. J., Groenewegen, H. J., Karst, H., Luiten, P. G. (1984). *Phaseolus vulgaris* leuco-agglutinin immunohistochemistry. A comparison between autoradiographic

and lectin tracing of neuronal efferents. *Brain Res, 307*(1–2), 379–383. https://doi.org/10.1016/0006-8993(84)90500-6

Ter Horst, G. J., Luiten, P. G. (1986). The projections of the dorsomedial hypothalamic nucleus in the rat. *Brain Res Bull, 16*(2), 231–248. https://doi.org/10.1016/0361-9230(86)90038-9

Thompson, R. H., Canteras, N. S., Swanson, L. W. (1996). Organization of projections from the dorsomedial nucleus of the hypothalamus: a PHAL study in the rat. *J Comp Neurol, 376*(1), 143–173. https://doi.org/10.1002/(sici)1096-9861(19961202)376:1%3C143::aid-cne9%3E3.0.co;2-3

Thompson, R. H., Swanson, L. W. (1998). Organization of inputs to the dorsomedial nucleus of the hypothalamus: a reexamination with Fluorogold and PHAL in the rat. *Brain Res Rev, 27*(2), 89–118. https://doi.org/10.1016/s0165-0173(98)00010-1

Thompson, R. H., Swanson, L. W. (2010). Hypothesis-driven structural connectivity analysis supports network over hierarchical model of brain architecture. *Proc Natl Acad Sci U S A, 107*, 15235–15239. https://doi.org/10.1073/pnas.1009112107

Toth, M., Fuzesi, T., Halasz, J., Tulogdi, A., Haller, J. (2010). Neural inputs of the hypothalamic "aggression area" in the rat. *Behav Brain Res, 215*(1), 7–20. https://doi.org/10.1016/j.bbr.2010.05.050

Tu, W., Ma, Z., Ma, Y., Dopfel, D., Zhang, N. (2021). Suppressing anterior cingulate cortex modulates default mode network and behavior in awake rats. *Cereb Cortex, 31*(1), 312–323. https://doi.org/10.1093/cercor/bhaa227

Urstadt, K. R., Berridge, K. C. (2020). Optogenetic mapping of feeding and self-stimulation within the lateral hypothalamus of the rat. *PLoS One, 15*(1), e0224301. https://doi.org/10.1371/journal.pone.0224301

van der Werf, Y. D., Witter, M. P., Groenewegen, H. J. (2002). The intralaminar and midline nuclei of the thalamus. Anatomical and functional evidence for participation in processes of arousal and awareness. *Brain Res Rev, 39*, 107–140. https://doi.

org/10.1016/s0165-0173(02)00181-9

van Groen, T., Kadish, I., Wyss, J. M. (1999). Efferent connections of the anteromedial nucleus of the thalamus of the rat. *Brain Res Rev, 30*(1), 1–26. https://doi.org/10.1016/s0165-0173(99)00006-5

Vanderwolf, C. H., Kolb, B., Cooley, R. K. (1978). Behavior of the rat after removal of the neocortex and hippocampal formation. *J Comp Physiol Psychol, 92*(1), 156–175. https://doi.org/10.1037/h0077447

Varela, C., Kumar, S., Yang, J. Y., Wilson, M. A. (2014). Anatomical substrates for direct interactions between hippocampus, medial prefrontal cortex, and the thalamic nucleus reuniens. *Brain Struct Funct, 219*(3), 911–929. https://doi.org/10.1007/s00429-013-0543-5

Vertes, R. P. (2002). Analysis of projections from the medial prefrontal cortex to the thalamus in the rat, with emphasis on nucleus reuniens. *J Comp Neurol 442*(2), 163–187. https://doi.org/10.1002/cne.10083

Vertes, R. P. (2004). Differential projections of the infralimbic and prelimbic cortex in the rat. *Synapse, 51*(1), 32–58. https://doi.org/10.1002/syn.10279

Vertes, R. P., Crane, A. M., Colom, L. V., Bland, B. H. (1995). Ascending projections of the posterior nucleus of the hypothalamus: PHAL analysis in the rat. *J Comp Neurol, 359*(1), 90–116. https://doi.org/10.1002/cne.903590107

Vertes, R. P., Hoover, W. B., Do Valle, A. C., Sherman, A., Rodriguez, J. J. (2006). Efferent projections of reuniens and rhomboid nuclei of the thalamus in the rat. *J Comp Neurol, 499*(5), 768–796. https://doi.org/10.1002/cne.21135

Vertes, R. P., Hoover, W. B. (2008). Projections of the paraventricular and paratenial nuclei of the dorsal midline thalamus in the rat. *J Comp Neurol, 508*(2), 212–237. https://doi.org/10.1002/cne.21679

Vertes, R. P., Hoover, W. B., Rodriguez, J. J. (2012). Projections of the central medial nucleus of the thalamus in the rat: Node in cortical, striatal and limbic forebrain circuitry.

Neuroscience, 219, 120–136. https://doi.org/10.1016/j.neuroscience.2012.04.067

Vogt, B. A., Peters, A. (1981). Form and distribution of neurons in the rat cingulate cortex: areas 32, 24, and 29. *J Comp Neurol 195*(4), 603–625. https://doi.org/10.1002/cne.901950406

Vogt, B. A., Miller, M. W. (1983). Cortical connections between rat cingulate cortex and visual, motor, and postsubicular cortices. *J Comp Neurol, 216*(2), 192–210. https://doi.org/10.1002/cne.902160207

Wagner, C. K., Eaton, M. J., Moore, K. E., Lookingland, K. J. (1995). Efferent projections from the region of the medial zona incerta containing A13 dopaminergic neurons: a PHA-L anterograde tract-tracing study in the rat. *Brain Res, 677*(2), 229–237. https://doi.org/10.1016/0006-8993(95)00128-d

Wang, C. C., Shyu, B. C. (2004). Differential projections from the mediodorsal and centrolateral thalamic nuclei to the frontal cortex in rats. *Brain Res, 995*(2), 226–235. https://doi.org/10.1016/j.brainres.2003.10.006

Wang, Q., Henry, A. M., Harris, J. A., Oh, S. W., Joines, K. M., Nyhus, J., Hirokawa, K. E., Dee, N., Mortrud, M., Parry, S., Ouellette, B., Caldejon, S., Bernard, A., Jones, A. R., Zeng, H., Hohmann, J. G. (2014). Systematic comparison of adeno-associated virus and biotinylated dextran amine reveals equivalent sensitivity between tracers and novel projection targets in the mouse brain. *J Comp Neurol 522*(9), 1989–2012. https://doi.org/10.1002/cne.23567

Watts, A. G., Kanoski, S. E., Sanchez-Watts, G., Langhans, W. (2022). The physiological control of eating: signals, neurons, and networks. *Physiol Rev, 102*(2), 689–813. https://doi.org/10.1152/physrev.00028.2020

Yoshida, A., Dostrovsky, J. O., Chiang, C. Y. (1992). The afferent and efferent connections of the nucleus submedius in the rat. *J Comp Neurol, 324*(1), 115–133. https://doi.org/10.1002/cne.903240109

Yoshida, K., McCormack, S., España, R. A., Crocker, A., Scammell, T. E. (2006). Afferents

to the orexin neurons of the rat brain. *J Comp Neurol, 494*(5), 845–861. https://doi.org/10.1002/cne.20859

Table 1. List of structures and abbreviations. Abbreviations and standard terms follow those of Swanson (2018). When available, the references at the ends of standard terms refer to the first use of the terms as defined. See Supplemental Bibliography for references.

Abbreviations	Standard terms for structures
AAA	*anterior amygdalar area (Gurdjian 1928)*
ACAd	*anterior cingulate area dorsal part (Krettek & Price, 1977a)*
ACB	*nucleus accumbens (Ziehen, 1897-1901)*
aco	*olfactory limb of the anterior commissure (>1840)*
act	*temporal limb of the anterior commissure (>1840)*
AD	*anterodorsal thalamic nucleus (>1840)*
ADP	*anterodorsal preoptic nucleus (Simerly et al., 1984)*
AHA	*anterior hypothalamic area (>1840)*
AHNa	*anterior hypothalamic area, anterior part (>1840)*
AHNc	*anterior hypothalamic area, central part (>1840)*
AHNd	*anterior hypothalamic area, dorsal part (>1840)*
AHNp	*anterior hypothalamic area, posterior part (>1840)*
AM	*anteromedial thalamic nucleus (>1840)*
AMd	*anteromedial thalamic nucleus dorsal part (Canteras & Swanson, 1992)*
AMv	*anteromedial thalamic nucleus ventral part (Canteras & Swanson, 1992)*
APN	*anterior pretectal nucleus (>1840)*
AQo	*opening of cerebral aqueduct (>1840)*
ARH	*arcuate hypothalamic nucleus (>1840)*
ATN	*anterior thalamic nuclei (>1840)*
AV	*anteroventral thalamic nucleus (>1840)*
AVP	*anteroventral preoptic nucleus (>1840)*
AVPV	*anteroventral periventricular nucleus (>1840)*
BA	*bed nucleus of accessory olfactory tract (Scalia & Witans, 1975)*
BAC	*bed nucleus of anterior commissure (Gurdjian, 1925)*
BSM	*bed nucleus of medullary stria (Risold & Swanson, 1995)*
BST	*bed nuclei of terminal stria (Gurdjian, 1925)*
BSTa	*bed nuclei of terminal stria anterior division (Ju & Swanson, 1989)*
BSTal	*bed nuclei of terminal stria anterolateral area (Swanson, 2004)*
BSTam	*bed nuclei of terminal stria anteromedial area (Dong & Swanson, 2006)*
BSTdm	*bed nuclei of terminal stria dorsomedial nucleus (Ju & Swanson, 1989)*
BSTfu	*bed nuclei of terminal stria fusiform nucleus (Ju & Swanson, 1989)*
BSTif	*bed nuclei of terminal stria interfascicular nucleus (Ju & Swanson, 1989)*
BSTju	*bed nuclei of terminal stria juxtacapsular nucleus (McDonald, 1983)*
BSTmg	*bed nuclei of terminal stria magnocellular nucleus (Ju & Swanson, 1989)*
BSTp	*bed nuclei of terminal stria posterior division (Ju & Swanson, 1989)*
BSTpr	*bed nuclei of terminal stria principal nucleus (Ju & Swanson, 1989)*
BSTrh	*bed nuclei of terminal stria rhomboid nucleus (Ju & Swanson, 1989)*

Abbreviations	Standard terms for structures
BSTse	*bed nuclei of terminal stria striatal extension (Ju & Swanson, 1989)*
BSTsz	*bed nuclei of terminal stria principal nucleus cell-sparse zone (Ju & Swanson, 1989)*
BSTtr	*bed nuclei of terminal stria transverse nucleus (Ju & Swanson, 1989)*
BSTv	*bed nuclei of terminal stria ventral nucleus (Ju & Swanson, 1989)*
CEAc	*central amygdalar nucleus capsular part (McDonald, 1982)*
CEAm	*central amygdalar nucleus medial part (McDonald, 1982)*
CL	*central lateral thalamic nucleus (Rioch, 1929)*
CM	*central medial thalamic nucleus (Rioch, 1929)*
CNG	*cingulate region (Brodmann, 1909)*
COAa	*cortical amygdalar area anterior part (>1840)*
COApm	*cortical amygdalar area posterior part medial zone (>1840)*
CP	*caudoputamen (Heimer & Wilson, 1975)*
cpd	*cerebral peduncle (Tarin, 1753)*
DMH	*dorsomedial hypothalamic nucleus (>1840)*
DMHa	*dorsomedial hypothalamic nucleus anterior part (>1840)*
DMHp	*dorsomedial hypothalamic nucleus posterior part (>1840)*
DMHv	*dorsomedial hypothalamic nucleus ventral part (>1840)*
ec	*external capsule (Burdach, 1822)*
em	*external medullary lamina (>1840)*
FF	*fields of Forel (>1840)*
frf	*radiation of corpus callosum frontal forceps (>1840)*
FS	*striatal fundus (>1840)*
GPl	*lateral globus pallidus (>1840)*
GPm	*medial globus pallidus (>1840)*
hbc	*habenular commissure (>1840)*
hitt	*thalamic habenulo-interpeduncular tract (Swanson, 2015)*
HYa	*hypothalamus anterior level (>1840)*
HYl	*lateral hypothalamic zone (Nauta & Haymaker, 1969)*
HYm	*medial hypothalamic zone (Nauta & Haymaker, 1969)*
HYp	*periventricular hypothalamic zone (Nauta & Haymaker, 1969)*
HYpr	*hypothalamic preoptic level (>1840)*
hys	*hypothalamic sulcus (>1840)*
I	*internuclear hypothalamic area (Swanson, 2004)*
IAD	*interanterodorsal thalamic nucleus (>1840)*
IAM	*interanteromedial thalamic nucleus (>1840)*
IB	*interbrain (Baer, 1837)*
ILA	*infralimbic area (Rose & Woolsey, 1948)*
ILM	*intralaminar thalamic nuclei (>1840)*
IMD	*intermediodorsal thalamic nucleus (>1840)*
im	*thalamic internal medullary lamina (>1840)*
int	*internal capsule (Burdach, 1822)*

Abbreviations	Standard terms for structures
IT	*interthalamic adhesion (>1840)*
LD	*lateral dorsal thalamic nucleus (>1840)*
LH	*lateral habenula (>1840)*
LHA	*lateral hypothalamic area (Nissl, 1913)*
LHAad	*lateral hypothalamic area anterior group anterior region dorsal zone (Swanson, 2004)*
LHAag	*lateral hypothalamic area anterior group (Swanson et al., 2005)*
LHAai	*lateral hypothalamic area anterior region anterior region intermediate zone (Swanson, 2004)*
LHAav	*lateral hypothalamic area anterior group anterior region ventral zone (Swanson, 2004)*
LHAd	*lateral hypothalamic area middle group lateral tier dorsal region (Swanson, 2004)*
LHAjd	*lateral hypothalamic area middle group medial tier juxtadorsomedial region (Swanson, 2004)*
LHAjp	*lateral hypothalamic area middle group medial tier juxtaparaventricular region (Swanson, 2004)*
LHAjv	*lateral hypothalamic area middle group medial tier juxtaventromedial region (Swanson, 2004)*
LHAjvd	*lateral hypothalamic area middle group medial tier juxtaventromedial region dorsal zone (Swanson, 2004)*
LHAjvv	*lateral hypothalamic area middle group medial tier juxtaventromedial region ventral zone (Swanson, 2004)*
LHAl	*lateral hypothalamic area middle group lateral tier (Swanson et al., 2005)*
LHAm	*lateral hypothalamic area middle group medial tier (Swanson et al., 2005)*
LHAma	*lateral hypothalamic area middle group lateral tier ventral region magnocellular nucleus (Paxinos & Watson, 1986)*
LHAmg	*lateral hypothalamic area middle group (Swanson et al., 2005)*
LHAp	*lateral hypothalamic area posterior group posterior region (Swanson, 2004)*
LHApc	*lateral hypothalamic area middle group lateral tier ventral region parvicellular region (Swanson, 2004)*
LHApf	*lateral hypothalamic area middle group perfironical tier (Swanson et al., 2005)*
LHApg	*lateral hypothalamic area posterior group (Swanson et al., 2005)*
LHAs	*lateral hypothalamic area middle group perifornical tier suprafornical region (Swanson, 2004)*
LHAsf	*lateral hypothalamic area middle group perifornical tier subfornical region (Swanson, 2004)*
LHAsfa	*lateral hypothalamic area middle group perifornical tier subfornical region anterior zone (Swanson, 2004)*
LHAsfp	*lateral hypothalamic area middle group perifornical tier subfornical region posterior zone (Swanson, 2004)*
LHAsfpm	*lateral hypothalamic area middle group perifornical tier subfornical region posterior zone premammillary subzone (Swanson, 2004)*
LHAv	*lateral hypothalamic area middle group lateral tier ventral region (Swanson et al., 2005)*

Abbreviations	Standard terms for structures
LHAvl	*lateral hypothalamic area middle group lateral tier ventral region lateral zone (Swanson, 2004)*
LHAvm	*lateral hypothalamic area middle group lateral tier ventral region medial zone (Swanson, 2004)*
LM	*lateral mammillary nucleus (Gudden, 1881)*
LP	*lateral posterior thalamic nucleus (>1840)*
LPO	*lateral preoptic area (>1840)*
LSr	*lateral septal nucleus rostral (rostroventral) part (Risold & Swanson, 1997)*
LSr.m.v.c	*lateral septal nucleus rostral (rostroventral) part medial zone ventral region caudal domain (Risold & Swanson, 1997)*
LSr.vl.v	*lateral septal nucleus rostral (rostroventral) part ventrolateral zone ventral region (Risold & Swanson, 1997)*
LSv	*lateral septal nucleus ventral part (Risold & Swanson, 1997)*
MA	*magnocellular nucleus (Swanson, 2004)*
mct	*medial corticohypothalamic tract (Gurdjian, 1927)*
MDc	*mediodorsal thalamic nucleus central part (>1840)*
MDl	*mediodorsal thalamic nucleus lateral part (>1840)*
MDm	*mediodorsal thalamic nucleus medial part (>1840)*
ME	*median eminence (Tilney, 1936)*
MEex	*median eminence external lamina (>1840)*
MEin	*median eminence internal lamina (>1840)*
MEAad	*medial amygdalar nucleus anterodorsal part (>1840)*
MEAav	*medial amygdalar nucleus anteroventral part (>1840)*
MEApv	*medial amygdalar nucleus posteroventral part (>1840)*
MEApd	*medial amygdalar nucleus posterodorsal part(>1840)*
MEPO	*median preoptic nucleus (Loo, 1931)*
mfb	*medial forebrain bundle (Edinger, 1893)*
mlt	*thalamic medial lemniscus (Swanson, 2015)*
MMme	*medial mammillary nucleus median part (>1840)*
MMpr	*medial mammillary nucleus principal part (Swanson, 2018)*
MOs	*secondary somatomotor areas (>1840)*
mph	*hypothalamic mammillary peduncle (Swanson, 2018)*
MPN	*medial preoptic nucleus (Gurdjian, 1927)*
MPNc	*medial preoptic nucleus central part (Simerly et al., 1984)*
MPNl	*medial preoptic nucleus lateral part (Simerly et al., 1984)*
MPNm	*medial preoptic nucleus medial part (Simerly et al., 1984)*
MPO	*medial preoptic area (>1840)*
MRNm	*midbrain reticular nucleus magnocellular part (Swanson, 2004)*
MS	*medial septal nucleus (>1984)*
mtgh	*hypothalamic mammillotegmental tract (Swanson, 2015)*
mtt	*mammillothalamic tract (Kölliker, 1896)*
mtth	*hypothalamic mammillothalamic tract (Swanson, 2018)*

Abbreviations	Standard terms for structures
mttt	*thalamic mammillothalamic tract (Swanson, 2015)*
NC	*nucleus circularis (>1840)*
NDB	*diagonal band nucleus (>1840)*
NId	*nucleus incertus diffuse part (Goto et al., 2001)*
NLOT	*nucleus of the lateral olfactory tract (Swanson & Petrovich, 1998)*
NPC	*nucleus of posterior commissure (>1840)*
och	*optic chiasm (Galen, c173)*
opth	*hypothalamic optic tract (Swanson, 2015)*
optt	*thalamic optic tract (Swanson, 2015)*
ORBv	*ventral orbital area (Krettek & Price, 1977)*
OT	*olfactory tubercle (Calleja, 1893)*
OV	*vascular organ of lamina terminalis (>1840)*
PA	*posterior amygdalar nucleus (Canteras et al., 1992)*
PAG	*periaqueductal gray (>1840)*
PAGdl	*periaqueductal gray dorsolateral column (Carrive et al., 1997)*
PAGm	*periaqueductal gray medial division (Beitz, 1985)*
PAGrl	*periaqueductal gray rostrolateral division (Swanson, 1998)*
PAGrm	*periaqueductal gray rostromedial division (Swanson, 1998)*
PAGvl	*periaqueductal gray ventrolateral column (Carrive et al., 1997)*
PCN	*paracentral thalamic nucleus (Gurdjian, 1927)*
PD	*posterodorsal preoptic nucleus (Simerly et al., 1984)*
PF	*parafascicular nucleus (Vogt, 1909)*
PH	*posterior hypothalamic nucleus (>1840)*
PL	*prelimbic area (Brodmann, 1909)*
pm	*principal mammillary tract (Kölliker, 1896)*
PMd	*dorsal mammillary nucleus (>1840)*
PMv	*ventral premammillary nucleus (>1840)*
PO	*posterior thalamic complex (>1840)*
pofs	*septal postcommissural fornix (Swanson, 2015)*
pofh	*hypothalamic postcommissural fornix (Swanson, 2015)*
PR	*perireuniens nucleus (Brittain, 1988)*
PRC	*periaqueductal gray precommissural nucleus (Paxinos & Watson, 1986)*
PS	*parastriatal nucleus (Simerly et al., 1984)*
PSCH	*suprachiasmatic preoptic nucleus (Simerly et al., 1984)*
PST	*preparasubthalamic nucleus (Swanson, 2004)*
PSTN	*parasubthalamic nucleus (Wang & Zhang, 1995)*
PT	*paratenial nucleus (>1840)*
PVa	*periventricular hypothalamic nucleus anterior part (Swanson, 2018)*
PVaa	*periventricular hypothalamic nucleus anterior part anterior zone (Swanson, 2018)*
PVH	*paraventricular hypothalamic nucleus (>1840)*

Abbreviations	Standard terms for structures
PVHam	*paraventricular hypothalamic nucleus magnocellular division anterior magnocellular part (Swanson & Kuypers, 1980)*
PVHap	*paraventricular hypothalamic nucleus parvicellular division anterior parvicellular part (>1840)*
PVHdp	*paraventricular hypothalamic nucleus descending division dorsal parvicellular part (>1840)*
PVHf	*paraventricular hypothalamic nucleus descending division forniceal part (>1840)*
PVHlp	*paraventricular hypothalamic nucleus descending division lateral parvicellular part (>1840)*
PVHmpd	*paraventricular hypothalamic nucleus parvicellular division medial parvicellular part dorsal zone (Swanson & Simmons, 2008)*
PVHmpdl	*paraventricular hypothalamic nucleus parvicellular medial parvicellular part dorsal zone lateral wing (Swanson & Simmons, 2008)*
PVHmpv	*paraventricular hypothalamic nucleus descending division medial parvicellular part ventral zone (>1840)*
PVHpml	*paraventricular hypothalamic nucleus magnocellular division posterior magnocellular part lateral zone (>1840)*
PVHpmm	*paraventricular hypothalamic nucleus magnocellular division posterior magnocellular part medial zone (>1840)*
PVHpv	*paraventricular hypothalamic nucleus parvicellular division periventricular part (>1840)*
PVi	*paraventricular hypothalamic nucleus anterior part intermediate zone (Swanson, 2018)*
PVp	*periventricular hypothalamic nucleus posterior part (>1840)*
PVpo	*periventricular hypothalamic nucleus anterior part preoptic zone (Swanson, 2018)*
PVT	*paraventricular thalamic nucleus (>1840)*
RCH	*lateral hypothalamic area anterior group retrochiasmatic area (>1840)*
REcd	*nucleus reuniens caudal division dorsal part (Risold et al., 1997)*
REcm	*nucleus reuniens caudal division median part (Risold et al., 1997)*
REcp	*nucleus reuniens caudal division posterior part (Risold et al., 1997)*
REr	*nucleus reuniens rostral division (Risold et al., 1997)*
REra	*nucleus reuniens rostral division anterior part (Risold et al., 1997)*
RErd	*nucleus reuniens rostral division dorsal part (Risold et al., 1997)*
RErl	*nucleus reuniens rostral division lateral part (Risold et al., 1997)*
RErm	*nucleus reuniens rostral division median part (Risold et al., 1997)*
RErv	*nucleus reuniens rostral division ventral part (Risold et al., 1997)*
RH	*rhomboid nucleus (Cajal, 1904)*
ri	*rhinal incisure (>1840)*
RT	*reticular thalamic nucleus (>1840)*
SBPV	*subparaventricular zone (Watts et al., 1987)*
SCH	*suprachiasmatic nucleus (Spiegel & Zwieg, 1919)*
SCO	*subcommissural organ (>1840)*
SEZ	*subependymal zone (>1840)*

Abbreviations	Standard terms for structures
SF	*septofimbrial nucleus (>1840)*
SI	*innominate substance (Schwalbe, 1881)*
sm	*medullary stria (Wenzel & Wenzel, 1812)*
sme	*epithalamic medullary stria (Swanson, 2015)*
smd	*supramammillary decussation (>1840)*
smh	*hypothalamic medullary stria (Swanson, 2015)*
SMT	*submedial thalamic nucleus (>1840)*
SNr	*substantia nigra reticular part (Sano, 1910)*
SO	*supraoptic nucleus (Lenhossék, 1887)*
SOp	*supraoptic nucleus principal part (Swanson, 2018)*
SOr	*supraoptic nucleus retrochiasmatic part (>1840)*
SPFm	*subparafascicular nucleus magnocellular part (>1840)*
SPFpl	*subparafascicular nucleus parvicellular part lateral division (>1840)*
SPFpm	*subparafascicular nucleus parvicellular part medial division (>1840)*
st	*terminal stria (Wenzel & Wenzel, 1812)*
ste	*endbrain terminal stria (Swanson, 2015)*
STN	*subthalamic nucleus (>1840)*
SUM	*supramammillary nucleus (>1840)*
SUMl	*supramammillary nucleus lateral part (Swanson, 1982)*
SUMm	*supramammillary nucleus medial part (Swanson, 1982)*
sup	*supraoptic decussations (>1840)*
suph	*hypothalamic supraoptic decussations (Swanson, 2018)*
TEP	*temporal pole (Broca, 1878)*
THe	*epithalamus (His, 1893)*
THv	*ventral part of thalamus (Herrick, 1910)*
TMd	*tuberomammillary nucleus dorsal part (Köhler et al., 1985)*
TMv	*tuberomammillary nucleus ventral part (Köhler et al., 1985)*
TRS	*triangular septal nucleus (>1840)*
TTd	*tenia tecta dorsal part (Swanson, 1992)*
TTv	*tenia tecta ventral part (Swanson, 1992)*
TU	*lateral hypothalamic area middle group lateral tier tuberal nucleus (>1840)*
TUi	*lateral hypothalamic area middle group lateral tier tuberal nucleus intermediate part (Swanson, 2004)*
TUl	*lateral hypothalamic area middle group lateral tier tuberal nucleus lateral part (Swanson, 2004)*
TUsv	*lateral hypothalamic area middle group lateral tier tuberal nucleus subventromedial part (Swanson, 2004)*
TUte	*lateral hypothalamic area middle group lateral tier tuberal nucleus terete part (Petrovich et al., 2001)*
V3h	*hypothalamic part of third ventricle principal part (Swanson, 2018)*
V3i	*third ventricle infundibular recess (>1840)*
V3m	*third ventricle mammillary recess (>1840)*

Abbreviations	Standard terms for structures
V3p	*third ventricle preoptic recess (>1840)*
V3r	*roof of third ventricle (>1840)*
V3t	*thalamic part of third ventricle principal part (Swanson, 2018)*
VAL	*ventral anterior-lateral thalamic complex (>1840)*
VENT	*ventral thalamic nuclei (>1840)*
VLP	*ventrolateral preoptic nucleus (Sherin et al., 1998)*
vlt	*ventrolateral hypothalamic tract (Swanson, 2004)*
VM	*ventral medial thalamic nucleus (>1840)*
VMHa	*ventromedial hypothalamic nucleus anterior part (>1840)*
VMHc	*ventromedial hypothalamic nucleus central part (>1840)*
VMHdm	*ventromedial hypothalamic nucleus dorsomedial part (>1840)*
VMHvl	*ventromedial hypothalamic nucleus ventrolateral part (>1840)*
VPLpc	*ventral posterolateral thalamic nucleus parvicellular part (>1840)*
VPLpr	*ventral posterolateral thalamic nucleus principal part (Swanson, 2004)*
VPMpc	*ventral posteromedial thalamic nucleus parvicellular part (>1840)*
VPMpr	*ventral posteromedial thalamic nucleus principal part (Swanson, 2004)*
VTA	*ventral tegmental area (Tsai, 1925)*
ZI	*zona incerta (>1840)*
ZIda	*zona incerta dopaminergic group (>1840)*

Table 2. List of antibodies and reagents

Reagent	Antigen/ Conjugate	Host	Type	Source	Catalog #	RRID	Titer
Primary	anti-PHAL	Rb	polyclonal IgG	Vector Labs	AS-2300	AB_2313686	1:4,000
	anti-CTB	Gt	polyclonal IgG	List Biological	703	AB_10013220	1:10,000
Secondary	anti-rabbit IgG	Dk	biotinylated	Jackson	711-065-152	AB_2340593	1:500
	anti-goat IgG	Dk	biotinylated	Jackson	705-065-147	AB_2340397	1:500
	anti-rabbit IgG	Dk	Cy5-conjugated	Jackson	711-175-152	AB_2340607	1:500
	anti-goat IgG	Dk	Cy3-conjugated	Jackson	705-165-147	AB_2307351	1:500
Conjugate	avidin	-	HRP-conjugated (ABC Kit)	Vector Labs	PK-6100	n/a	n/a

Table 3. Semi-quantitative analysis of mPFC connectional weights with diencephalon by region. Both PHAL and CTB connectional strengths were tabulated in a 0–5 scale. A "-" is used to indicate an absence of connectivity, "+" and "++" indicate low, "+++" indicates moderate, and "++++" and "+++++" indicate high connectional strength. Diencephalic regions on the left column are named and ordered according to Swanson (2018). Semi-quantification was only done on gray matter regions labeled on the atlas and higher-order groupings were left with a blue fill. See Methods section for details regarding score determination.

	ILA (#113)		ACAd (#131)	
Diencephalic cell groups or regions	**PHA-L**	**CTB**	**PHA-L**	**CTB**
Hypothalamus (HY)				
Periventricular hypothalamic zone (HYp)				
Terminal lamina (lam)				
Vascular organ of lamina terminalis (OV)	–	–	–	–
Median preoptic nucleus (MEPO)	+	–	–	–
Subfornical organ (SFO)	–	–	–	–
Anteroventral periventricular nucleus (AVPV)	+	–	–	–
Suprachiasmatic preoptic nucleus (PSCH)	–	–	–	–
Periventricular hypothalamic nucleus anterior part (PVa)				
preoptic zone (PVpo)	–	–	–	–
anterior zone (PVaa)	–	–	–	–
intermediate zone (PVi)	–	–	–	+
Internuclear hypothalamic area (I)	+	++	–	–
Anteroventral preoptic nucleus (AVP)	+	+	+	–
Anterodorsal preoptic nucleus (ADP)	+	–	–	–
Medial preoptic area (MPO)	++	+	+	+
Parastriatal nucleus (PS)	+	–	–	–
Posterodorsal preoptic nucleus (PD)	–	–	–	–
Ventrolateral preoptic nucleus (VLP)				
Suprachiasmatic nucleus (SCH)	–	–	–	–
Subparaventricular zone (SBPV)	+	–	–	–
Paraventricular hypothalamic nucleus (PVH)				
Parvicellular division (PVHp)				
Periventricular part (PVHpv)	+	+	–	–
Anterior parvicellular part (PVHap)	–	–	–	–
Medial parvicellular part dorsal zone (PVHmpd)	+	–	–	–
lateral wing (PVHmpdl)	–	–	–	–
Magnocellular division (PVHm)				
Anterior magnocellular part (PVHam)	++	–	–	–
Posterior magnocellular part (PVHpm)				
medial zone (PVHpmm)	+	–	–	–
lateral zone (PVHpml)	+	–	–	–
Descending division (PVHd)				

Diencephalic cell groups or regions	ILA (#113)		ACAd (#131)	
	PHA-L	CTB	PHA-L	CTB
medial parvicellular part ventral zone (PVHmpv)	+	–	–	–
dorsal parvicellular part ventral zone (PVHdp)	+	–	–	–
lateral parvicellular part ventral zone (PVHlp)	+	–	–	–
forniceal part (PVHf)	–	–	–	–
Anterior hypothalamic area (AHA)	+	–	–	–
Supraoptic nucleus (SO)				
principal part (SOp)	–	–	–	–
retrochiasmatic part (SOr)	–	–	–	–
Arcuate hypothalamic nucleus (ARH)	–	+	–	–
Dorsomedial hypothalamic nucleus (DMH)				
Anterior part (DMHa)	++	–	–	–
Posterior part (DMHp)	+	+	–	–
Ventral part (DMHv)	+	++	–	–
Periventricular hypothalamic nucleus posterior part (PVp)	–	+	–	–
Posterior hypothalamic nucleus (PH)	+++	+++	+++	+
Medial hypothalamic zone (HYm)				
Medial preoptic nucleus (MPN)				
Medial part (MPNm)	+	–	–	–
Central part (MPNc)	–	–	–	–
Lateral part (MPNl)	+	–	–	–
Anterior hypothalamic nucleus (AHN)				
Anterior part (AHNa)	+	–	–	–
Central part (AHNc)	+	–	+	–
nucleus circularis (NC)	–	–	–	–
Posterior part (AHNp)	+	–	–	–
Dorsal part (AHNd)	+	–	–	–
Ventromedial hypothalamic nucleus (VMH)				
Anterior part (VMHa)	–	++	–	–
Ventrolateral part (VMHvl)	–	+	–	+
Central part (VMHc)	–	–	–	–
Dorsomedial part (VMHdm)	+	+	–	–
Ventral premammillary nucleus (PMv)	+	–	–	–
Dorsal premammillary nucleus (PMd)	+	–	++	–
Mammillary body (MBO)				
Tuberomammillary nucleus (TM)				
ventral part (TMv)	–	–	–	–
dorsal part (TMd)	–	–	–	–
Medial mammillary nucleus (MM)				
principal part (MMpr)	–	–	–	–
median part (MMme)	+++++	–	–	–
Lateral mammillary nucleus (LM)	–	–	–	–

Diencephalic cell groups or regions	ILA (#113)		ACAd (#131)	
	PHA-L	CTB	PHA-L	CTB
Supramammillary nucleus (SUM)				
Medial part (SUMm)	+	–	–	–
Lateral part (SUMl)	++	+	+	–
Lateral hypothalamic zone (HYl)				
Lateral preoptic area (LPO)	++	+++	++	++
Lateral hypothalamic area (LHA)				
Anterior group (LHAag)				
Retrochiasmatic area (RCH)	+	–	–	–
Anterior region (LHAa)				
ventral zone (LHAav)	+++	++++	+	+
intermediate zone (LHAai)	+++	+	–	–
dorsal zone (LHAad)	++	–	++	–
Middle group (LHAmg)				
Medial tier (LHAm)				
Juxtaventromedial region (LHAjv)				
Ventral zone (LHAjvv)	++	+++	–	+
Dorsal zone (LHAjvd)	++	+	–	–
Juxtaparaventricular region (LHAjp)	+	+	++	–
Juxtadorsomedial region (LHAjd)	+++	++	+	–
Perifornical tier (LHApf)				
Subfornical region (LHAsf)				
Anterior zone (LHAsfa)	++	+	–	–
Posterior zone (LHAsfp)	++	+	–	–
premammillary subzone (LHAsfpm)	+	–	–	–
Suprafornical region (LHAs)	+++++	++	+	+
Lateral tier (LHAl)				
Tuberal nucleus (TU)				
subventromedial part (TUsv)	+	+	–	–
intermediate part (TUi)	++	+	–	–
terete part (TUte)	+++++	++	–	–
lateral part (TUl)	+	–	–	–
Ventral region (LHAv)				
medial zone (LHAvm)	++	+	–	–
lateral zone (LHAvl)	++++	+	–	–
parvicellular region (LHApc)	–	–	–	–
magnocellular nucleus (LHAma)	++	+	–	–
Dorsal region (LHAd)	+++++	++	+	–
Posterior group (LHApg)				
Posterior region (LHAp)	++++	+++	++	–
Preparasubthalamic nucleus (PST)	+	–	–	–
Parasubthalamic nucleus (PSTN)	+++++	+	–	–

Diencephalic cell groups or regions	ILA (#113)		ACAd (#131)	
	PHA-L	CTB	PHA-L	CTB
Subthalamic nucleus (STN)	–	–	++	–
Thalamus (TH)				
Ventral part of thalamus (THv)				
Zona incerta general (ZIg)				
Zona incerta (ZI)	+	++	++	+
dopaminergic group (ZIda)	–	–	+	–
Fields of Forel (FF)	–	–	–	–
Ventral lateral geniculate nucleus (LGv)				
medial zone (LGvm)	–	–	–	–
lateral zone (LGvl)	–	–	–	–
Intergeniculate leaflet (IGL)	–	–	–	–
Reticular thalamic nucleus (RT)	–	–	–	–
Dorsal part of thalamus (THd)				
Midline thalamic nuclei (MTN)				
Nucleus reuniens (RE)				
Rostral division (REr)				
anterior part (REra)	+++	+++++	+	–
dorsal part (RErd)	++	++++	++	++++
ventral part (RErv)	++++	++++	+	–
lateral part (RErl)	++++	++++	++	++++
median part (RErm)	++	++++	++	–
Caudal division (REc)				
posterior part (REcp)	++++	+++	++	+
dorsal part (REcd)	+++++	+++++	+++	+
median part (REcm)	++++	++	+	–
Paraventricular thalamic nucleus (PVT)	+++	+++++	+	–
Paratenial nucleus (PT)	+++	+++++	+++	++
Anterior thalamic nuclei (ATN)				
Anteroventral thalamic nucleus (AV)	–	–	+	–
Anterodorsal thalamic nucleus (AD)	–	–	+	–
Anteromedial thalamic nucleus (AM)				
Ventral part (AMv)	+	+++	++++	+++++
Dorsal part (AMd)	+	++	+++++	++++
Interanteromedial thalamic nucleus (IAM)	+	++	++++	++++
Interanterodorsal thalamic nucleus (IAD)	+	+	+++	++
Lateral dorsal thalamic nucleus (LD)	–	–	+	–
Medial thalamic nuclei (MED)				
Perireuniens nucleus (PR)	++++	++++	+++++	+++
Submedial thalamic nucleus (SMT)	++++	+	++	–
Mediodorsal thalamic nucleus (MD)				
Medial part (MDm)	+++++	+++++	+	++

Diencephalic cell groups or regions	ILA (#113)		ACAd (#131)	
	PHA-L	CTB	PHA-L	CTB
Central part (MDc)	+	+++	+	+
Lateral part (MDl)	+	+++	+++++	+++++
Intermediodorsal thalamic nucleus (IMD)	+++	+++	+	–
Intralaminar thalamic nuclei (ILM)				
Rhomboid nucleus (RH)	+	++++	+	+
Central medial thalamic nucleus (CM)	+	++++	+++++	+++++
Paracentral thalamic nucleus (PCN)	–	–	–	–
Central lateral thalamic nucleus (CL)	–	–	+++	++++
Parafascicular nucleus (PF)	+	+++	+	–
Ventral thalamic nuclei (VENT)				
Ventral anterior-lateral thalamic complex (VAL)	–	–	+	++
Ventral medial thalamic nucleus (VM)	+	++	+++++	++++
Ventral posterior thalamic nucleus (VP)				
Ventral posteromedial thalamic nucleus (VPM)				
Principal part (VPMpr)	–	–	–	–
Parvicellular part (VPMpc)	–	+	–	–
Ventral posterolateral thalamic nucleus (VPL)				
Principal part (VPLpr)	–	–	–	–
Parvicellular part (VPLpc)	–	–	–	–
Subparafascicular nucleus (SPF)				
Magnocellular part (SPFm)	+	–	+	–
Parvicellular part (SPFp)				
medial division (SPFpm)	–	–	–	–
lateral division (SPFpl)	–	–	–	–
Peripeduncular nucleus (PP)	–	–	–	–
Lateral thalamic nuclei (LAT)				
Lateral posterior thalamic nucleus (LP)	–	–	+	+
Posterior thalamic nuclei (POT)				
Posterior thalamic complex (PO)	–	–	–	–
Suprageniculate nucleus (SGN)	–	–	–	–
Posterior limiting thalamic nucleus (POL)	–	–	–	–
Dorsal lateral geniculate nucleus (LGd)	–	–	–	–
Medial geniculate complex (MG)				
Medial part (MGm)	–	–	–	–
Ventral part (MGv)	–	–	–	–
Dorsal part (MGd)	–	–	–	–
Epithalamus (THe)				
Habenular nuclei (H)				
Medial habenula (MH)	–	–	–	–
Lateral habenula (LH)	+	–	+	+

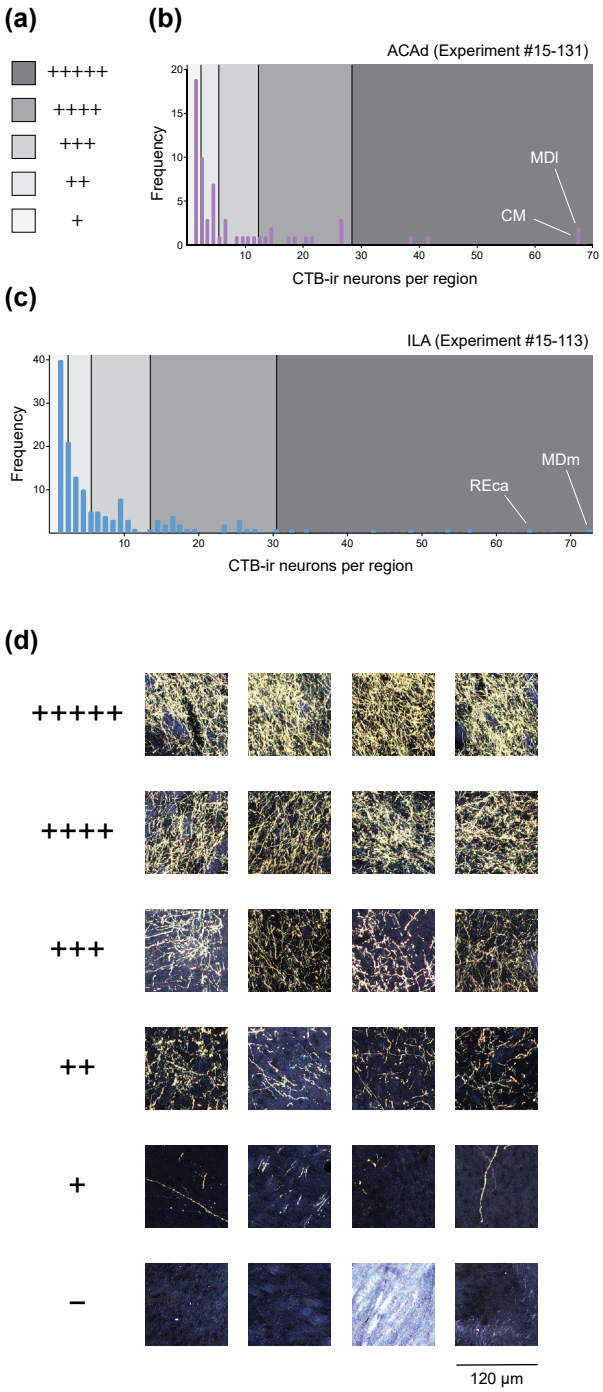

Supplemental Figure 1. Strategies for obtaining semi-quantitative scores (0–5 scale) for CTB (**a**–**c**) and PHAL (**d**). (**a**) Shading code corresponding to symbols used in **Table 3**. (**b**, **c**) Histograms showing frequency of CTB-ir neuron counts per region across each atlas level for CTB injections in the ACAd (**b**) and ILA (**c**). Shaded zones follow numerical ranges for scores in (a). (**d**) Representative darkfield photomicrographs showing examples for each axon density score. Images were sampled using 120 × 120 µm bins.

Supplemental Bibliography

Beitz, A.J. (1985). The midbrain periaqueductal gray in the rat. I. Nuclear volume, cell number, density, orientation, and regional subdivisions. *J Comp Neurol, 237*(4), 445–459. https://doi.org/10.1002/cne.902370403

Brittain, D.A. (1988). *The Efferent Connections of the Infralimbic Area in the Rat*. Ph.D. Thesis. LaJolla, University of California at San Diego, pp. 1–170.

Broca, P.P. (1878). Nomenclature cérébrale: dénomination et subdivision des hémisphères et des anfractuosités de la surface. *Revue d'Anthropologie, 1*, 193–236.

Brodmann, K. (1909). *Vergleichende Lokalisationslehre der Grosshirnrinde in ihren Prinzipien Dargestellt auf Grund des Zellenbaues* (Barth, Leipzig).

Burdach, K.F. (1819, 1822, 1826). *Vom Baue und Leben des Gehirns* (Dyk'schen Buchhandlung, Leipzig).

Cajal, S.R. y (1899-1904). *Textura del Sistema Nervioso del Hombre y de los Vertebrados: Estudios sobre el Plan Estructural y Composición de los Centros Serviosos Adicionados de Consideraciones Fisiológicas Fundadas en los Nuevos Descubrimientos*, 2 Vols. (Moya, Madrid).

Calleja, C. (1893). *La Región Olfatoria del Cerebro* (Moya, Madrid).

Canteras, N.S., Simerly, R.B., & Swanson, L.W. (1992). The connections of the posterior nucleus of the amygdala. *J Comp Neurol, 324*(2), 143–179. https://doi.org/10.1002/cne.903240203

Canteras, N.S. & Swanson, L.W. (1992). The dorsal premammillary nucleus: an unusual component of the mammillary body. *Proc Natl Acad Sci U S A, 89*(21), 10089–10093. https://doi.org/10.1073/pnas.89.21.10089

Carrive, P., Leung, P., Harris, J., & Paxinos, G. (1997). Conditioned fear to context is associated with increased Fos expression in the caudal ventrolateral region of the midbrain periaqueductal gray. *Neuroscience, 78*(1), 165–177. https://doi.org/10.1016/s0306-4522(97)83047-3

Dong, H.-W. & Swanson, L.W. (2006). Projections from bed nuclei of the stria terminalis, anteromedial area: cerebral hemisphere integration of neuroendocrine, autonomic, and behavioral aspects of energy balance. *J Comp Neurol, 494*(1), 142–178. https://doi.org/10.1002/cne.20788

Edinger, L. (1893). *Vorlesungen über den Bau der nervösen Centralorgane des Menschen und der Thiere* (Vogel, Leipzig).

Galen, C. (c173). *On the Usefulness of the Parts of the Body*. Translated from the Greek with an Introduction and Commentary by M.T. May (Cornell University Press, Ithaca), 1968.

Gudden, B. von (1881). Beitrag zur Kentnis des Corpus mammillare und der sogenannten Schenkel des Fornix. *Archiv für Psychiatrie und Nervenkrankheiten 11*:428–452.

Gurdjian, E.S. (1925). Olfactory connections in the albino rat, with special reference to the stria medullaris and the anterior commissure. *J Comp Neurol, 38*, 127–163.

Gurdjian, E.S. (1927). The diencephalon of the albino rat. *J Comp Neurol, 43*, 1–114.

Gurdjian, E.S. (1928). The corpus striatum of the rat. *J Comp Neurol, 45*, 249–281.

Heimer, L. & Wilson, R.D. (1975). The subcortical projections of the allocortex: similarities in the neural associations of the hippocampus, the piriform cortex, and the neocortex. In: Santini, M. (Ed.) *Golgi Centennial Symposium Proceedings* (Raven Press, New York), pp. 177–193.

Herrick, C.J. (1910). The morphology of the forebrain in amphibia and reptilia. *J Comp Neurol Psychol, 20*, 413–547. https://doi.org/10.1002/cne.920200502

His, W. (1893). Vorschläge zur Eintheilung des Gehrins. *Archiv für Anatomie und Entwickelungsgeschichte* [no volume indicated] pp. 172–179.

Ju, G. & Swanson, L.W. (1989). Studies on the cellular architecture of the bed nuclei of the stria terminalis in the rat: I. Cytoarchitecture. *J Comp Neurol, 280*(4), 587–602. https://doi.org/10.1002/cne.902800409

Köhler, C., Swanson, L.W., Haglund, L., & Wu, Y.-Y. (1985). The cytoarchitecture,

histochemistry and projections of the tuberomammillary nucleus in the rat. *Neuroscience, 16*(1), 85–110. https://doi.org/10.1016/0306-4522(85)90049-1

Kölliker, A. (1896). Handbuch der Gewebelehre des Menschen, 6th Edn., Zweiter Band: *Nervensystem des Menschen und der Thiere* (Engelmann, Leipzig).

Krettek, J.E. & Price, J.L. (1977). The cortical projections of the mediodorsal nucleus and adjacent thalamic nuclei in the rat. *J Comp Neurol, 171*(2), 157–192. https://doi.org/10.1002/cne.901710204

Lenhossék, M. (1887). Beobachtungen am Gehirn des Menschen. *Anatomischer Anzeiger, 2*, 450–461.

Loo, Y.T. (1931). The forebrain of the opossum, Didelphis virginiana. *J Comp Neurol, 52*(1), 1–148. https://doi.org/10.1002/cne.900520102

Nauta, W.J.H. & Haymaker, W. (1969). Hypothalamic nuclei and fiber connections. In: Haymaker, W., Anderson, E., & Nauta, W.J.H. (Eds.) *The Hypothalamus* (Chas. C Thomas, Springfield IL), pp. 136–209.

McDonald, A.J. (1982). Cytoarchitecture of the central amygdaloid nucleus of the rat. *J Comp Neurol, 208*(4), 401-418. https://doi.org/10.1002/cne.902080409

McDonald, A. J. (1983). Neurons of the bed nucleus of the stria terminalis: a golgi study in the rat. *Brain Res Bull, 10*(1), 111–120. https://doi.org/10.1016/0361-9230(83)90082-5

Nissl, F. (1913). Die Grosshirnanteile des Kaninchens. *Archiv für Psychiatrie und Nervenkrankheiten, 52*, 867–953.

Paxinos, G. & Watson, C. (1986). *The Rat Brain in Stereotaxic Coordinates*, 2nd Edn. (Academic Press, New York).

Petrovich, G.D., Canteras, N.S., & Swanson L.W. (2001). Combinatorial amygdalar inputs to hippocampal domains and hypothalamic behavior circuits. *Brain Res Rev, 38*(1–2), 247–289. https://doi.org/10.1016/s0165-0173(01)00080-7

Rioch, D.M. (1929). Studies on the diencephalon of Carnivora. Part II: Certain nuclear

configurations and fiber connections of the subthalamus and midbrain of the dog and cat. *J Comp Neurol, 49*, 121–153.

Risold, P.Y. & Swanson, L.W. (1995). Cajal's nucleus of the stria medullaris: characterization by in situ hybridization and immunohistochemistry for enkephalin. *J Chem Neuroanat, 9*(4), 235–240. https://doi.org/10.1016/0891-0618(95)00083-6

Risold, P.Y. & Swanson, L.W. (1997). Chemoarchitecture of the rat lateral septal nucleus. *Brain Res Rev, 24*(2–3), 91–113. https://doi.org/10.1016/s0165-0173(97)00008-8

Risold, P.Y., Thompson, R.H., & Swanson, L.W. (1997). The structural organization of connections between hypothalamus and cerebral cortex. *Brain Res Rev, 24*(2–3), 197–254. https://doi.org/10.1016/s0165-0173(97)00007-6

Rose, J.E. & Woolsey, C.N. (1948). Structure and relations of limbic cortex and anterior thalamic nuclei in rabbit and cat. *J Comp Neurol, 89*(3), 279–347. https://doi.org/10.1002/cne.900890307

Sano, T. (1910). Beitrag zur vergleichenden Anatomie der Substantia nigra, des Corps Luysii und der Zona incerta. *Monatsschrift für Psychiatrie und Neurologie, 28*, 26–31.

Scalia, F. & Winans, S.S. (1975). The differential projections of the olfactory bulb and accessory olfactory bulb in mammals. *J Comp Neurol, 161*(2), 31–56. https://doi.org/10.1002/cne.901610105

Schwalbe, G. (1881). *Lehrbuch der Neurology* (Besold, Erlangen).

Sherin, J.E., Elmquist, J.K., Torrealba, F., & Saper, C.B. (1998). Innervation of histaminergic tuberomammillary neurons by GABAergic and galaninergic neurons in the ventrolateral preoptic nucleus of the rat. *J Neurosci, 18*(12), 4705–4721. https://doi.org/10.1523/jneurosci.18-12-04705.1998

Simerly, R.B., Swanson, L.W., & Gorski, R.A. (1984). Demonstration of a sexual dimorphism in the distribution of serotonin-immunoreactive fibers in the medial preoptic nucleus of the rat. *J Comp Neurol, 225*(2), 151–166. https://doi.org/10.1002/cne.902250202

Simmons, D.M. & Swanson, L.W. (2008). High resolution paraventricular nucleus serial section model constructed within a traditional rat brain atlas. *Neurosci Lett, 438*(1), 85–89. https://doi.org/10.1016/j.neulet.2008.04.057

Spiegel, E.A. & Zwieg, H. (1919). Zur Cytoarchitektonic des Tuber cinereum. *Arbeiten aus dem Neurologischen Institute an der Wiener Universiteit, 22*, 278–295.

Swanson, L.W. (1982). The projections of the ventral tegmental area and adjacent regions: a combined fluorescent retrograde tracer and immunofluorescence study in the rat. *Brain Res Bull, 9*(1–6), 321–353. https://doi.org/10.1016/0361-9230(82)90145-9

Swanson, L.W. (1992). *Brain Maps: Structure of the Rat Brain* (Elsevier, Amsterdam).

Swanson, L.W. (1998). *Brain Maps: Structure of the Rat Brain. A Laboratory Guide with Printed and Electronic Templates for Data, Models and Schematics*, 2nd Edn. with 2 CD-ROMs (Elsevier, Amsterdam).

Swanson, L.W. (2004). *Brain Maps: Structure of the Rat Brain. A Laboratory Guide with Printed and Electronic Templates for Data, Models and Schematics*, 3rd Edn. (Elsevier, Amsterdam), 215 pp. with CD-ROM, Brain Maps: Computer Graphics Files 3.0.

Swanson, L.W. (2015). *Neuroanatomical Terminology: A Lexicon of Classical Origins and Historical Foundations* (Oxford University Press, New York).

Swanson L.W. (2018). Brain Maps 4.0—Structure of the Rat Brain: an open access atlas with global nervous system nomenclature ontology and flatmaps. *J Comp Neurol, 526*(6), 935–943. https://doi.org/10.1002/cne.24381

Swanson, L.W. & Kuypers, H.G.J.M. (1980). A direct projection from the ventromedial nucleus and retrochiasmatic area of the hypothalamus to the medulla and spinal cord of the rat. *Neurosci Lett, 17*(3), 307–312. https://doi.org/10.1016/0304-3940(80)90041-5

Swanson, L.W. & Simmons, D.M. (1989). Differential steroid hormone and neural influences on peptide mRNA levels in CRH cells of the paraventricular nucleus:

a hybridization histochemical study in the rat. *J Comp Neurol, 285*(4), 413–435. https://doi.org/10.1002/cne.902850402

Swanson, L.W., Sanchez-Watts, G., & Watts, A.G. (2005). Comparison of melanin-concentrating hormone and hypocretin/orexin mRNA expression patterns in a new parceling scheme of the lateral hypothalamic zone. *Neurosci Lett, 387*(2), 80–84. https://doi.org/10.1016/j.neulet.2005.06.066

Swanson, L.W. & Petrovich, G.D. (1998). What is the amygdala? *Trends Neurosci, 21*(8), 323–331. https://doi.org/10.1016/s0166-2236(98)01265-x

Tarin, P. (1753). *Dictionnaire Anatomique suivi d'une Bibliotheque Anatomique et Physiologique* (Briasson, Paris).

Tilney, F. (1936). The development and constituents of the human hypophysis. *Bulletin of the Neurological Institute of New York, 5*, 387–436.

Tsai, C. (1925). The optic tracts and centers of the opossum, Didelphis virginiana. *J Comp Neurol, 39*(2), 173–216. https://doi.org/10.1002/cne.900390202

Vogt, C. (1909) La myéloarchitecture du thalamus du cercopithèque. *Journal für Psychologie und Neurologie 12* (Suppl.), 285–324.

Wang, P.Y. & Zhang, F.C. (1995). *Outlines and Atlas of Learning Rat Brain Slices* (Westnorth University Press, China).

Watts, A.G., Swanson, L.W, & Sanchez-Watts, G. (1987). Efferent projections of the suprachiasmatic nucleus: I. Studies using anterograde transport of *Phaseolus vulgaris* leucoagglutinin in the rat. *J Comp Neurol, 258*(2), 204–229. https://doi.org/10.1002/cne.902580204

Wenzel, J. & Wenzel, K. (1812). *De Penitiori Structura Cerebri Hominis et Brutorum* (Cotta, Tübingen).

Ziehen, T. (1897-1901). Das Centralnervensystem der Monotremen und Marsupialier. *Denkschriften der Medicinisch-naturwissenschaftlichen Gesellschaft zu Jena, 6*, 1–187, 677–728.

Introduction to Chapter 2

The hypothalamus is made of a wide range of distinct neuronal subpopulations. These can be defined by the presence of neuropeptides or by mathematical means on large single-cell transcriptomic datasets (Mickelsen et al., 2020). RNA-based methods are a powerful tool that can identify scores of previously unknown neuronal populations. However, there is a strong possibility that a subset of transcriptomically defined populations would in fact be artifacts. One important caveat, as observed in our prelimiary work focused on tyrosine hydroxylase transcripts, is that mRNA transcripts do not always undergo translation. Indeed, combined transcriptomic and proteomic datasets often show minimal overlap (Schenk et al., 2019). It is also not guaranteed that mathematically detected clusters reflect neuronal populations that are meaningful on the basis of spatial organization, function, or connectivity. This project was aimed at clarifying the spatial distributions of the tyrosine hydroxylase (TH) expressing neurons in the hypothalamus as one step towards addressing these challenges.

This was a collaborative project conducted between the Khan lab and the group of Melissa Chee at Carleton University (Ottawa, Canada). The Chee lab is interested in the phenomenon of neurotransmitter co-release, and previous work has shown that dopaminergic neurons can also use GABA as a neurotransmitter. As a first step towards exploring this, we performed Nissl-based atlas mapping to determine the distributions of TH neurons that could also release GABA.

In this project, I worked closely with Kayla Schumacker and Rebecca Butler from the Chee lab to perform Nissl-based mapping and quantifications. Mikayla Payant performed validation of the transgenic mouse lines. Gabor Wittmann performed combined immunofluorescence and *in situ* hybridization. Melissa Chee designed the experiments and oversaw manuscript assembly

Chapter 2

Distributions of hypothalamic neuron populations co-expressing tyrosine hydroxylase and the vesicular GABA transporter in the mouse

Kenichiro Negishi[1,5]*, Mikayla A. Payant[2,5]*, Kayla S. Schumacker[2,5]*, Gabor Wittmann[3], Rebecca M. Butler[2], Ronald M. Lechan[3], Harry W. M. Steinbusch[4], Arshad M. Khan[1,6], Melissa J. Chee[2,6]

[1]UTEP Systems Neuroscience Laboratory, Department of Biological Sciences, and Border Biomedical Research Center, University of Texas at El Paso, El Paso, TX 79968, USA

[2]Department of Neuroscience, Carleton University, Ottawa, ON, K1S 5B6, Canada

[3]Department of Medicine, Division of Endocrinology, Diabetes and Metabolism, Tufts Medical Center, Boston, MA 02111, USA

[4]Department of Psychiatry and Neuropsychology, Section Cellular Neuroscience, Maastricht University, Maastricht, Netherlands

Author footnote: *KN, MAP, KSS contributed equally to the manuscript. AMK and MJC are joint senior authors.

Note: KN was supported for this work by NIH grant GM109817 (awarded to AMK).

This manuscript was reproduced from *The Journal of Comparative Neurology* with permission from John Wiley & Sons, Inc.

Abstract

The hypothalamus contains catecholaminergic neurons marked by the expression of tyrosine hydroxylase (TH). As multiple chemical messengers coexist in each neuron, we determined if hypothalamic TH-immunoreactive (ir) neurons express vesicular glutamate or GABA transporters. We used Cre/loxP recombination to express enhanced GFP (EGFP) in neurons expressing the vesicular glutamate (vGLUT2) or GABA transporter (vGAT), then determined whether TH-ir neurons colocalized with native EGFP^{Vglut2}- or EGFP^{Vgat}-fluorescence, respectively. EGFP^{Vglut2} neurons were not TH-ir. However, discrete TH-ir signals colocalized with EGFP^{Vgat} neurons, which we validated by in situ hybridization for *Vgat* mRNA. To contextualize the observed pattern of colocalization between TH-ir and EGFP^{Vgat}, we first performed Nissl-based parcellation and plane-of-section analysis, and then mapped the distribution of TH-ir EGFP^{Vgat} neurons onto atlas templates from the *Allen Reference Atlas* (*ARA*) for the mouse brain. TH-ir EGFP^{Vgat} neurons were distributed throughout the rostrocaudal extent of the hypothalamus. Within the *ARA* ontology of gray matter regions, TH-ir neurons localized primarily to the periventricular hypothalamic zone, periventricular hypothalamic region, and lateral hypothalamic zone. There was a strong presence of EGFP^{Vgat} fluorescence in TH-ir neurons across all brain regions, but the most striking colocalization was found in a circumscribed portion of the zona incerta (ZI)—a region assigned to the hypothalamus in the *ARA*—where every TH-ir neuron expressed EGFP^{Vgat}. Neurochemical characterization of these ZI neurons revealed that they display immunoreactivity for dopamine but not dopamine β-hydroxylase. Collectively, these findings indicate the existence of a novel mouse hypothalamic population that may signal through the release of GABA and/or dopamine.

Keywords: zona incerta, dopamine, hypothalamus, GABA, tyrosine hydroxylase, catecholamine, atlas

Introduction

The prevailing view of neurotransmission is that multiple chemical messengers can coexist, in various combinations, within single neurons and in some cases can even be co-stored in synaptic vesicles (Hökfelt et al., 1986). These chemical messengers may be neurotransmitters like glutamate and GABA that rapidly initiate and terminate discrete synaptic events, or neuromodulators like neuropeptides and catecholamines that can have varied release probabilities, time courses of release, or long-range target sites. In fact, virtually all neuropeptidergic neurons also harbor a neurotransmitter, as exemplified by brain structures in the hypothalamus. For example, neurons in the arcuate hypothalamic nucleus coexpress the neuropeptides Agouti-related protein and neuropeptide Y (Broberger, de Lecea, Sutcliffe, & Hökfelt, 1998; Broberger, Johansen, Johansson, Schalling, & Hökfelt, 1998; Hahn, Breininger, Baskin, & Schwartz, 1998) as well as the neurotransmitter GABA (Tong, Ye, Jones, Elmquist, & Lowell, 2008).

Colocalized neurotransmitters and neuromodulators may work in tandem or in opposition to prolong or suppress neuronal functions (van den Pol, 2012). For instance, neurons in the lateral hypothalamus that express either melanin-concentrating hormone (MCH) or hypocretin/orexin (H/O) have transcripts encoding the machinery for vesicular storage of glutamate (Mickelsen et al., 2017). Both of these neuronal populations can release glutamate and produce transient excitatory glutamatergic events (Chee, Arrigoni, & Maratos-Flier, 2015; Schöne, Apergis-Schoute, Sakurai, Adamantidis, & Burdakov, 2014), but MCH inhibits (Sears et al., 2010; Wu, Dumalska, Morozova, van den Pol, & Alreja, 2009) whereas H/O stimulates neuronal activity (Schöne et al., 2014). Additionally, these coexpressed messengers may also serve distinct functions. For example, MCH, but not glutamate from MCH neurons, promotes rapid eye movement sleep (Naganuma, Bandaru, Absi, Chee, & Vetrivelan, 2019), while glutamate has been shown to encode the nutritive value of sugars (Schneeberger et al., 2018) .

The colocalization between neuropeptides and catecholamines is also well-

studied. The catecholamines are a major class of monoamine messengers that include dopamine, norepinephrine, and epinephrine. Their presence in neurons can indirectly be suggested by the detection of immunoreactivity for tyrosine hydroxylase (TH; EC 1.14.16.2), which mediates the rate-limiting step in catecholamine biosynthesis (Nagatsu, Levitt, & Udenfriend, 1964; Udenfriend & Wyngaarden, 1956). Discrete populations of catecholamine-containing neurons (A Björklund & Lindvall, 1984; A Björklund & Nobin, 1973; Dahlström & Fuxe, 1964), and specifically TH-immunoreactive (ir) neurons (Hökfelt, Johansson, Fuxe, Goldstein, & Park, 1976; Hökfelt, Märtensson, Björklund, Kleinau, & Goldstein, 1984; van den Pol, Herbst, & Powell, 1984), have been detailed in the rat brain and include neurons in the hypothalamus. Hypothalamic TH-ir neurons are primarily found within the zona incerta (ZI) and periventricular parts of the hypothalamus (Hökfelt et al., 1976; Ruggiero, Baker, Joh, & Reis, 1984), which is composed of neurochemically and functionally diverse gray matter regions. For example, hypothalamic dopamine neurons may colocalize with galanin and neurotensin as well as with markers for GABA synthesis (Everitt et al., 1986). Furthermore, recent work has demonstrated that dopaminergic neurons in the arcuate nucleus co-release GABA (Zhang & van den Pol, 2015), and that both neurotransmitters regulate feeding in response to circulating metabolic signals (Zhang & van den Pol, 2016).

Single-cell RNA sequencing has revealed that neurochemically defined populations, such as hypothalamic TH-expressing neurons, can be further sorted into transcriptionally distinct subgroups (Romanov et al., 2017). Gene expression-based cluster analysis is a powerful tool for identifying subpopulations within seemingly homogeneous cell groups (Romanov et al., 2017). However, it is necessary for these transcriptomic studies to be supported and framed by accurate structural information (Crosetto, Bienko, & van Oudenaarden, 2015; Khan et al., 2018). Consideration of basic properties, such as morphology, connectivity, and spatial distributions can reveal groupings (Bota & Swanson, 2007), which would likely remain undetected by high-throughput transcriptomic analyses

alone. Indeed, for the hypothalamus, most published transcriptomic and proteomic analyses have ignored cytoarchitectonic boundary conditions of the diverse gray matter regions in this structure, opting instead to report gene expression patterns from the whole hypothalamus (Khan et al., 2018).

We therefore examined the spatial distributions of hypothalamic TH neurons and quantified the extent of their colocalization with other neurotransmitters or neuropeptides. We first determined whether hypothalamic TH-ir neurons may be either GABAergic or glutamatergic. By combining multi-label immunohistochemistry and enhanced green fluorescent protein (EGFP) reporter expression with cytoarchitectural analysis to obtain high spatial resolution maps of TH-ir neuronal subpopulations, we found that most hypothalamic TH-ir neurons coexpressed EGFP reporter expression for the vesicular GABA transporter ($EGFP^{Vgat}$), and that this colocalization was especially prevalent within a specific region of the rostral ZI. We further characterized the neurochemical identity of ZI $EGFP^{Vgat}$ TH-ir neurons and showed that these are dopamine-containing neurons, and that they do not appear to colocalize with known neuropeptides in the ZI region.

Materials and Methods

All animal care and experimental procedures were completed in accordance with the guidelines and approval of the Animal Care Committee at Carleton University. Mice were housed in ambient temperature (22–24°C) with a 12:12 light dark cycle with *ad libitum* access to water and standard mouse chow (Teklad Global Diets 2014, Envigo, Mississauga, Canada).

2.1 Generation of *Vgat-cre;L10-Egfp* and *Vglut2-cre;L10-Egfp mice*

To visualize GABAergic and glutamatergic neurons, respectively, we labeled neurons expressing the vesicular GABA transporter (vGAT; *Slc32a1*) or vesicular glutamate transporter 2 (vGlut2; *Slc17a6*) with an EGFP reporter by crossing a *Vgat-ires-cre* (Stock 028862, Jackson Laboratory, Bar Harbor, ME) or *Vglut2-ires-cre* mouse (Stock No. 16963, Jackson Laboratory) with a Cre-dependent *lox-STOP-lox-L10-Egfp* reporter mouse (Krashes et al., 2014), kindly provided by Dr. B. B. Lowell (Beth Israel Deaconess Medical Center, Boston, MA) to produce *Vgat-cre;L10-Egfp* and *Vglut2-cre;L10-Egfp* mice.

2.2 Antibody characterization

Table 1 lists the following primary antibodies we used for immunohistochemistry (IHC). All secondary antibodies (**Table 2**) were raised in donkey against the species of the conjugated primary antisera (mouse, goat, rabbit, or sheep).

Sheep anti-digoxigenin (DIG) antibody

When compared to tissue incubated with a DIG-labeled riboprobe followed with the anti-DIG antibody, no hybridization signals were detected when the tissue was incubated with the anti-DIG antibody only (Vazdarjanova et al., 2006).

Goat anti-dopamine antibody

The polyclonal anti-dopamine antibody was made and generously provided by

Prof. H. W. M. Steinbusch (Maastricht University, Maastricht, Netherlands). Specificity was determined through a gelatin model system and nitrocellulose sheets. The anti-dopamine antibody showed immunoreactivity to even low concentrations of dopamine, with cross-reactivity of less than 10% to noradrenaline, less than 1% to other monoamines, and low levels of cross-reactivity to L-DOPA at higher concentrations (Steinbusch, van Vliet, Bol, & de Vente, 1991).

Rabbit anti-dopamine β-hydroxylase (DBH)

Specificity was determined by the absence of staining when the antibody was preadsorbed by the DBH peptide (Sockman & Salvante, 2008). The distribution of DBH immunoreactivity was confirmed in the locus coeruleus (data not shown), a region known to express DBH, as previously shown (Yamaguchi, Hopf, Li, & de Lecea, 2018). This antibody has also been reported to reveal a distribution of hindbrain DBH-immunoreactive neurons that is similar to that revealed by a DBH antibody of different origin (Halliday & McLachlan, 1991).

Chicken anti-GFP antibody

Wild type brain tissue does not endogenously express the GFP transgene and incubating wild type brain tissue with this antibody did not produce any GFP-ir signals (data not shown).

Rabbit anti-GFP antibody

Specificity was determined by the absence of GFP immunoreactivity in the brain of wild type *Drosophila melanogaster*, which does not endogenously produce endogenous GFP molecules (Busch, Selcho, Ito, & Tanimoto, 2009).

Rabbit anti-melanin-concentrating hormone (MCH) antibody

The polyclonal anti-MCH antibody was made and generously provided by Dr. E. Maratos-Flier (Beth Israel Deaconess Medical Center, Boston, MA). Specificity was determined by the lack of MCH immunoreactivity after preadsorption with MCH peptide

(Elias et al., 1998) or after application to brain tissue from MCH knockout mice (Chee, Pissios, & Maratos-Flier, 2013).

Goat anti-orexin-A antibody

Specificity was demonstrated by preadsorption with orexin peptide, which abolished all specific staining shown with this antibody (Florenzano et al., 2006).

Mouse anti-tyrosine hydroxylase (TH) antibody

This antibody recognizes a single 62 kDa band that corresponds to the molecular weight of TH in Western blots of TH isolated from synaptosomal preparations (Wolf & Kapatos, 1989), brain homogenates (Carrera, Anadón, & Rodríguez-Moldes, 2012), or micropunches from frozen brain tissue sections (Shepard, Chuang, Shaham, & Morales, 2006). This antibody did not detect TH immunoreactivity following unilateral lesion of the compact part of the substantia nigra with 6-hydroxydopamine (Bourdy et al., 2014; Chung, Chen, Chan, & Yung, 2008) or ventral tegmental area with ibotenic acid (Bourdy et al., 2014) compared to the control, non-lesioned side. Knockdown of *th1* gene that encodes *Th* in the central nervous system of the zebrafish reportedly abolished detectable immunoreactivity from this antibody (Kuscha, Barreiro-Iglesias, Becker, & Becker, 2012).

2.3 Immunohistochemistry (IHC)

2.3.1 Tissue processing

Male and female *Vgat-cre;L10-Egfp*, *Vglut2-cre;L10-Egfp*, and wild type mice on a mixed C57BL/6, FVB, and 129S6 background (8–15 weeks old) were anesthetized with an intraperitoneal (ip) injection of urethane (1.6 g/kg) and transcardially perfused with cold (4°C) 0.9% saline followed by 10% neutral buffered formalin (4°C), unless indicated otherwise. The brain was removed from the skull, post-fixed with 10% formalin for 24 hours at 4°C, and then cryoprotected in phosphate-buffered saline (PBS; pH 7.4, 0.01 M) containing 20% sucrose and 0.05% sodium azide for 24 hours at 4°C. Brains were cut into four or five series of 30 µm-thick coronal-plane sections using a freezing microtome

(Leica SM2000R, Nussloch, Germany) and stored in an antifreeze solution containing 50% formalin, 20% glycerol, and 30% ethylene glycol.

To examine dopamine immunoreactivity, *Vgat-cre;L10-Egfp* brains were perfused with cold (4°C) saline and then 1% glutaraldehyde:9% formalin mixture (4°C). The brains were post-fixed in the perfusion solution for 30 minutes and cryoprotected with 30% sucrose solution for 24 hours (4°C). Brains were cut into five series of 30 µm-thick sections and collected into a PBS-azide solution containing 1% formalin. All aforementioned perfusion and incubation solutions contained 1% sodium metabisulfite to prevent the oxidation of dopamine.

2.3.2 Procedure

Single- and dual-label IHC were completed as previously described (Chee et al., 2013), unless indicated otherwise, using the antibodies and dilution combinations listed in **Tables 1** and **2**. In brief, brain tissue sections were washed with six 5-minute PBS exchanges and then blocked for 2 hours at room temperature (RT, 20–21 °C) with 3% normal donkey serum (NDS; Jackson ImmunoResearch Laboratories, Inc., West Grove, PA) dissolved in PBS-azide containing 0.25% Triton X-100 (PBT-azide). Unless indicated otherwise, primary antibodies were concurrently added to the blocking serum and incubated with the brain sections overnight (16–18 hours, RT). After washing with six 5-minute PBS rinses, the appropriate secondary antibodies were diluted in PBT containing 3% NDS and applied to the brain tissue sections for 2 hours (RT). The sections were rinsed with three 10-minute PBS washes before being mounted on SuperFrost Plus glass microscope slides (Fisher Scientific, Pittsburgh, PA) and coverslipped (#1.5 thickness) using ProLong Gold antifade reagent containing DAPI (Fisher Scientific).

To examine dopamine immunoreactivity, *Vgat-cre;L10-Egfp* brain tissues were incubated in PBS containing 0.5% sodium borohydride for 30 minutes at RT, followed by six 5-minute washes in PBS. The brain sections were then blocked with 3% NDS in PBT-azide for 2 hours prior to the simultaneous overnight-incubation (RT) of primary antibodies

against GFP (anti-chicken) and TH, then washed with six 5-minute exchanges in PBS, and incubated with the corresponding Alexa Fluor 488- and Alexa Fluor 568-conjugated secondary antibodies in 3% NDS for 2 hours. After three 10-minute PBS rinses of the tissue sections, we diluted the dopamine primary antibody into a 3% NDS, PBT-azide solution and incubated the sections in this solution overnight at RT. The sections were rinsed with PBS six times for 5 minutes each before incubating them with the corresponding Alexa Fluor 647-conjugated secondary antibody in 3% NDS-PBT. Following three 10-minute washes in PBS, the brain sections were mounted and coverslipped. All solutions used to process the visualization of dopamine immunoreactivity contained 1% sodium metabisulfite to prevent the oxidation of dopamine.

2.4 Dual fluorescence *in situ* hybridization (fISH) and IHC

2.4.1 Tissue preparation for fISH

Vgat-cre;L10-Egfp mice were anesthetized with urethane (1.6 g/kg, ip), and their brains were rapidly removed and snap-frozen on powdered dry ice. The brains were warmed to –16°C and sliced into ten series of 16 µm-thick coronal sections through the entire hypothalamus using a cryostat (CM3050 S, Leica Microsystems, Buffalo Grove, IL). Each section was thaw-mounted on Superfrost Plus slides (Fisher Scientific), air-dried at RT, and then stored at –80°C until processed for fISH.

2.4.2 fISH and IHC procedure

The antisense vGAT riboprobe corresponds to nucleotide 875–1,416 of mouse *Slc32a1* mRNA (*Vgat*; NM_009508.2) (Agostinelli et al., 2017). Using a plasmid linearized with SacI (New England Biolabs, Beverly, MA), it was transcribed with T7 polymerase (Promega, Madison, WI) in the presence of digoxigenin (DIG)-conjugated UTP (Roche Diagnostics, Mannheim, Germany).

fISH for *Vgat* mRNA was performed according to the protocol previously described for fresh frozen sections (Wittmann, Hrabovszky, & Lechan, 2013). In brief, prior to

hybridization, the sections were fixed with 4% paraformaldehyde for 20 minutes and rinsed with two 3-minute PBS washes; acetylated with 0.25% acetic anhydride in 0.1 M triethanolamine and rinsed with two PBS washes; then dehydrated in an ethanol gradient starting from 80%, 95%, to 100% for 1 minute each, chloroform for 10 minutes, and again in 100% and 95% ethanol for 1 minute each. The riboprobe (650 pg/µl) was mixed with hybridization buffer containing 50% formamide, 2× sodium citrate buffer (SSC), 1× Denhardt's solution (MilliporeSigma, Burlington, MA), 0.25 M Tris buffer (pH 8.0), 10% dextran sulfate, 3.5% dithiothreitol, 265 µg/ml denatured salmon sperm DNA (MilliporeSigma), and applied directly to each slide under a plastic Fisherbrand coverslip (Fisher Scientific). Hybridization occurred overnight at 56°C in humidity chambers. Following hybridization, we removed the coverslip and the sections were washed in 1× SSC for 15 minutes; treated with 25 µg/ml RNase A (MilliporeSigma) dissolved in 0.5 M NaCl, 10 mM Tris, 1 mM EDTA (pH 8.0) for 1 hour (37°C); sequentially washed at 65°C with 1× SSC for 15 minutes, 0.5× SSC for 15 minutes, and 0.1× SSC for 1 hour. Subsequently, the sections were treated with PBS containing 0.5% Triton X-100 and 0.5% H_2O_2 (pH 7.4) for 15 minutes, rinsed in three 10-minute PBS washes, then immersed in 0.1 M maleate buffer (pH 7.5) for 10 minutes before blocking in 1% Blocking Reagent (Roche) for 10 minutes. The sections were incubated in horseradish peroxidase-conjugated, sheep anti-DIG antibody in blocking reagent and enclosed over sections with a CoverWell incubation chamber (Grace Bio-Labs Inc., Bend, OR) overnight at 4°C. After rinsing with three 10-minute PBS washes, the hybridization signal was amplified with a TSA Plus Biotin Kit (Perkin Elmer, Waltham, MA), by diluting the TSA Plus biotin reagent (1:400) in 0.05 M Tris (pH 7.6) containing 0.01% H_2O_2, for 30 minutes. The sections were incubated with streptavidin-conjugated Alexa Fluor 555 (1:500; S32355, Invitrogen; RRID: AB_2571525) in 1% Blocking Reagent for 2 hours (RT) to label the *Vgat* mRNA hybridization signal.

Following fISH, we processed the sections for immunofluorescence by incubating

them with a GFP (rabbit) antibody, rinsing with three 10-minute PBS washes, and labeling with an Alexa Fluor 488-conjugated anti-rabbit secondary (**Table 2**). Finally, the sections were washed in PBS and coverslipped with Vectashield mounting medium containing DAPI (H-1200, Vector Laboratories, Burlingame, CA).

2.5 Nissl staining

Free-floating brain sections were mounted onto dust-free gelatin-coated slides and air dried overnight at RT. Sections were dehydrated using ascending concentrations of ethanol (50%, 70%, 95%, and 3× 100% for 3 minutes each) and delipidized in mixed-isomer xylenes for 25 minutes. Sections were then rehydrated in decreasing concentrations of ethanol (100%, 95%, 70%, and 50% for 3 minutes each) and rinsed with distilled water (3 minutes) before staining with 0.25% w/v solution of the thiazine dye, thionine (Kiernan, 2001), made from thionin acetate (Lenhossék, 1895) (861340, MilliporeSigma; pH 4.5, RT) for 30 seconds. Immediately after thionine staining, the sections were rinsed in water; differentiated with 0.4% glacial acetic acid in deionized water by dipping the slides for up to one minute until the gray and white matter were distinguished clearly from each other; then dehydrated in ascending concentrations of ethanol (50%, 70%, 95%, and 3× 100% for 3 minutes each). The brain tissue sections were cleared in mixed-isomer xylenes for 25 minutes, and the slides were coverslipped with DPX Mountant (Millipore Sigma).

2.6 Microscopy

All images were exported as TIFF files into Adobe Illustrator CS4 (Adobe Systems Inc., San Jose, CA) for assembly into multi-panel figures and to add text labels and arrowheads.

2.6.1 Epifluorescence imaging

Images showing the colocalization between *Vgat* mRNA and GFP-ir in *Vgat-cre;L10-Egfp* tissue were captured using a Zeiss Axioplan 2 microscope (Carl Zeiss Inc., Göttingen, Germany) equipped with a RT SPOT digital camera (Diagnostic Instruments,

Sterling Heights, MI). Adobe Photoshop CS4 (Adobe) was used to create composite images and to modify brightness or contrast to increase the visibility of lower level signals. Large field-of-view images of whole brain sections were acquired with a fully motorized Nikon Ti2 inverted microscope (Nikon Instruments Inc., Mississauga, Canada) mounted with a Prime 95B CMOS camera (Photometrics, Tucson, AZ) using a CF160 Plan Apochromat ×20 objective lens (0.75 numerical aperture). Images were stitched using NIS Elements software (Nikon), which was also used to adjust image brightness and contrast.

2.6.2 Confocal imaging

High-magnification confocal stacks (2048 × 2048 pixels) involving two- or three-color fluorescence channels were viewed using a Nikon C2 confocal microscope fitted with Plan Apochromat ×20 (0.75 numerical aperture) or ×40 (0.95 numerical aperture) objective lenses and acquired using NIS Elements software (Nikon). The excitation light was provided by 488-nm, 561-nm, and 640-nm wavelength lasers for the visualization of Alexa Fluor 488, Alexa Fluor 568, and Alexa Fluor 647, respectively. We used NIS Elements to stitch overlapping frames, flatten confocal stacks by maximum intensity projection, and adjust the brightness or contrast of flattened images. Two-color images were coded in green (Alexa Fluor 488) and pseudo-colored magenta (Alexa Fluor 568). Three-color images were coded in green (Alexa Fluor 488), red (Alexa Fluor 568), and pseudo-colored light blue (Alexa Fluor 647).

2.7 Nissl-based parcellations, plane-of-section analysis, and atlas-based mapping

An Olympus BX53 microscope (Olympus Corporation, Tokyo, Japan) was used to examine Nissl-stained tissue sections. Photomicrographs were produced with an Olympus DP74 color camera powered by CellSens Dimension software (Version 2.3). Contrast enhancements and brightness adjustments were made with Photoshop (Version

CS6; Adobe) before analyses. Photomicrographs of Nissl-stained tissue were imported to Adobe Illustrator (Version CC 2014, Adobe) and regional boundaries were drawn on a separate data layer. Line parcellations were made using the nomenclature and boundary definitions of the *Allen Reference Atlas* (*ARA*; Dong, 2008). To the extent that was applicable, cytoarchitectural criteria outlined in Swanson's rat brain atlas (Swanson, 2018) were also used to clarify delineations. Parcellations were then carefully superimposed on corresponding fluorescence images to precisely reveal the spatial distributions of TH- and vGAT-ir neurons. We photographed fluorescently-immunostained tissue sections using a Zeiss Axio Imager M.2 microscope (Carl Zeiss Corporation, Thornwood, NY) using ×10 (0.3 numerical aperture) and ×20 (0.8 numerical aperture) Plan Apochromat objective lenses. An EXi Blue monochrome camera (Teledyne Qimaging, Inc., Surrey, British Columbia, Canada) was used to capture multi-channel fluorescence images and a motorized stage controlled by Volocity Software (Version 6.1.1; Quorum Technologies, Inc., Puslinch, Ontario, Canada) aided in generating stitched mosaic images. Image files were then exported in TIFF format to allow further processing using Adobe Photoshop.

Using the parcellations that were superimposed onto the corresponding epifluorescence image, cells that existed within the parcellated boundaries were marked using the *Blob Brush* tool in Adobe Illustrator. A red circle represented a TH-positive cell, and a blue circle represented a TH- and vGAT-positive cell. Plane-of-section analysis (Zséli et al., 2016) was performed to assign each photographed tissue section or portion thereof to the appropriate ARA reference atlas level(s). The cell representations were then superimposed onto the corresponding ARA reference atlas template (Dong, 2008) for each atlas level, thus creating atlas-based maps of the tissue of interest.

2.8 Cell counting

The numbers of cells counted from the procedures below are semi-quantitative measures meant to provide data for relative comparisons rather than absolute cell numbers within the hypothalamus.

2.8.1 Quantification of Vgat hybridization signals

We acquired stitched epifluorescence images for whole hypothalamic sections using a ×10 objective on a fully motorized Olympus BX61VS microscope running VS-ASW-FL software (Olympus). We viewed the images offline using OlyVIA software (Olympus) in order to quantify the colocalization of *Vgat* hybridization signals, which expressed red fluorescence, in GFP-ir neurons from *Vgat-cre;L10-Egfp* brain tissue. Cells were counted using a grid comprising 1-inch × 1-inch squares that was printed on a transparency such that each square, when overlaid onto the magnified image on the computer screen, encompassed a 2.4-mm^2 area of the hypothalamus. We counted from one hemisphere and placed the first counting square starting at the ventral edge of the base of the brain, i.e., at the median eminence, then working up to 1.7 mm dorsally (or until the ventral edge of the thalamus where no GFP-ir neurons were observed) and up to 1.4 mm laterally and away from the third ventricle until the cerebral peduncle. We counted the total number of GFP-ir neurons from every brain section within one series (out of 10), as prepared in Section 2.4.1. To avoid double-counting, cells that landed on the gridlines were not included in the count.

We applied the Abercrombie formula to correct for oversampling error (Abercrombie, 1946) in our total cell count using the equation $P = A(M/(L+M))$ where P is the corrected cell count reported; A is the original cell count; M is the mean tissue thickness; and L is the mean cell diameter (in μm). We determined the tissue thickness following tissue processing by confocal imaging using the ×40 objective, and the mean tissue thickness from this experiment was 11 μm. The diameter of each of 100 neurons throughout the hypothalamus of *Vgat-cre;L10-Egfp* brain tissue was determined by calculating the mean length of two perpendicular line vectors placed across the soma of each neuron using NIS Elements (Nikon); the mean cell diameter is 12.7 μm. The percentage of colocalization was calculated by determining the total number of *Vgat* mRNA neurons relative to the total number of GFP-ir neurons in the whole hypothalamus of one brain.

2.8.2 Quantification of EGFP^{Vgat} or EGFP^{Vglut2} fluorescence and TH immunoreactivity

We acquired stitched epifluorescence images using a ×10 objective (0.3 numerical aperture) on an Olympus BX53 microscope mounted with the Olympus DP74 camera, and mean cell counts were determined using Adobe Illustrator CS5 (Adobe) across three brains. In every brain section within one series (out of five), as prepared in Section 2.3.1, we counted all neurons displaying TH immunoreactivity, which exhibited red fluorescence, and determined the proportion of these neurons that also displayed EGFP^{Vgat} or EGFP^{Vglut2} fluorescence.

We applied the Abercrombie correction for oversampling as described in Section 2.8.1. The mean tissue thickness for this experiment was 20 µm. The mean cell diameter was determined from 3–6 TH-ir neurons from *Vgat-cre;L10-Egfp* brain tissue within each parcellated region of the hypothalamus. The mean cell diameter used for applying the Abercrombie correction factor for that region ranged between 9.3 µm and 16.4 µm. The values reported reflect the corrected mean number of neurons counted in each region. The percentage of colocalization was calculated with respect to the parcellation-based cytoarchitectural boundaries and only the neurons that fell within the defined boundaries were counted, unless indicated otherwise in the Results.

2.9 Statistics

Line of best-fit for linear regressions was determined using Prism 6.07 (GraphPad Software Inc., San Diego, CA). All frequency distribution histograms were generated with Prism. All data are expressed as the mean ± standard error of the mean (SEM).

Results

3.1 Catecholaminergic neurons in the hypothalamus may be GABAergic

Catecholaminergic neurons are distributed throughout the hypothalamus (A Björklund & Lindvall, 1984; Dahlström & Fuxe, 1964; Hökfelt et al., 1976; Ruggiero et al., 1984; van den Pol et al., 1984), and we determined if they may coexpress the neurotransmitter glutamate or GABA, which can be marked by their expression of vGLUT2 or vGAT, respectively. We therefore examined if TH-ir neurons in *Vglut2-cre;L10-Egfp* and *Vgat-cre;L10-Egfp* mouse brain tissue, respectively, also express native EGFP fluorescence ($EGFP^{Vglut2}$ or $EGFP^{Vgat}$). Interestingly, we did not observe any colocalization between TH-ir and $EGFP^{Vglut2}$ neurons from the hypothalamus (**Figure 1**); in contrast, colocalization between TH-ir and $EGFP^{Vgat}$ was readily evident (**Figure 2**). These observations suggested that hypothalamic TH-ir neurons may be GABAergic.

We evaluated the efficacy and specificity of native EGFP fluorescence to indicate vGAT-expressing neurons in *Vgat-cre;L10-Egfp* mice by assessing the colocalization of *Vgat* mRNA hybridization signal (*Vgat*-ISH) in $EGFP^{Vgat}$ neurons labeled with an anti-GFP antibody to identify GFP immunoreactivity (**Figure 3**). We counted GFP-ir neurons from one hemisphere of the hypothalamus and found that more than 99% of GFP-ir neurons (8,855 out of 8,906) expressed *Vgat*-ISH signals. Thus, $EGFP^{Vgat}$-positive neurons have nearly complete one-to-one correspondence with *Vgat*-ISH signal in the hypothalamus. Furthermore, less than 1% of the *Vgat*-ISH neurons (64 out of 8,919) counted were not GFP-ir in the hypothalamus, so the likelihood of under-reporting a *Vgat*-positive neuron was minimal. These findings validated the use of the *Vgat-cre;L10-Egfp* mouse model for unambiguous detection of EGFP *Vgat* hypothalamic neurons by native EGFP fluorescence.

3.2 Distribution of $EGFP^{Vgat}$ TH-ir neurons in the hypothalamus

The hypothalamus includes gray matter regions starting rostrally at the level of the anteroventral periventricular nucleus (AVP) and proceeding caudally until the emergence

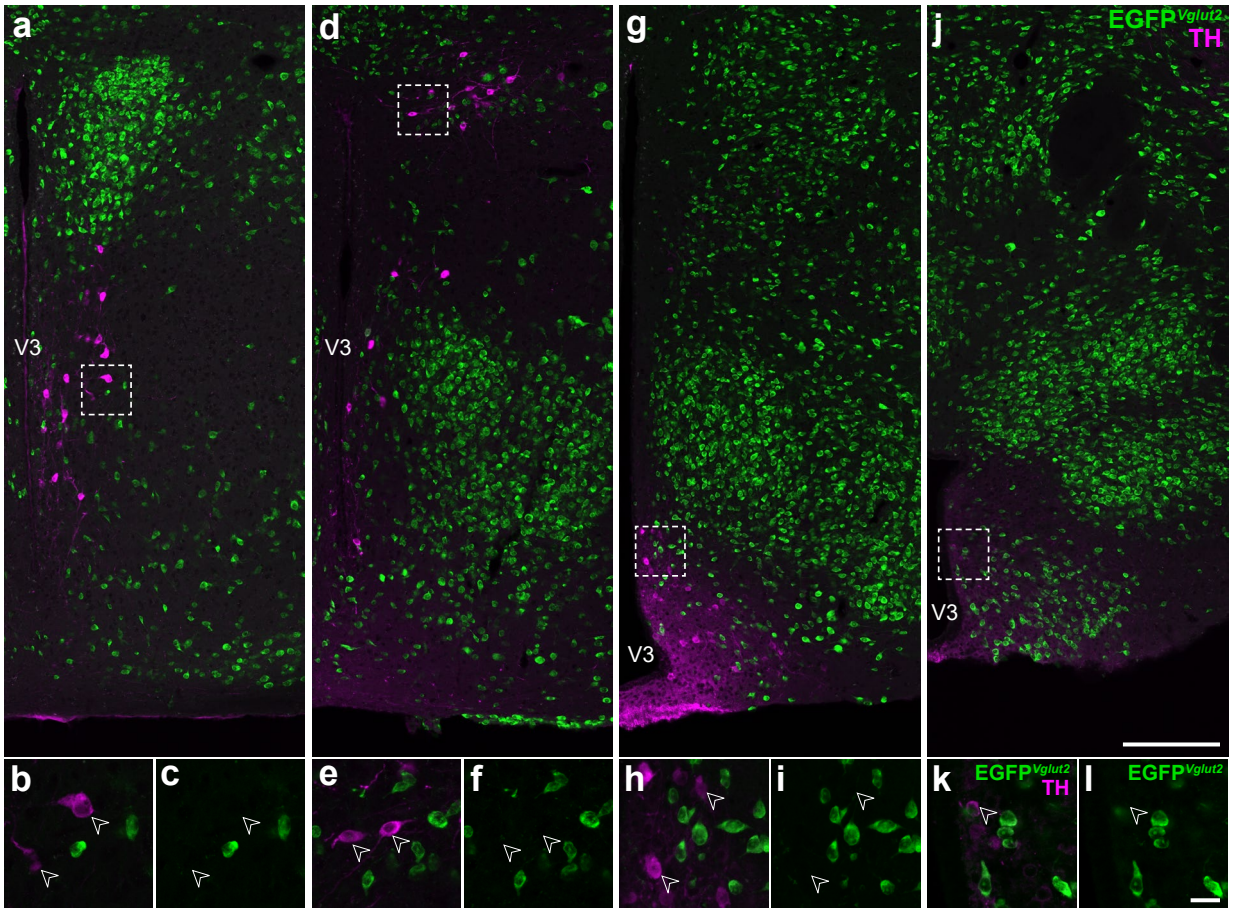

Figure 1. Hypothalamic TH-expressing neurons do not colocalize with EGFP^{Vglut2} fluorescence. Representative stitched confocal photomicrographs showing the medial hypothalamic zone within 600 μm of the third ventricle (V3) in *Vglut2-cre;L10-Egfp* mice at the inferred anteroposterior positions (in mm) from Bregma: –0.5 (***a***), –1.3 (***d***), –1.6 (***g***), and –2.2 (***j***). Merged-channel confocal photomicrographs (***b***, ***e***, ***h***, ***k***) from the respective outlined areas (from ***a***, ***d***, ***g***, ***j***) indicate that TH-ir neurons (open arrowheads) do not express EGFP^{Vglut2} (green; ***c***, ***f***, ***i***, ***l***). Scale bars: 200 μm in ***j*** also applies to ***a***, ***d***, ***g***; 20 μm in ***l*** also applies to ***b***, ***c***, ***e***, ***f***, ***h***, ***i***, ***k***. Label in ***j*** applies to ***a***, ***d***, ***g***; ***k*** applies to ***b***, ***e***, ***h***; ***l*** applies to ***c***, ***f***, ***i***. V3, third ventricle.

of the ventral tegmental area. In the mouse, the hypothalamus extends approximately 3 mm along the anteroposterior axis (+0.445 to –2.48 mm from Bregma), and this distance is represented across 33 levels (L; L50–L83) in the reference space of the ARA (Dong, 2008). We observed TH-ir neurons throughout the entire rostrocaudal extent of the hypothalamus, where they were dispersed in numerous gray matter regions. We evaluated the distributions of TH-ir neurons across the *ARA* reference space (**Figure 4a**), including EGFP^{Vgat} TH-ir neurons (**Figure 4b**). Overall, there was a strong linear

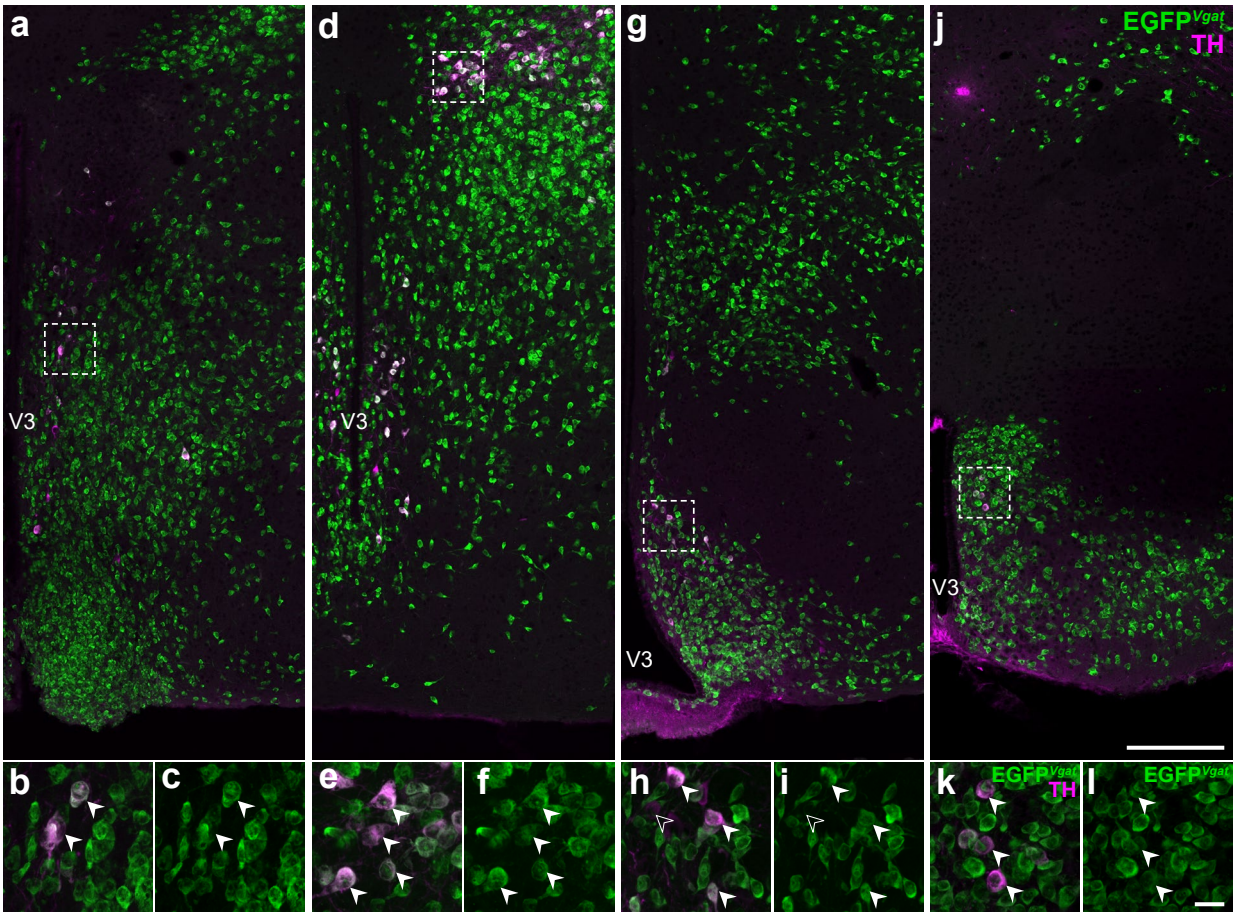

Figure 2. Some hypothalamic TH-expressing neurons colocalize with EGFP^{Vgat} fluorescence. Representative stitched confocal photomicrographs showing the medial hypothalamic zone within 600 μm of the third ventricle (V3) in *Vgat-cre;L10-Egfp* mice at the inferred anteroposterior positions (in mm) from Bregma: –0.5 (***a***), –1.3 (***d***), –1.6 (***g***), and –2.2 (***j***). Merged-channel confocal photomicrographs (***b***, ***e***, ***h***, ***k***) from the respective outlined areas in (***a***, ***d***, ***g***, ***j***) indicate that the vast majority of TH-ir neurons (filled arrowheads) coexpress EGFP^{Vgat} (green; ***c***, ***f***, ***i***, ***l***). Open arrowheads (***h***, ***i***) mark TH-ir neurons that do not coexpress EGFP^{Vgat}. Scale bars: 200 μm in ***j*** also applies to ***a***, ***d***, ***g***; 20 μm in ***l*** also applies to ***b***, ***c***, ***e***, ***f***, ***h***, ***i***, ***k***. Label in ***j*** applies to ***a***, ***d***, ***g***; ***k*** applies to ***b***, ***e***, ***h***; ***l*** applies to ***c***, ***f***, ***i***. V3, third ventricle.

relationship between the total number of TH-ir neurons and the number of EGFP^{Vgat} TH-ir neurons (r = 0.973, R2 = 0.947; **Figure 4c**).

In order to increase the spatial resolution for visualizing the distribution of TH-ir neurons in the hypothalamus, we mapped their locations onto *ARA* atlas templates that are available as electronic vector-object files (Dong, 2008) (**Figure 5**) and quantified the proportion of EGFP^{Vgat} TH-ir neurons in each parcellated gray matter region of the hypothalamus (**Table 3**). All regions with detectable labeling of TH-ir neurons are tabulated

using the hierarchical organization of brain structures presented by the ARA (Allen Institute for Brain Science, 2011b). The colocalization of TH immunoreactivity with EGFP^{Vgat} occurred at low (<50%), moderate (50–80%), or high frequencies (>80%) of colocalization.

3.2.1 The periventricular zone

The TH-ir neurons in the periventricular zone were distributed within three main brain regions: the paraventricular hypothalamic nucleus (PVH), periventricular hypothalamic nucleus (PV), and arcuate hypothalamic nucleus (ARH) (**Table 3**). These neurons were distributed across L56–L74 and were moderately to highly (63–91%) colocalized with EGFP^{Vgat}, which showed a very strong linear relationship with the overall numbers of TH-ir neurons in this zone (r = 0.995, R2 = 0.990; **Figure 4d**–**f**).

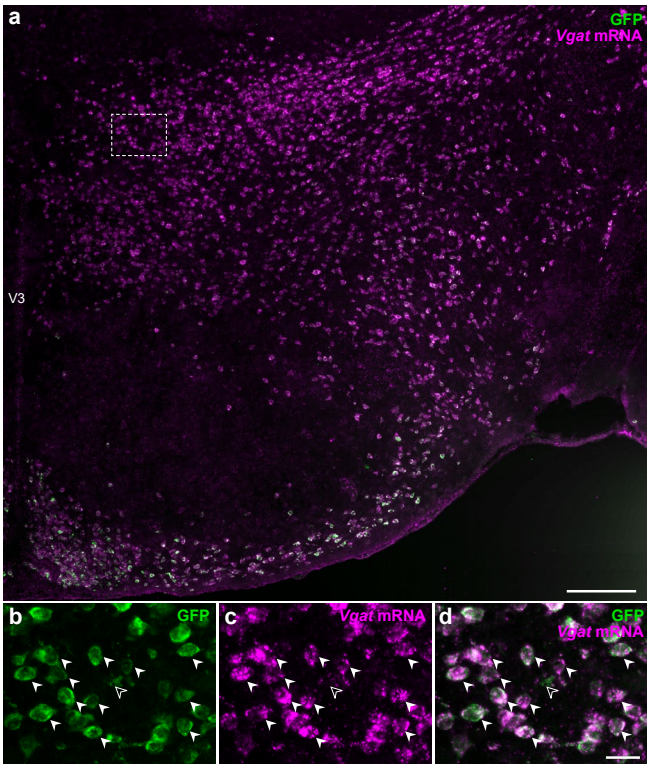

Figure 3. Visualization of vGAT-expressing neurons by GFP fluorescence. Epifluorescence photomicrograph showing *Vgat* mRNA hybridization signals in GFP-ir neurons from *Vgat-cre;L10-Egfp* mice. High magnification photomicrographs from the outlined area (from ***a***) show that almost all GFP-ir neurons (***b***) express *Vgat* mRNA hybridization signal (***c***) in the merged-channel image (***d***). Filled arrowheads indicate representative *Vgat*-ISH and GFP-ir colocalized neurons while open arrowheads point to a GFP-ir neuron that is *Vgat*-negative. Scale bars: 200 µm (***a***); 25 µm (***b***–***d***). V3, third ventricle.

TH-ir neurons in the PVH were largely confined to its parvicellular division and were most numerous within the anterior parvicellular part (PVHap), and 90% of PVHap TH-ir neurons were EGFP^{Vgat}-positive (**Table 3**; L56–L59; **Figure 5c**–**f**). In contrast, the dorsal zone (PVHmpd; **Table 3**) or periventricular part (PVHpv; L56–59; **Figure 5c**–**f**; **Table 3**) of the parvicellular PVH contained much fewer TH-ir neurons, and 60% and 63% of PVHmpd and PVHpv neurons, respectively, were also EGFP^{Vgat}-positive (**Table 3**).

Most of the TH-ir neurons in the periventricular zone abutted the third ventricle.

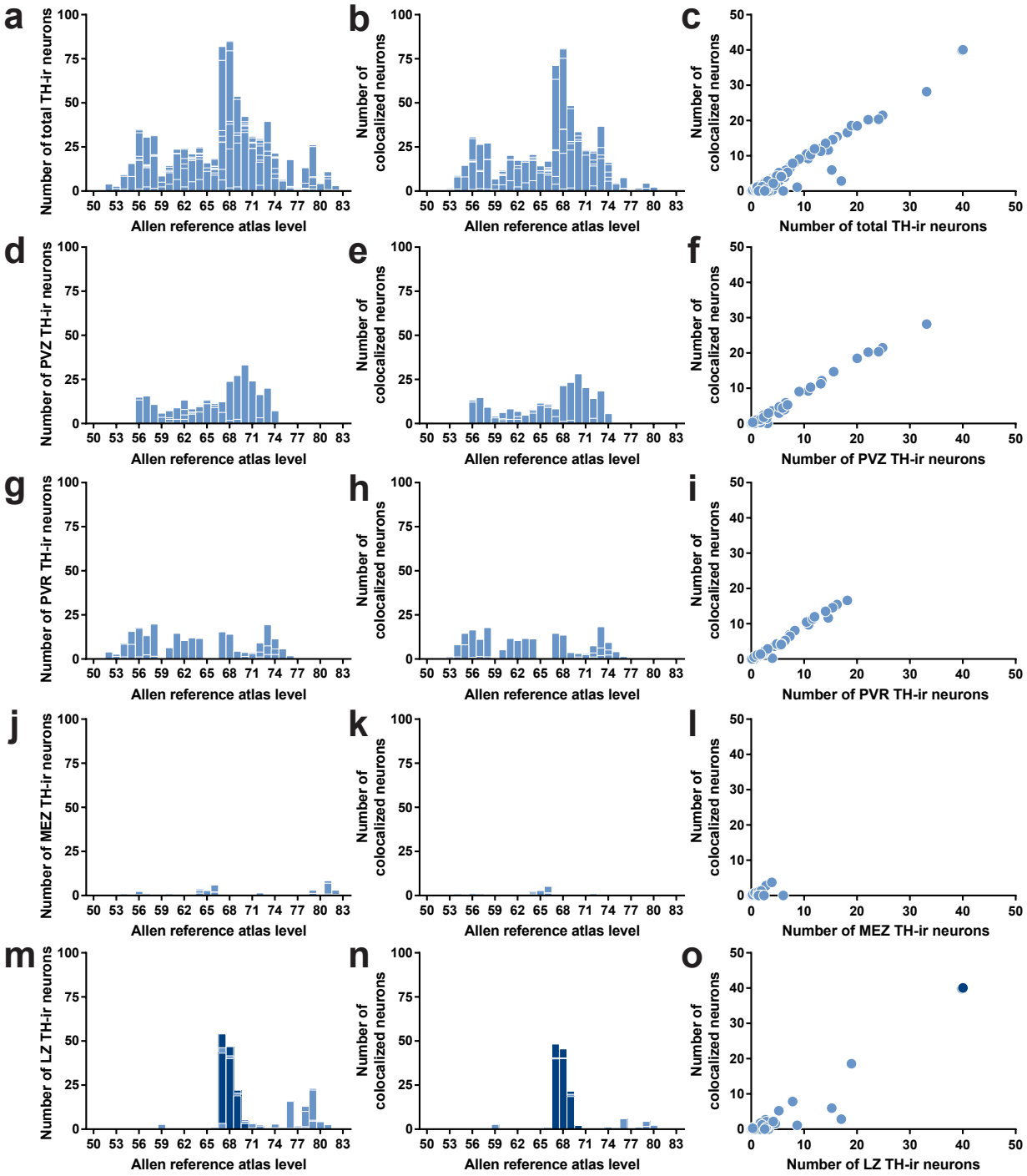

Figure 4. Distributions of TH-ir neurons with the colocalization of EGFP^{Vgat} in Vgat-cre;L10-Egfp brain tissue. Number of TH-ir neurons (***a***, ***d***, ***g***, ***j***, ***m***) that coexpress EGFP^{Vgat} (***b***, ***e***, ***h***, ***k***, ***n***) at each atlas level throughout the whole hypothalamus (***a***, ***b***), periventricular hypothalamic zone (PVZ; ***d***, ***e***), periventricular hypothalamic region (PVR; ***g***, ***h***), hypothalamic medial zone (MEZ; ***j***, ***k***), and hypothalamic lateral zone (LZ; ***m***, ***n***). Correlation between the coexpression of EGFP^{Vgat} in TH-ir neurons at all brain regions in each atlas level of the whole hypothalamus (***c***), PVZ (***f***), PVR (***i***), MEZ (***l***), and LZ (***o***). Dark blue bars in ***m*** and ***n*** and the dark blue filled circles in ***o*** correspond to regions within the zona incerta.

Within this zone, the entire periventricular hypothalamic nucleus that was mapped extended through 15 atlas levels, including the anterior (PVa) and intermediate (PVi) parts, and 84–90% of TH-ir neurons in this region were also EGFP^{Vgat}-positive (L59–74; **Figure 5f**–**r**; **Table 3**). Notably, the middle anteroposterior portion of the PVi (L65–L67) expressed the most EGFP^{Vgat} TH-ir neurons (**Figure 5j**–**l**). In the ARH, TH-ir neurons were distributed throughout the entire rostrocaudal extent of the structure but were most abundant within the dorsomedial aspect of the ARH at L68–L71 (**Figure 5m**–**p**). TH-ir neurons were distributed in varying densities through the ARH along its anteroposterior expanse, and 73–88% of these neurons were also EGFP^{Vgat}-positive (**Table 3**).

3.2.2 The periventricular region

The periventricular region included brain regions across virtually the entire rostrocaudal extent of the hypothalamus, though TH-ir neurons were clustered either toward its rostral (L52–L63) or caudal portions (L67–L76) (**Figure 4g**–**h**). Overall, most TH-ir neurons in the periventricular region were also EGFP^{Vgat}-positive (r = 0.992, R2 = 0.983; **Figure 4i**), but we found regional differences at several atlas levels.

Within the rostral periventricular region, TH-ir neurons were most abundant in the preoptic part of the periventricular hypothalamic nucleus (PVpo; L54–58), and 93% of these neurons were also EGFP^{Vgat}-positive (**Table 3**; **Figure 5b**–**e**). Colocalized neurons that fell on or immediately outside the parcellated boundaries of PVpo in L57 were provisionally included in the cell counts for PVpo (**Figure 5d**). There were also notable TH-ir neurons in the subparaventricular zone (SBPV; L60–63) that displayed very high colocalization with EGFP^{Vgat} (**Table 3**; **Figure 5g**–**h**). Other areas in the periventricular hypothalamic

Figure 5. Mapped distributions of EGFP^{Vgat} TH-ir neurons in the hypothalamus. Representative coronal maps, arranged from rostral to caudal order (***a***–***w***), show the distributions of TH-ir neurons that colocalize (blue circles) or do not colocalize (red circles) with EGFP^{Vgat} from *Vgat-cre;L10-Egfp* mice. Consultation of Nissl-stained tissue guided the assignment of neurons to parcellated cytoarchitectonic boundaries in the TH-ir tissue, and plane-of-section analysis facilitated their mapping to gray matter regions of the *ARA* reference atlas templates. Each panel includes a portion of the atlas template for a given *ARA* level, the numerical designation of the atlas level (bottom left), the corresponding inferred stereotaxic coordinate from Bregma (β; bottom right), and the brain region labels adopted from formal nomenclature of the *ARA* (Dong, 2008).

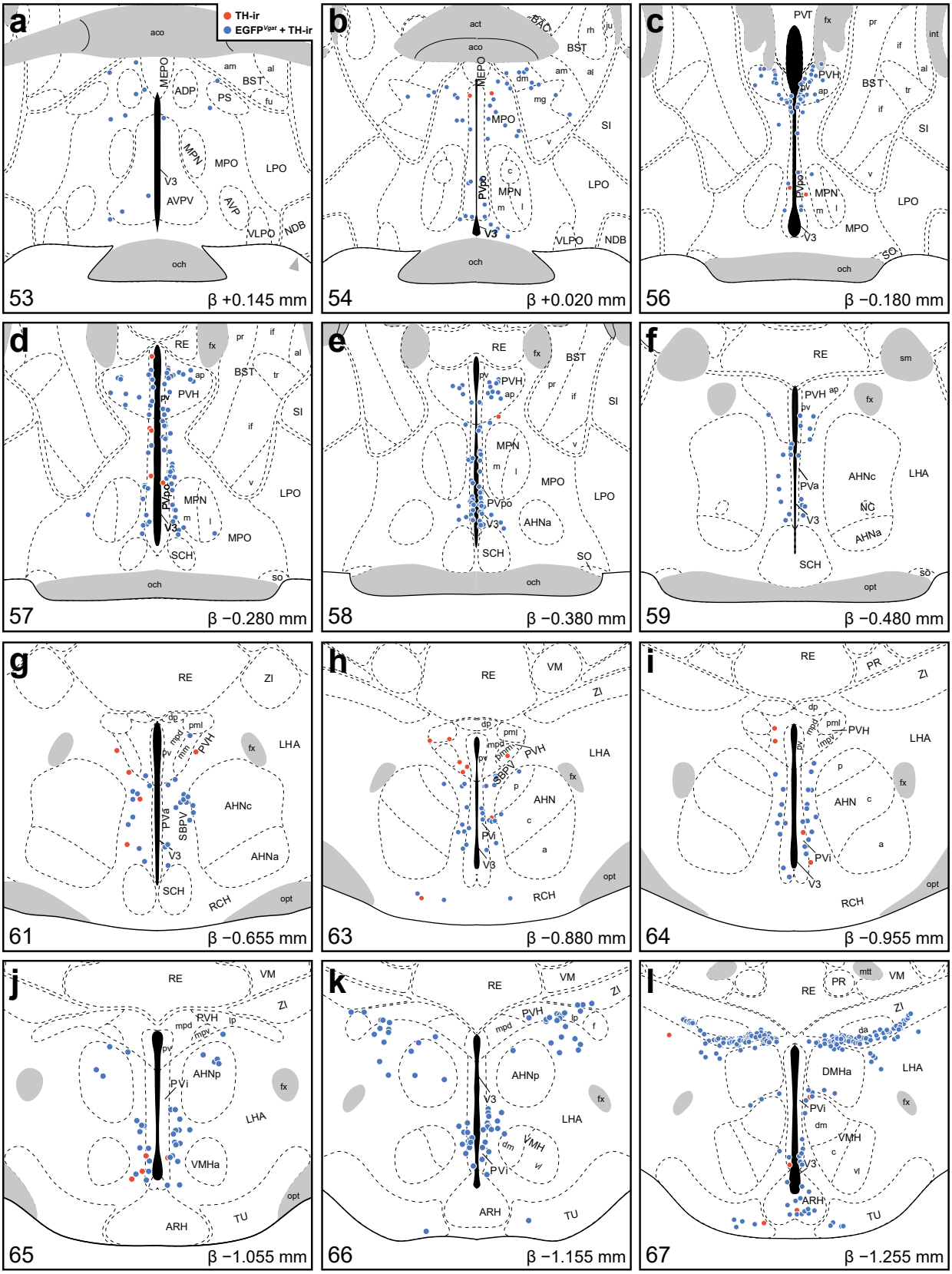

Figure 5. (see previous page)

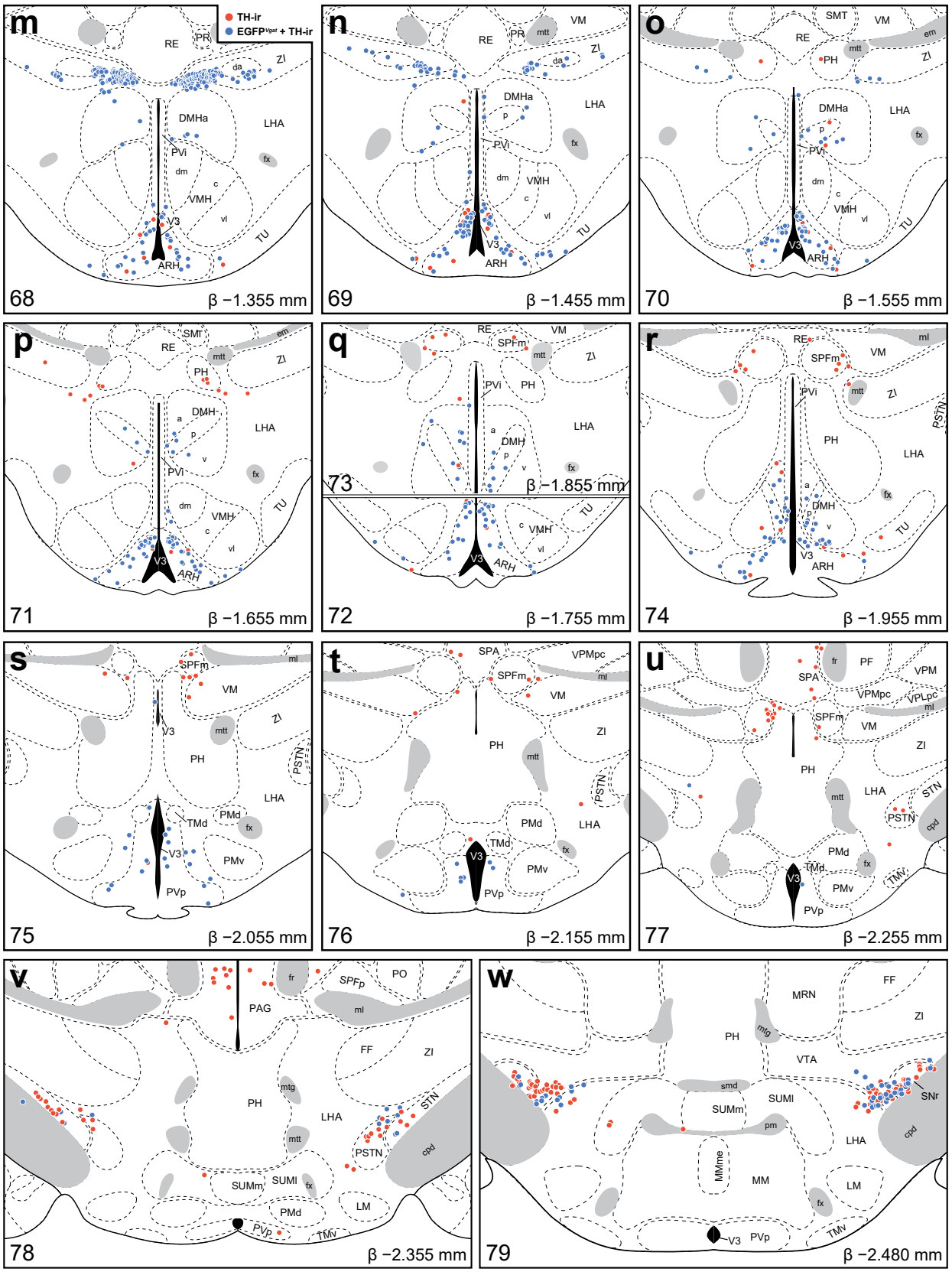

Figure 5 continued.

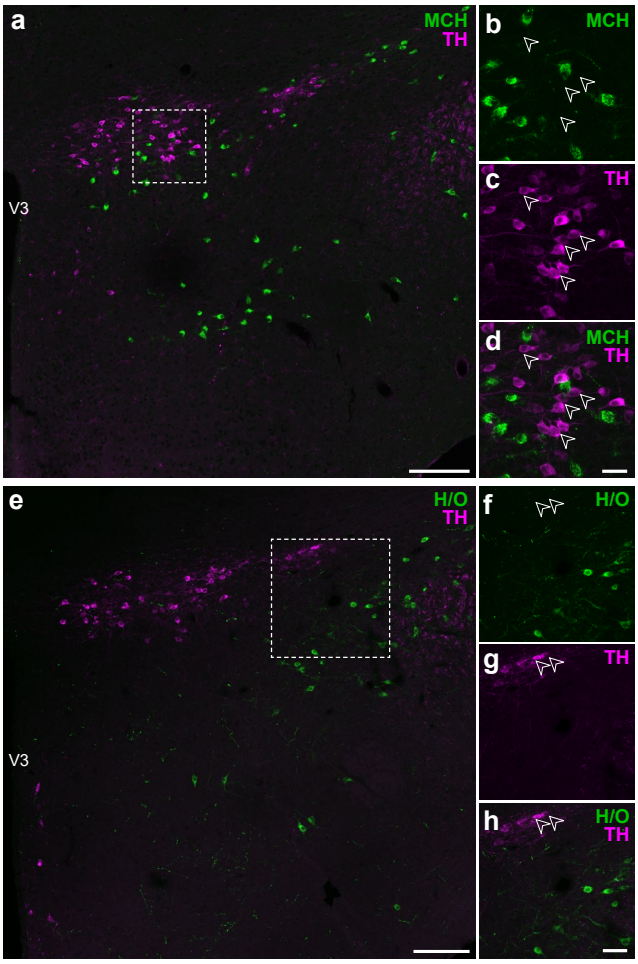

Figure 6. TH-ir neurons in the ZI do not show detectable MCH or H/O immunoreactivities. Confocal photomicrographs from the lateral hypothalamic zone of wild type mouse tissue illustrating the distributions of MCH-ir (***a***–***d***) and H/O-ir neurons (***e***–***h***) relative to TH-ir neurons. Open arrowheads show lack of detectable MCH- (***b***) or H/O-positive labeling (***f***) in TH-ir neurons (***c***, ***g***) in merged-channel, high-magnification photomicrographs (***d***, ***h***) from the outlined areas in ***a*** and ***e***, respectively. Scale bars: 100 µm (***a***, ***e***); 30 µm (***b***–***d***); 50 µm (***f***–***h***).

region contained a few TH-ir neurons in the anteroventral periventricular nucleus (AVPV) and medial preoptic area (MPO). Colocalization of EGFP^{Vgat} at TH-ir neurons in the AVPV was low (13%; **Table 3**; **Figure 5a**) but moderate to high (73–98%) in the MPO (**Table 3**; **Figure 5b**–**e**).

Within the caudal periventricular region, TH-ir neurons were found in the posterior part of the periventricular hypothalamic nucleus (PVp; L75–79), where 72% of them colocalized with EGFP^{Vgat} (**Table 3**; **Figure 5s**–**w**). In the dorsomedial nucleus of the hypothalamus (DMH; **Table 3**), aside from a small cluster of cells lining the dorsomedial tip of its anterior part (DMHa) at L67 (**Figure 5l**), TH-ir neurons were sparsely distributed throughout the remaining DMHa (L68–74), as well as the ventral (DMHv; L71–74), and posterior (DMHp; L70–74) parts of the DMH. TH-ir neurons throughout the entire DMH showed between 80–90% colocalization with EGFP^{Vgat} (**Table 3**).

3.2.3 The hypothalamic medial zone

The hypothalamic medial zone rarely contained TH-ir neurons (**Figure 4j**–**k**), and overall, there was only a weak correlation between EGFP^{Vgat} and TH-ir neurons (r = 0.593,

R2 = 0.352; **Figure 4l**). There were few, if any, TH-ir neurons within the anterior (AHNa) or central (AHNc) parts of the anterior hypothalamic nucleus, but the posterior part (AHNp) contained distinct TH-ir neurons that colocalized with EGFP^{Vgat} (**Table 3**; **Figure 5f**–**k**). A few TH-ir neurons resided more caudally in the supramammillary nucleus (SUM) between L78–L82, but none of these neurons colocalized with EGFP^{Vgat} (**Table 3**; **Figure 5v, w**).

Notably, the PVH, which contained a moderate density of colocalized EGFP^{Vgat} and TH-ir neurons within the periventricular zone, only displayed few such neurons within the hypothalamic medial zone (in its descending division), specifically in the lateral parvicellular part (PVHlp) (L66; **Figure 5k**).

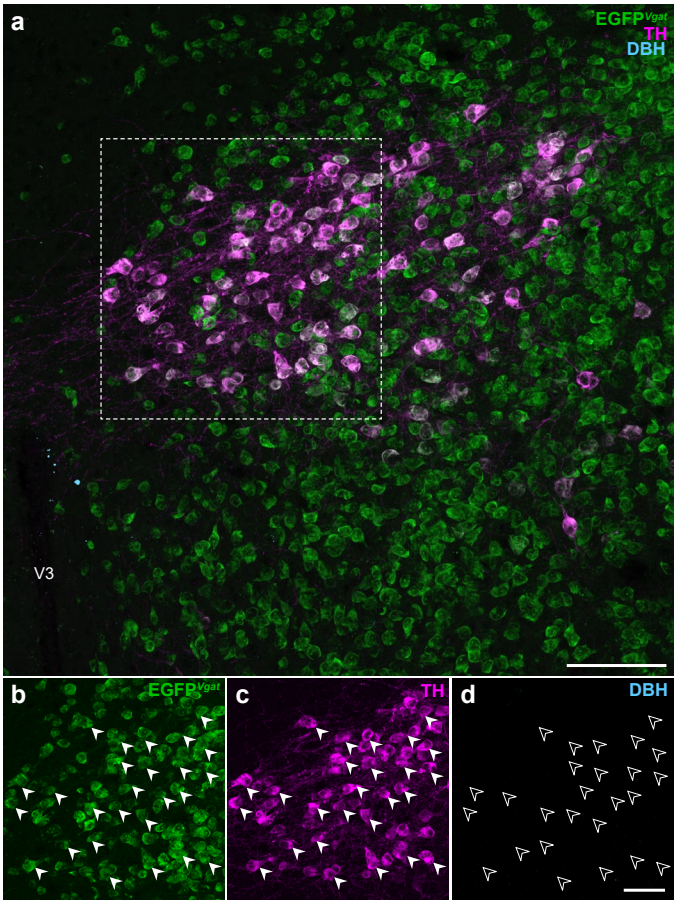

Figure 7. EGFP^{Vgat} TH-ir neurons in the ZI do not express dopamine β-hydroxylase. Confocal photomicrographs from the ZI of *Vgat-cre;L10-Egfp* brain tissue (***a***) show EGFP^{Vgat} (***b***) in TH-ir neurons (***c***) but not immunoreactivity for dopamine β-hydroxylase (DBH; ***d***). Filled arrowheads mark a representative sample of EGFP^{Vgat} TH-ir neurons (***b***, ***c***) from the outlined area (***a***) that do not express DBH, as indicated by open arrowheads (***d***). Scale bars: 100 µm (***a***); 50 µm (***b***–***d***). V3, third ventricle.

3.2.4 The lateral hypothalamic zone

With the exception of the zona incerta (ZI), which accounted for most of the positive lateral hypothalamic zone TH-ir neurons between L66–69, the brain regions in this zone primarily contained a low density of TH-ir neurons (**Figure 4m**), but there was a strong correlation between EGFP^{Vgat} and TH-ir neurons (r = 0.953, R2 = 0.908). In the anterior

region of the lateral hypothalamic zone, the lateral hypothalamic and lateral preoptic areas contained few, if any, TH-ir neurons that colocalized EGFP^{Vgat}. Posterior levels of the hypothalamus (L70–82), which include the posterior hypothalamic nucleus (PH), parasubthalamic nucleus (PSTN), subthalamic nucleus (STN), and tuberal nucleus (TU), contained few TH-ir neurons. These regions displayed low (12–43%) colocalization with EGFP^{Vgat} (**Table 3**).

In contrast, we found a high density of TH-ir neurons in the ZI, particularly within L67–L69 (**Figure 5l–n**), and every TH-ir neuron in this space displayed EGFP^{Vgat} (**Figure 5k–n**). The majority of these TH-ir EGFP^{Vgat} neurons lined the ventral edge of the ZI at L67 and clustered within the medial aspect of the ZI at L68. Interestingly, the majority of these neurons resided outside the cytoarchitectural boundaries of a cell group labeled in *ARA* reference atlas templates (Dong, 2008) as the dopaminergic group within the ZI (ZIda), although those that fell within its boundaries also displayed EGFP^{Vgat} (**Figure 5l–n**).

3.3 Striking distribution pattern of GABAergic TH-ir neurons within the zona incerta

While several hypothalamic regions displayed strong colocalization between TH immunoreactivity and EGFP^{Vgat}, the distribution pattern of neurons with such colocalization was the most prominent and specific within the ZI. The ZI is a relatively expansive region that spans 2.33 mm along the rostrocaudal axis of the mouse brain, as represented within the *ARA* reference space at L61–L83. EGFP^{Vgat} colocalized with all TH-ir ZI neurons found from L67 to L69 (**Figure 5l–n**). The ZI was notable among brain regions because the degree of colocalization of TH-ir neurons with EGFP^{Vgat} was the most complete among all brain regions analyzed at each atlas level (see right- and upper-most data points in **Figure 4**, panels c and o). In contrast, there were very few TH-ir neurons anterior to L67 that were within the cytoarchitectonic boundaries of the ZI (**Figure 5g–k**), only a few TH-ir ZI neurons that were located between L70–L83 (see **Figure 5o–w** for L70–79), and only

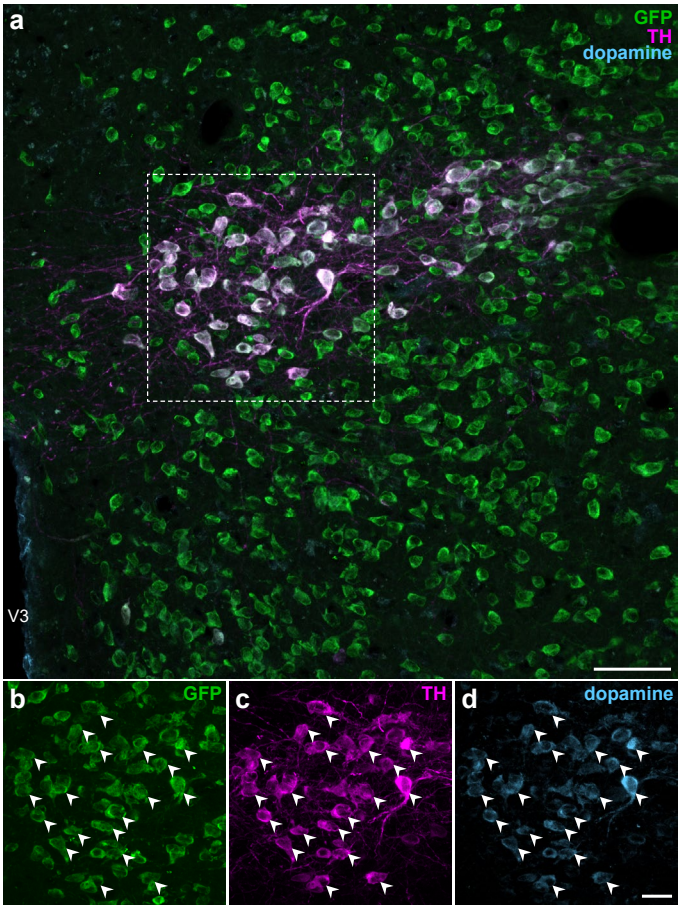

Figure 8. EGFP^{Vgat} TH-ir neurons in the ZI contain immunoreactivity for dopamine. Confocal photomicrographs from the ZI of *Vgat-cre;L10-Egfp* brain tissue (***a***) show the colocalization of GFP (***b***), TH (***c***), and dopamine (***d***) immunoreactivities at high magnification within the same neuron. Filled arrowheads indicate representative GFP-, TH-, and dopamine-ir neurons. Scale bars: 50 µm (***a***); 20 µm (***b***–***d***). V3, third ventricle.

57% of ZI neurons residing outside L67–L69 colocalized with EGFP^{Vgat} (**Table 3**).

3.4 Neurochemical characterization of EGFP^{Vgat} TH-ir neurons

The hypothalamus is enriched by the expression of diverse neuropeptides, including those residing within or surrounding the ZI within the lateral hypothalamic zone, such as MCH and H/O. We performed dual-label IHC reactions for TH and either MCH or H/O, but we could not detect either MCH (**Figure 6a–d**) or H/O (**Figure 6e–h**) immunoreactivity with TH-ir neurons.

TH is the rate-limiting enzyme for all catecholamine neurotransmitter synthesis (Udenfriend & Wyngaarden, 1956) in mammals and is commonly used as a marker of catecholaminergic neurons. However, it does not further specify the terminal catecholamine (i.e., dopamine, norepinephrine, or epinephrine) synthesized by the neuron. Within the catecholamine biosynthesis pathway, dopamine is hydroxylated by dopamine β-hydroxylase (DBH; EC 1.14.17.1) into norepinephrine which, in turn, can be methylated to become epinephrine. Dual-label IHC for DBH and TH immunoreactivities in *Vgat-cre;L10-Egfp* tissue did not reveal DBH-ir neurons within the ZI (**Figure 7**) or any other region of the hypothalamus (data not shown). These results show that TH-ir ZI neurons lack the enzymatic machinery

to synthesize norepinephrine, and hence also epinephrine. Therefore, we determined if TH-ir ZI neurons would display immunoreactivity to dopamine. To this end, we performed triple-label IHC for dopamine, TH, and GFP in the ZI of *Vgat-cre;L10-Egfp* mouse brain tissue and found that almost all GFP- and TH-ir neurons also displayed dopamine immunoreactivity (**Figure 8**).

Discussion

We examined the distribution and neurochemical identity of TH-ir hypothalamic neurons in a transgenic EGFP-reporter mouse line expressing vGAT; portions of these data have been presented in preliminary form (Chee et al. 2017, 2018). First, we found that most hypothalamic TH-ir neurons coexpress vGAT, with the greatest concentration of these neurons located in a portion of the rostral ZI. Second, we found that these rostral ZI coexpressing TH and vGAT display immunoreactivity for dopamine but not for the norepinephrine-synthesizing enzyme DBH. Collectively, the results suggest that rostral ZI neurons synthesize dopamine as their terminal releasable catecholamine and may also release the neurotransmitter GABA. Below, we discuss these results in relation to the known neuroanatomy and neurochemistry of these neurons.

Neuroanatomy. We mapped the locations of TH-ir neurons onto atlas templates from *ARA* (Dong, 2008) to provide high-spatial resolution maps of their distribution throughout the mouse hypothalamus. Several hypothalamic regions, including the arcuate and paraventricular hypothalamic nuclei, contained a high density of $EGFP^{Vgat}$ TH-ir neurons. Notably, the use of a standardized neuroanatomical framework to visualize and map the distribution of TH-ir neurons onto atlas templates revealed their remarkably specific and robust localization in a discrete portion of the ZI. The ZI spans more than 2.3 mm rostrocaudally, but almost all TH-ir neurons were found to reside specifically within a 0.2 mm-long segment of the ZI between L67–L69. Furthermore, these TH-ir neurons appear to be homogeneous in their neurochemical makeup based on their colocalization

of vGAT and dopamine, but not MCH or H/O neuropeptides, or DBH. Together, the evidence in the present study indicates that these neurons likely produce dopamine as their terminal catecholamine in this biosynthetic pathway.

Our Nissl stains in the mouse brain highlight the presence of a compact region within the ZI, which was also labeled ZIda according to *ARA* nomenclature (Dong, 2008), but it is notable that the observed EGFP^{Vgat} TH-ir neurons in our study were medial and ventral to this compact cell group. It has been previously reported that distributions of TH-ir neurons in the ZI may be differentiated by cell diameter (Ruggiero et al., 1984), but we only considered cell location and not cell size in our observations. Commonly used mouse brain atlases (Dong, 2008; Franklin & Paxinos, 2012) make reference to the A13 or dopaminergic cell group of the ZI, respectively, based on cytoarchitectural features. However, given that EGFP^{Vgat} TH-ir neurons in the mouse ZI fall outside of the compact region assigned to these labels, the compact cell group in the mouse ZI may only approximate the location of dopaminergic neurons. It is noteworthy that the most recent iteration of the *ARA* nomenclature and online atlas levels (Allen Institute for Brain Science, 2011a) has removed the cytoarchitectonic boundaries originally assigned in the ZI to the compact A13 region. However, we have used *ARA* digital reference atlas templates (Dong, 2008), which still contain this region as a discrete structure (ZIda), to map our TH-ir neuronal distributions—as these are, at the time of this writing, the only electronically available vector-object templates for *ARA* reference space. As subsequent versions of the *ARA* become available, we hope that accompanying vector-object templates will be available for the community to use to map their datasets.

Neurochemistry. Although TH immunoreactivity is a useful marker for dopaminergic cell populations, its presence alone is not sufficient to identify these populations, but needs to be considered in relation to the presence or absence of other molecular markers of dopaminergic transmission and/or the specific catecholamine produced by the neurons being examined (A. Björklund & Dunnett, 2007; Tritsch, Granger, & Sabatini, 2016). In the

hypothalamus, transcriptomic analysis of neurons in the lateral hypothalamic area has provided evidence in support of the GABAergic and dopaminergic profile of TH neurons, which express genes encoding enzymes to synthesize GABA (*Gad1* and *Gad2*) and dopamine (*Ddc* and *Th*), as well as their respective vesicular transporters vGAT (*Slc32al*) and vMAT2 (*Slc18a2*) (Mickelsen et al., 2019). ZI TH-ir neurons may transport dopamine into synaptic vesicles, as they also express the vesicular monoamine transporter, vMAT2 (Sharma, Kim, Mayr, Elliott, & Whelan, 2018). Moreover, microspectrofluorometric studies have demonstrated that catecholaminergic ZI neurons in the rat display emission spectra exclusively for dopamine (A Björklund & Nobin, 1973), and our own detection of dopamine immunoreactivity in these neurons supports this observation. Taken together, the presence of TH, dopamine, and vMAT2 in these ZI neurons suggests that these neurons package and release dopamine for neurotransmission. The detection of TH and dopamine immunoreactivity also suggests that these neurons probably express aromatic L-amino acid decarboxylase (AADC; EC 4.1.1.28) (Lovenberg, Weissbach, & Udenfriend, 1962), which has been shown in ZI neurons of the prairie vole (Ahmed, Northcutt, & Lonstein, 2012), and that both AADC and TH are catalytically active for dopamine synthesis.

Similarly, ZI TH-ir neurons also express glutamate decarboxylase (GAD) to synthesize GABA (Shin et al., 2007) and we show in the present study that all ZI TH-ir neurons express vGAT, which facilitates the transport of GABA into synaptic vesicles (**Figures 7, 8**). Collectively, these observations show that in addition to dopaminergic neurotransmission, ZI TH-ir neurons also possess the molecular machinery to mediate GABAergic neurotransmission. By contrast, we did not detect the colocalization of TH and $EGFP^{Vglut2}$ in the ZI or elsewhere in the hypothalamus, and while it is possible that hypothalamic TH-ir neurons may harbor an alternative transporter for glutamate, such as Vglut3 (Schäfer, Varoqui, Defamie, Weihe, & Erickson, 2002), the expression of Vglut1 in the hypothalamus has not been reported (Fremeau et al., 2001).

We also did not detect the colocalization of ZI TH-ir neurons with at least two major

neuropeptidergic cell groups in the lateral hypothalamic zone. Unlike ZI TH-ir neurons, both MCH and H/O neurons coexpress *Vglut2* but not *Vgat* (Mickelsen et al., 2019) and can release glutamate (Chee et al., 2015; Schöne et al., 2012). In light of recent transcriptomic analysis, we also do not expect that ZI TH neurons would colocalize with another neuropeptide, as they do not show enriched gene expression for neuropeptides such as cocaine- and amphetamine-regulated transcript protein, galanin, neuropeptide W, neuropeptide Y, neurotensin, somatostatin, and tachykinin produced by *Vgat*-expressing neurons in the lateral hypothalamus (Mickelsen et al., 2019).

We identified GABAergic neurons based on vGAT expression, which we visualized by cre-dependent EGFP expression in *Vgat-cre;L10-Egfp* neurons. As gross, qualitative comparison of *Vgat* hybridization signals had shown its expression in expected brain regions (Vong et al., 2011), we performed quantitative analyses to address any possible ectopic EGFP expression at the neuronal level. Nearly all (>99%) EGFP^{Vgat} neurons expressed *Vgat* mRNA, thus confirming robust and accurate labeling of vGAT neurons in the hypothalamus of *Vgat-cre;L10-Egfp* mice. Furthermore, fewer than 1% of *Vgat* neurons do not express EGFP^{Vgat}, so it is unlikely that there would be a cluster of detectable TH-ir *Vgat* neurons that is not revealed by colocalization with EGFP^{Vgat}. GABA is often reported as a co-transmitter in dopaminergic cells. For example, dopaminergic neurons in the ventral tegmental area may transport GABA and dopamine via vMAT2, thus these two chemical messengers may be co-packaged (Tritsch, Ding, & Sabatini, 2012). However, in the olfactory bulb, GABA and dopamine are not necessarily co-packaged, and they may utilize independent modes of vesicular release that occur over different time courses (Borisovska, Bensen, Chong, & Westbrook, 2013). We are pursuing further neuroanatomical studies to identify the projection targets of ZI TH-ir neurons (Mejia et al., 2019), as well as functional studies to determine if these ostensibly GABAergic and dopaminergic ZI neurons do in fact release GABA and/or dopamine at downstream neurons.

GABAergic neurons within the ZI have recently been shown to modulate the motivational and hedonic aspects of feeding through direct projections to the paraventricular nucleus of the thalamus (PVT) (Zhang & van den Pol, 2017), but it is not known if dopamine also acts at the PVT to stimulate feeding. The PVT receives projections from ZI TH neurons (Li, Shi, & Kirouac, 2014) and expresses D2-subtype dopamine receptors, which are linked to a role for the PVT in drug addiction (Clark et al., 2017). There is at least a foundational basis for dopamine- and GABA-mediated neurotransmission in the PVT, but it remains to be determined if these chemical messengers would exert similar influences upon behavior by acting in the PVT or elsewhere. For instance, another ZI GABAergic pathway targets the periaqueductal gray (PAG) and is implicated in the control of flight and freezing responses (Chou et al., 2018). A neuroanatomical tracing study reported ZI TH-ir neuronal projections to the PAG in rats (Messanvi, Eggens-Meijer, Roozendaal, & van der Want, 2013) allowing for the possibility of a role for dopamine in mediating defensive behaviors.

Our work broadly supports the emerging view that GABA co-transmission is a hallmark of dopaminergic neurons (Tritsch et al., 2016). Overall, we found EGFP^{Vgat} signals colocalized in 82% of hypothalamic TH-ir neurons, though some regions showed higher or lower levels of colocalization (**Table 3**). Outside the ZI, the largest numbers of EGFP^{Vgat} TH-ir neurons were distributed through the PVH, PV, and ARH, regions which harbor neurons that project to the pituitary (Ju, Liu, & Tao, 1986) and mediate neurosecretory functions (Markakis & Swanson, 1997). For example, TH-expressing neurons send projections to the median eminence to enable dopamine-mediated inhibition of prolactin release from the anterior pituitary gland (Ben-Jonathan & Hnasko, 2001; Ben-Jonathan, Oliver, Weiner, Mical, & Porter, 1977). Moreover, cells in the anterior pituitary express all GABA receptor subtypes (Anderson & Mitchell, 1986) and GABA administration can also inhibit prolactin release (Grandison & Guidotti, 1979). Thus, in addition to mediating local neurocircuitry to regulate behavior, colocalized GABA and dopamine in neurons could

work synergistically to mediate neuroendocrine functions.

Hypothalamic TH-ir neurons in the rat and mouse have been reported since the 1970s (Hökfelt et al., 1976; Hökfelt et al., 1984; Ruggiero et al., 1984; van den Pol et al., 1984), and the present study extends this work by providing high spatial-resolution atlas-based maps of TH-ir neurons in the mouse hypothalamus. Further, this dataset is enriched by defining and mapping the distribution of TH neuron subpopulations that may also be GABAergic. Importantly, these maps constitute a standardized dataset that can be used to derive precise stereotaxic coordinates to target these discrete neuronal subpopulations in functional studies.

References

Agostinelli, L. J., Ferrari, L. L., Mahoney, C. E., Mochizuki, T., Lowell, B. B., Arrigoni, E., & Scammell, T. E. (2017). Descending projections from the basal forebrain to the orexin neurons in mice. *J Comp Neurol, 525*(7), 1668-1684. https://doi.org/10.1002/cne.24158

Ahmed, E. I., Northcutt, K. V., & Lonstein, J. S. (2012). L-amino acid decarboxylase- and tyrosine hydroxylase-immunoreactive cells in the extended olfactory amygdala and elsewhere in the adult prairie vole brain. *J Chem Neuroanat, 43*(1), 76-85. https://doi.org/10.1016/j.jchemneu.2011.10.006

Allen Institute for Brain Science. (2011a). *Allen Mouse Brain Atlas*. Retrieved from http://atlas.brain-map.org/

Allen Institute for Brain Science. (2011b). *Technical white paper: Allen reference atlas*, version 1 (2008) (PDF file). from Allen Institute for Brain Science http://help.brain-map.org/display/mousebrain/Documentation

Anderson, R. A., & Mitchell, R. (1986). Effects of gamma-aminobutyric acid receptor agonists on the secretion of growth hormone, luteinizing hormone, adrenocorticotrophic hormone and thyroid-stimulating hormone from the rat pituitary gland in vitro. *J*

Endocrinol, 108(1), 1-8. https://doi.org/10.1677/joe.0.1080001

Ben-Jonathan, N., & Hnasko, R. (2001). Dopamine as a prolactin (PRL) inhibitor. *Endocr Rev, 22*(6), 724-763. https://doi.org/10.1210/edrv.22.6.0451

Ben-Jonathan, N., Oliver, C., Weiner, H. J., Mical, R. S., & Porter, J. C. (1977). Dopamine in hypophysial portal plasma of the rat during the estrous cycle and throughout pregnancy. *Endocrinology, 100*(2), 452-458. https://doi.org/10.1210/endo-100-2-452

Björklund, A., & Dunnett, S. B. (2007). Dopamine neuron systems in the brain: an update. *Trends Neurosci, 30*(5), 194-202. https://doi.org/10.1016/j.tins.2007.03.006

Björklund, A., & Lindvall, O. (1984). Dopamine-containing systems in the CNS. In A. Björklund & T. Hökfelt (Eds.), *Handbook of Chemical Neuroanatomy*, Volume 2: Classical Transmitters in the CNS, Part I (pp. 55-122). Amsterdam: Elsevier.

Björklund, A., & Nobin, A. (1973). Fluorescence histochemical and microspectrofluorometric mapping of dopamine and noradrenaline cell groups in the rat diencephalon. *Brain Res, 51*, 193-205. https://doi.org/10.1016/0006-8993(73)90372-7

Borisovska, M., Bensen, A. L., Chong, G., & Westbrook, G. L. (2013). Distinct modes of dopamine and GABA release in a dual transmitter neuron. *J Neurosci, 33*(5), 1790-1796. https://doi.org/10.1523/jneurosci.4342-12.2013

Bota, M., & Swanson, L. W. (2007). The neuron classification problem. *Brain Res Rev, 56*(1), 79-88. https://doi.org/10.1016/j.brainresrev.2007.05.005

Bourdy, R., Sánchez-Catalán, M.-J., Kaufling, J., Balcita-Pedicino, J. J., Freund-Mercier, M.-J., Veinante, P., . . . Barrot, M. (2014). Control of the Nigrostriatal Dopamine Neuron Activity and Motor Function by the Tail of the Ventral Tegmental Area. *Neuropsychopharmacology, 39*(12), 2788. https://doi.org/10.1038/npp.2014.129

Broberger, C., de Lecea, L., Sutcliffe, J. G., & Hökfelt, T. (1998). Hypocretin/orexin- and melanin-concentrating hormone-expressing cells form distinct populations in the rodent lateral hypothalamus: relationship to the neuropeptide Y and agouti gene-

related protein systems. *J Comp Neurol, 402*(4), 460-474. https://doi.org/10.1002/(SICI)1096-9861(19981228)402:4%3C460::AID-CNE3%3E3.0.CO;2-S

Broberger, C., Johansen, J., Johansson, C., Schalling, M., & Hökfelt, T. (1998). The neuropeptide Y/agouti gene-related protein (AGRP) brain circuitry in normal, anorectic, and monosodium glutamate-treated mice. *Proc Natl Acad Sci U S A, 95*(25), 15043-15048. https://doi.org/10.1073/pnas.95.25.15043

Busch, S., Selcho, M., Ito, K., & Tanimoto, H. (2009). A map of octopaminergic neurons in the Drosophila brain. *J Comp Neurol, 513*(6), 643-667. https://doi.org/10.1002/cne.21966

Carrera, I., Anadón, R., & Rodríguez-Moldes, I. (2012). Development of tyrosine hydroxylase-immunoreactive cell populations and fiber pathways in the brain of the dogfish Scyliorhinus canicula: new perspectives on the evolution of the vertebrate catecholaminergic system. *J Comp Neurol, 520*(16), 3574-3603. https://doi.org/10.1002/cne.23114

Chee, M. J., Arrigoni, E., & Maratos-Flier, E. (2015). Melanin-concentrating hormone neurons release glutamate for feedforward inhibition of the lateral septum. *J Neurosci, 35*(8), 3644-3651. https://doi.org/10.1523/jneurosci.4187-14.2015

Chee, M. J., Negishi, K., Schumacker, K. S., Butler, R. B., & Khan, A. M. (2017). Immunohistochemical study and atlas mapping of neuronal populations that co-express tyrosine hydroxylase and the vesicular GABA transporter in the hypothalamus. Program 604.04. Poster presented at the Society for Neuroscience, Washington, DC.

Chee, M. J., Negishi, K., Schumacker, K. S., Butler, R. B., & Khan, A. M. (2018). Identification and atlas mapping of mouse hypothalamic neurons that co-express tyrosine hydroxylase and the vesicular GABA transporter in in situ hybridization and immunohistochemistry studies. Program No. 680.27. Poster presented at the Society for Neuroscience, San Diego, CA.

Chee, M. J., Pissios, P., & Maratos-Flier, E. (2013). Neurochemical characterization of neurons expressing melanin-concentrating hormone receptor 1 in the mouse hypothalamus. *J Comp Neurol, 521*(10), 2208-2234. https://doi.org/10.1002/cne.23273

Chou, X. L., Wang, X., Zhang, Z. G., Shen, L., Zingg, B., Huang, J., . . . Tao, H. W. (2018). Inhibitory gain modulation of defense behaviors by zona incerta. *Nat Commun, 9*(1), 1151. https://doi.org/10.1038/s41467-018-03581-6

Chung, E. K. Y., Chen, L. W., Chan, Y. S., & Yung, K. K. L. (2008). Downregulation of glial glutamate transporters after dopamine denervation in the striatum of 6-hydroxydopamine-lesioned rats. *J Comp Neurol, 511*(4), 421-437. https://doi.org/10.1002/cne.21852

Clark, A. M., Leroy, F., Martyniuk, K. M., Feng, W., McManus, E., Bailey, M. R., . . . Kellendonk, C. (2017). Dopamine D2 receptors in the paraventricular thalamus attenuate cocaine locomotor sensitization. *eNeuro, 4*(5). https://doi.org/10.1523/eneuro.0227-17.2017

Crosetto, N., Bienko, M., & van Oudenaarden, A. (2015). Spatially resolved transcriptomics and beyond. *Nat Rev Genet, 16*(1), 57-66. https://doi.org/10.1038/nrg3832

Dahlström, A., & Fuxe, K. (1964). Evidence for the existence of monoamine-containing neurons in the central nervous system. I. Demonstration of monoamines in the cell bodies of brain stem neurons. *Acta Physiol Scand Suppl, Suppl 232*, 1-55.

Dong, H. W. (2008). *The Allen reference atlas: A digital color brain atlas of the C57BL/6J male mouse*. Hoboken, NJ: John Wiley & Sons.

Elias, C. F., Saper, C. B., Maratos-Flier, E., Tritos, N. A., Lee, C., Kelly, J., . . . Elmquist, J. K. (1998). Chemically defined projections linking the mediobasal hypothalamus and the lateral hypothalamic area. *J Comp Neurol, 402*(4), 442-459. https://doi.org/10.1002/(SICI)1096-9861(19981228)402:4%3C442::AID-CNE2%3E3.0.CO;2-R

Everitt, B. J., Meister, B., Hökfelt, T., Melander, T., Terenius, L., Rokaeus, A., . . . et

al. (1986). The hypothalamic arcuate nucleus-median eminence complex: immunohistochemistry of transmitters, peptides and DARPP-32 with special reference to coexistence in dopamine neurons. *Brain Res, 396*(2), 97-155. https://doi.org/10.1016/s0006-8993(86)80192-5

Florenzano, F., Viscomi, M. T., Mercaldo, V., Longone, P., Bernardi, G., Bagni, C., . . . Carrive, P. (2006). P2X2R purinergic receptor subunit mRNA and protein are expressed by all hypothalamic hypocretin/orexin neurons. *J Comp Neurol, 498*(1), 58-67. https://doi.org/10.1002/cne.21013

Franklin, K. B., & Paxinos, G. (2012). *The mouse brain in stereotaxic coordinates* (4th ed.). New York, NY: Academic Press.

Fremeau, R. T., Jr., Troyer, M. D., Pahner, I., Nygaard, G. O., Tran, C. H., Reimer, R. J., . . . Edwards, R. H. (2001). The expression of vesicular glutamate transporters defines two classes of excitatory synapse. *Neuron, 31*(2), 247-260. https://doi.org/10.1016/s0896-6273(01)00344-0

Grandison, L., & Guidotti, A. (1979). gamma-Aminobutyric acid receptor function in rat anterior pituitary: evidence for control of prolactin release. *Endocrinology, 105*(3), 754-759. https://doi.org/10.1210/endo-105-3-754

Hahn, T. M., Breininger, J. F., Baskin, D. G., & Schwartz, M. W. (1998). Coexpression of Agrp and NPY in fasting-activated hypothalamic neurons. *Nat Neurosci, 1*(4), 271-272. https://doi.org/10.1038/1082

Halliday, G. M., & McLachlan, E. M. (1991). A comparative analysis of neurons containing catecholamine-synthesizing enzymes and neuropeptide Y in the ventrolateral medulla of rats, guinea-pigs and cats. *Neuroscience, 43*(2-3), 531-550. https://doi.org/10.1016/0306-4522(91)90313-d

Hökfelt, T., Holets, V. R., Staines, W., Meister, B., Melander, T., Schalling, M., . . . et al. (1986). Coexistence of neuronal messengers--an overview. *Prog Brain Res, 68*, 33-70. https://doi.org/10.1016/s0079-6123(08)60230-7

Hökfelt, T., Johansson, O., Fuxe, K., Goldstein, M., & Park, D. (1976). Immunohistochemical studies on the localization and distribution of monoamine neuron systems in the rat brain. I. Tyrosine hydroxylase in the mes- and diencephalon. *Med Biol, 54*(6), 427-453.

Hökfelt, T., Märtensson, R., Björklund, A., Kleinau, S., & Goldstein, M. (1984). Distributional maps of tyrosine hydroxylase-immunoreactive neurons in the rat brain. In A. Björklund & T. Hökfelt (Eds.), *Handbook of Chemical Neuroanatomy*, vol. 2. Classical Transmitters in the CNS, Part I. (pp. 277-379). Amsterdam: Elsevier.

Ju, G., Liu, S., & Tao, J. (1986). Projections from the hypothalamus and its adjacent areas to the posterior pituitary in the rat. *Neuroscience, 19*(3), 803-828. https://doi.org/10.1016/0306-4522(86)90300-3

Khan, A. M., Grant, A. H., Martinez, A., Burns, G., Thatcher, B. S., Anekonda, V. T., . . . Blevins, J. E. (2018). Mapping molecular datasets back to the brain regions they are extracted from: Remembering the native countries of hypothalamic expatriates and refugees. *Adv Neurobiol, 21*, 101-193. https://doi.org/10.1007/978-3-319-94593-4_6

Kiernan, J. A. (2001). Classification and naming of dyes, stains and fluorochromes. *Biotechnic & Histochemistry, 76*(5-6), 261-278.https://doi.org/10.1080/bih.76.5-6.261.278

Krashes, M. J., Shah, B. P., Madara, J. C., Olson, D. P., Strochlic, D. E., Garfield, A. S., . . . Lowell, B. B. (2014). An excitatory paraventricular nucleus to AgRP neuron circuit that drives hunger. *Nature, 507*(7491), 238-242. https://doi.org/10.1038/nature12956

Kuscha, V., Barreiro-Iglesias, A., Becker, C. G., & Becker, T. (2012). Plasticity of tyrosine hydroxylase and serotonergic systems in the regenerating spinal cord of adult zebrafish. *J Comp Neurol, 520*(5), 933-951. https://doi.org/10.1002/cne.22739

Lenhossék, M. (1895). *Der feinere Bau des Nervensystems im Lichte neuester*

Forschungen (2nd ed.). Berlin: H. Kornfeld.

Li, S., Shi, Y., & Kirouac, G. J. (2014). The hypothalamus and periaqueductal gray are the sources of dopamine fibers in the paraventricular nucleus of the thalamus in the rat. *Front Neuroanat, 8*, 136. https://doi.org/10.3389/fnana.2014.00136

Lovenberg, W., Weissbach, H., & Udenfriend, S. (1962). Aromatic L-amino acid decarboxylase. *J Biol Chem, 237*, 89-93.

Markakis, E. A., & Swanson, L. W. (1997). Spatiotemporal patterns of secretomotor neuron generation in the parvicellular neuroendocrine system. *Brain Res Brain Res Rev, 24*(2-3), 255-291. https://doi.org/10.1016/s0165-0173(97)00006-4

Mejia, E., Ponce, M. S., Negishi, K., Hebert, A. J., Chee, M. J., & Khan, A. M. (2019). Viral tracing of axonal projections from tyrosine hydroxylase-expressing neurons of the zona incerta in male mice. Program No. 149.21. Poster presented at the Society for Neuroscience, Chicago, IL.

Messanvi, F., Eggens-Meijer, E., Roozendaal, B., & van der Want, J. J. (2013). A discrete dopaminergic projection from the incertohypothalamic A13 cell group to the dorsolateral periaqueductal gray in rat. *Front Neuroanat, 7*, 41. https://doi.org/10.3389/fnana.2013.00041

Mickelsen, L. E., Bolisetty, M., Chimileski, B. R., Fujita, A., Beltrami, E. J., Costanzo, J. T., . . . Jackson, A. C. (2019). Single-cell transcriptomic analysis of the lateral hypothalamic area reveals molecularly distinct populations of inhibitory and excitatory neurons. *Nat Neurosci, 22*(4), 642-656. https://doi.org/10.1038/s41593-019-0349-8

Mickelsen, L. E., Kolling, F. W., Chimileski, B. R., Fujita, A., Norris, C., Chen, K., . . . Jackson, A. C. (2017). Neurochemical heterogeneity among lateral hypothalamic hypocretin/orexin and melanin-concentrating hormone neurons identified through single-cell gene expression analysis. *eNeuro, 4*(5). https://doi.org/10.1523/eneuro.0013-17.2017

Naganuma, F., Bandaru, S. S., Absi, G., Chee, M. J., & Vetrivelan, R. (2019). Melanin-concentrating hormone neurons promote rapid eye movement sleep independent of glutamate release. *Brain Struct Funct, 224*(1), 99-110. https://doi.org/10.1007/s00429-018-1766-2

Nagatsu, T., Levitt, M., & Udenfriend, S. (1964). Conversion of L-tyrosine to 3,4-dihydroxyphenylalanine by cell-free preparations of brain and sympathetically innervated tissues. *Biochem Biophys Res Commun, 14*, 543-549. https://doi.org/10.1016/0006-291x(64)90266-9

Romanov, R. A., Zeisel, A., Bakker, J., Girach, F., Hellysaz, A., Tomer, R., . . . Harkany, T. (2017). Molecular interrogation of hypothalamic organization reveals distinct dopamine neuronal subtypes. *Nat Neurosci, 20*(2), 176-188. https://doi.org/10.1038/nn.4462

Ruggiero, D. A., Baker, H., Joh, T. H., & Reis, D. J. (1984). Distribution of catecholamine neurons in the hypothalamus and preoptic region of mouse. *J Comp Neurol, 223*(4), 556-582. https://doi.org/10.1002/cne.902230408

Schäfer, M. K., Varoqui, H., Defamie, N., Weihe, E., & Erickson, J. D. (2002). Molecular cloning and functional identification of mouse vesicular glutamate transporter 3 and its expression in subsets of novel excitatory neurons. *J Biol Chem, 277*(52), 50734-50748. https://doi.org/10.1074/jbc.m206738200

Schneeberger, M., Tan, K., Nectow, A. R., Parolari, L., Caglar, C., Azevedo, E., . . . Friedman, J. M. (2018). Functional analysis reveals differential effects of glutamate and MCH neuropeptide in MCH neurons. *Mol Metab, 13*, 83-89. https://doi.org/10.1016/j.molmet.2018.05.001

Schöne, C., Apergis-Schoute, J., Sakurai, T., Adamantidis, A., & Burdakov, D. (2014). Coreleased orexin and glutamate evoke nonredundant spike outputs and computations in histamine neurons. *Cell Rep, 7*(3), 697-704. https://doi.org/10.1016/j.celrep.2014.03.055

Schöne, C., Cao, Z. F., Apergis-Schoute, J., Adamantidis, A., Sakurai, T., & Burdakov, D. (2012). Optogenetic probing of fast glutamatergic transmission from hypocretin/orexin to histamine neurons in situ. *J Neurosci, 32*(36), 12437-12443. https://doi.org/10.1523/jneurosci.0706-12.2012

Sears, R. M., Liu, R. J., Narayanan, N. S., Sharf, R., Yeckel, M. F., Laubach, M., . . . DiLeone, R. J. (2010). Regulation of nucleus accumbens activity by the hypothalamic neuropeptide melanin-concentrating hormone. *J Neurosci, 30*(24), 8263-8273. https://doi.org/10.1523/jneurosci.5858-09.2010

Sharma, S., Kim, L. H., Mayr, K. A., Elliott, D. A., & Whelan, P. J. (2018). Parallel descending dopaminergic connectivity of A13 cells to the brainstem locomotor centers. *Sci Rep, 8*(1), 7972. https://doi.org/10.1038/s41598-018-25908-5

Shepard, J. D., Chuang, D. T., Shaham, Y., & Morales, M. (2006). Effect of methamphetamine self-administration on tyrosine hydroxylase and dopamine transporter levels in mesolimbic and nigrostriatal dopamine pathways of the rat. *Psychopharmacology (Berl), 185*(4), 505-513. https://doi.org/10.1007/s00213-006-0316-4

Shin, S. Y., Yang, J. H., Lee, H., Erdelyi, F., Szabo, G., Lee, S. Y., & Ryu, P. D. (2007). Identification of the adrenoceptor subtypes expressed on GABAergic neurons in the anterior hypothalamic area and rostral zona incerta of GAD65-eGFP transgenic mice. *Neurosci Lett, 422*(3), 153-157. https://doi.org/10.1016/j.neulet.2007.05.060

Sockman, K. W., & Salvante, K. G. (2008). The integration of song environment by catecholaminergic systems innervating the auditory telencephalon of adult female European starlings. *Dev Neurobiol, 68*(5), 656-668. https://doi.org/10.1002/dneu.20611

Steinbusch, H. W. M., van Vliet, S. P., Bol, J., G. J. M., & de Vente, J. (1991). Development and application of antibodies to primary (DA, L-DOPA) and secondary (cGMP) messengers: A technical report. In A. Calas & D. Eugène (Eds.), *Neurocytochemical Methods*. NATO ASI Series (Series H: Cell Biology) (Vol. 58, pp. 1-27). Berlin:

Springer-Verlag.

Swanson, L. W. (2018). Brain maps 4.0-Structure of the rat brain: An open access atlas with global nervous system nomenclature ontology and flatmaps. *J Comp Neurol, 526*(6), 935-943. https://doi.org/10.1002/cne.24381

Tong, Q., Ye, C. P., Jones, J. E., Elmquist, J. K., & Lowell, B. B. (2008). Synaptic release of GABA by AgRP neurons is required for normal regulation of energy balance. *Nat Neurosci, 11*(9), 998-1000. https://doi.org/10.1038/nn.2167

Tritsch, N. X., Ding, J. B., & Sabatini, B. L. (2012). Dopaminergic neurons inhibit striatal output through non-canonical release of GABA. *Nature, 490*(7419), 262-266. https://doi.org/10.1038/nature11466

Tritsch, N. X., Granger, A. J., & Sabatini, B. L. (2016). Mechanisms and functions of GABA co-release. *Nat Rev Neurosci, 17*(3), 139-145. https://doi.org/10.1038/nrn.2015.21

Udenfriend, S., & Wyngaarden, J. B. (1956). Precursors of adrenal epinephrine and norepinephrine in vivo. *Biochim Biophys Acta, 20*(1), 48-52. https://doi.org/10.1016/0006-3002(56)90261-x

van den Pol, A. N. (2012). Neuropeptide transmission in brain circuits. *Neuron, 76*(1), 98-115. https://doi.org/10.1016/j.neuron.2012.09.014

van den Pol, A. N., Herbst, R. S., & Powell, J. F. (1984). Tyrosine hydroxylase-immunoreactive neurons of the hypothalamus: a light and electron microscopic study. *Neuroscience, 13*(4), 1117-1156. https://doi.org/10.1016/0306-4522(84)90292-6

Vazdarjanova, A., Ramirez-Amaya, V., Insel, N., Plummer, T. K., Rosi, S., Chowdhury, S., . . . Barnes, C. A. (2006). Spatial exploration induces ARC, a plasticity-related immediate-early gene, only in calcium/calmodulin-dependent protein kinase II-positive principal excitatory and inhibitory neurons of the rat forebrain. *J Comp Neurol, 498*(3), 317-329. https://doi.org/10.1002/cne.21003

Vong, L., Ye, C., Yang, Z., Choi, B., Chua, S., & Lowell, B. B. (2011). Leptin action on GABAergic neurons prevents obesity and reduces inhibitory tone to POMC

neurons. *Neuron, 71*(1), 142-154. https://doi.org/10.1016/j.neuron.2011.05.028

Wittmann, G., Hrabovszky, E., & Lechan, R. M. (2013). Distinct glutamatergic and GABAergic subsets of hypothalamic pro-opiomelanocortin neurons revealed by in situ hybridization in male rats and mice. *J Comp Neurol, 521*(14), 3287-3302. https://doi.org/10.1002/cne.23350

Wolf, M. E., & Kapatos, G. (1989). Flow cytometric analysis and isolation of permeabilized dopamine nerve terminals from rat striatum. *J Neurosci, 9*(1), 106-114. https://doi.org/10.1523/jneurosci.09-01-00106.1989

Wu, M., Dumalska, I., Morozova, E., van den Pol, A., & Alreja, M. (2009). Melanin-concentrating hormone directly inhibits GnRH neurons and blocks kisspeptin activation, linking energy balance to reproduction. *Proc Natl Acad Sci U S A, 106*(40), 17217-17222. https://doi.org/10.1073/pnas.0908200106

Yamaguchi, H., Hopf, F. W., Li, S. B., & de Lecea, L. (2018). In vivo cell type-specific CRISPR knockdown of dopamine beta hydroxylase reduces locus coeruleus evoked wakefulness. *Nat Commun, 9*(1), 5211. https://doi.org/10.1038/s41467-018-07566-3

Zhang, X., & van den Pol, A. N. (2015). Dopamine/tyrosine hydroxylase neurons of the hypothalamic arcuate nucleus release GABA, communicate with dopaminergic and other arcuate neurons, and respond to dynorphin, Met-enkephalin, and oxytocin. *J Neurosci, 35*(45), 14966-14982. https://doi.org/10.1523/jneurosci.0293-15.2015

Zhang, X., & van den Pol, A. N. (2016). Hypothalamic arcuate nucleus tyrosine hydroxylase neurons play orexigenic role in energy homeostasis. *Nat Neurosci, 19*(10), 1341-1347. https://doi.org/10.1038/nn.4372

Zhang, X., & van den Pol, A. N. (2017). Rapid binge-like eating and body weight gain driven by zona incerta GABA neuron activation. *Science, 356*(6340), 853-859. https://doi.org/10.1126/science.aam7100

Zséli, G., Vida, B., Martinez, A., Lechan, R. M., Khan, A. M., & Fekete, C. (2016).

Elucidation of the anatomy of a satiety network: Focus on connectivity of the parabrachial nucleus in the adult rat. *J Comp Neurol, 524*(14), 2803-2827. https://doi.org/10.1002/cne.23992

Table 1. List and details of primary antibodies

Antibody	Immunogen	Clonality, Isotype	Source, Catalogue no., Lot no.	RRID	Titer
Sheep anti-DIG	Isolated from sheep immunized with DIG steroid molecule	Polyclonal, IgG	Roche, 11207733910, 28557000	AB_514500	1:100
Goat anti-dopamine	Dopamine-glutaraldehyde-thyroglobulin conjugate	Polyclonal, IgG	Dr. H. W. M. Steinbusch, Maastricht University	N/A	1:2,000
Rabbit anti-DBH	Purified enzyme from bovine adrenal medulla	Polyclonal, IgG	Immunostar, 22806, 1233001	AB_572229	1:5,000
Chicken anti-GFP	His-tagged GFP isolated from *Aequorea victoria*	Polyclonal, IgY	Millipore, 06-896, 3022861	AB_11214044	1:2,000
Rabbit anti-GFP	Isolated from *Aequorea victoria*	Polyclonal, IgG	Invitrogen, A6455, 52630A	AB_221570	1:1,000
Rabbit anti-MCH	Full length MCH peptide	Polyclonal, IgG	Dr. E. Maratos-Flier, Beth Israel Deaconess Medical Center	AB_2314774	1:5,000
Goat anti-orexin-A	Amino acid residue 48–66 at C-terminus of human orexin precursor	Polyclonal, IgG	Santa Cruz, sc-8070, J2414	AB_653610	1:4,000
Mouse anti-TH	Purified from N-terminus of PC12 cells	Monoclonal, IgG	Millipore, MAB318, 2677893	AB_2201528	1:2,000

DIG, digoxigenin; DBH, dopamine beta-hydroxylase; GFP, green fluorescent protein; MCH, melanin-concentrating hormone; TH, tyrosine hydroxylase

Table 2. List and details of secondary antibodies

Antibody	Isotype	Source, Catalogue no., Lot no.	RRID	Titer
AffiniPure donkey anti-chicken Alexa Fluor 488	IgY (H+L)	Jackson ImmunoResearch, 703-545-155, 139424	AB_2340375	1:500
AffiniPure donkey anti-goat Alexa Fluor 488	IgG (H+L)	Jackson ImmunoResearch, 705-545-147, 103943	AB_2336933	1:500
AffiniPure donkey anti-rabbit Alexa Fluor 488	IgG (H+L)	Jackson ImmunoResearch, 711-545-152, 125719	AB_2313584	1:200
Donkey anti-rabbit Alexa Fluor 488	IgG (H+L)	Thermo Fisher Scientific, A-21206, 19107512	AB_141708	1:500
Donkey anti-mouse Alexa Fluor 568	IgG (H+L)	Thermo Fisher Scientific, A-10037, 1827879	AB_2534013	1:500
Donkey anti-goat Alexa Fluor 647	IgG (H+L)	Thermo Fisher Scientific, A-21447, 1977345	AB_2535864	1:500
Donkey anti-rabbit Alexa Fluor 647	IgG (H+L)	Thermo Fisher Scientific, A-31573, 1903516	AB_2536183	1:300

Table 3. Quantification of EGFP^{Vgat}-labeled TH-immunoreactive neurons from *Vgat-cre;L10-Egfp* mouse brain tissue

Brain region[1]	Abbrev.[2]	*ARA* Level[3]	Number of neurons[4]		
			TH-ir	EGFP^{Vgat} + TH-ir[5]	Coloc.[6] (%)
Periventricular zone					
Supraoptic nucleus	SO	56–63	0[7]	0	
Accessory supraoptic group	ASO		n/a[8]	n/a	
Paraventricular hypothalamic nucleus					
Magnocellular division					
Anterior magnocellular part	PVHam		n/a	n/a	
Medial magnocellular part	PVHmm	60–65	2 ± 1	1 ± 1	
Posterior magnocellular part					
Lateral zone	PVHpml	60–65	0	0	
Medial zone	PVHpmm	63	0	0	
Parvicellular division					
Anterior parvicellular part	PVHap	56–59	37 ± 5	33 ± 6	90
Dorsal zone	PVHmpd	60–66	5 ± 2	3 ± 2	63
Periventricular part	PVHpv	56–65	3 ± 2	2 ± 1	60
Periventricular hypothalamic nucleus					
Anterior part	PVa	59–61	8 ± 4	6 ± 4	90
Intermediate part	PVi[9]	62–64	7 ± 1	6 ± 1	91
		65–67	27 ± 4	23 ± 3	87
		68–74	4 ± 2	3 ± 1	84
Arcuate hypothalamic nucleus	ARH[9]	65–67	5 ± 3	4 ± 3	73
		68–71	85 ± 18	74 ± 16	87
		72–74	27 ± 9	23 ± 9	88
Periventricular region					
Anteroventral preoptic nucleus	ADP	51–53	0	0	
Anterior hypothalamic area	AHA		n/a	n/a	
Anteroventral preoptic nucleus	AVP	50–54	1 ± 1	1 ± 1	
Anteroventral periventricular nucleus	AVPV	51–53	5 ± 4	1 ± 0	13
Dorsomedial nucleus of the hypothalamus					
Anterior part	DMHa[9]	67–69	29 ± 8	27 ± 8	92
		70–74	5 ± 3	4 ± 2	93
Posterior part	DMHp	70–74	11 ± 3	9 ± 3	81
Ventral part	DMHv	71–74	10 ± 2	9 ± 2	87
Median preoptic nucleus	MEPO		n/a	n/a	
Medial preoptic area	MPO[9]	50–55	9 ± 5	9 ± 4	98
		56–58	4 ± 3	3 ± 2	73
Vascular organ of the lamina terminalis	OV		n/a	n/a	
Posterodorsal preoptic nucleus	PD		0	0	
Parastrial nucleus	PS		0	0	
Suprachiasmatic preoptic nucleus	PSCH		n/a	n/a	
Periventricular hypothalamic nucleus					

Brain region[1]	Abbrev.[2]	*ARA* Level[3]	Number of neurons[4]		
			TH-ir	EGFP^{Vgat} + TH-ir[5]	Coloc.[6] (%)
Posterior part	PVp	75–79	8 ± 2	5 ± 2	72
Preoptic part	PVpo	54–66	54 ± 4	50 ± 5	93
Subparaventricular zone	SBPV	60–63	32 ± 1	30 ± 0	93
Subfornical organ	SFO		n/a	n/a	
Ventrolateral preoptic nucleus	VLPO	53–55	0	0	
Hypothalamic medial zone					
Anterior hypothalamic nucleus					
Anterior part	AHNa	58–64	0	0	
Central part	AHNc	59–64	1 ± 1	1 ± 0	
Dorsal part	AHNd		n/a	n/a	
Posterior part	AHNp	63–66	6 ± 1	6 ± 1	88
Mammillary body					
Lateral mammillary nucleus	LM	78–81	0	0	
Medial mammillary nucleus	MM	79–82	0	0	
Supramammillary nucleus					
Lateral part	SUMl	78–82	4 ± 2	0	0
Medial part	SUMm	78–82	6 ± 6	0	0
Tuberomammillary nucleus					
Dorsal part	TMd	75–77	0	0	
Ventral part	TMv	77–79	0	0	
Medial preoptic nucleus					
Central part	MPNc	53–55	0	0	
Lateral part	MPNl	54–58	1 ± 0	1 ± 0	
Medial part	MPNm	54–58	3 ± 1	1 ± 0	57
Dorsal premammillary nucleus	PMd				
Ventral premammillary nucleus	PMv				
Paraventricular hypothalamic nucleus, descending division					
Dorsal parvicellular part	PVHdp	60–65	0	0	
Forniceal part	PVHf		n/a	n/a	
Lateral parvicellular part	PVHlp	66	4 ± 2	4 ± 2	95
Medial parvicellular part, ventral zone	PVHmpv	64–65	0	0	
Ventromedial hypothalamic nucleus					
Anterior part	VMHa	65–66	0	0	
Central part	VMHc	67–73	1 ± 1	1 ± 1	
Dorsomedial part	VMHdm	67–71	0	0	
Ventrolateral part	VMHvl	66–73	0	0	
Hypothalamic lateral zone					
Lateral hypothalamic area	LHA	59–79	15 ± 11	6 ± 5	37
Lateral preoptic area	LPO	50–59	1 ± 1	1 ± 1	
Posterior hypothalamic nucleus	PH	70–82	8 ± 4	1 ± 0	12

Brain region[1]	Abbrev.[2]	*ARA* Level[3]	Number of neurons[4]		
			TH-ir	EGFP^{Vgat} + TH-ir[5]	Coloc.[6] (%)
Preparasubthalamic nucleus	PST		n/a	n/a	
Parasubthalamic nucleus	PSTN	75–78	8 ± 5	2 ± 1	18
Retrochiasmatic area	RCH		n/a	n/a	
Subthalamic nucleus	STN	75–78	8 ± 4	2 ± 2	30
Tuberal nucleus	TU	65–75	8 ± 4	3 ± 1	43
Zona incerta	ZI[9]	61–66	0	0	
		67–69	86 ± 19	86 ± 18	100
		70–83	4 ± 1	2 ± 1	57
Dopaminergic group	ZIda	67–69	10 ± 5	10 ± 5	100
Fields of Forel	FF	78–79	1 ± 1	0	

[1] Organization of brain regions based on hierarchical structure presented by the *Allen Reference Atlas* (*ARA*; Allen Institute for Brain Science, 2011).

[2] Nomenclature and atlas level based on the *ARA* (Dong, 2008).

[3] Each brain region may span several atlas levels.

[4] The total number of tyrosine hydroxylase-immunoreactive (TH-ir) neurons counted bilaterally from parcellated brain regions. Data are reported as mean ± SEM (n = 3 mice), rounded to nearest whole number. Number of neurons reported is corrected for oversampling using the Abercrombie formula $P = A(M/(L+M))$ (Abercrombie, 1946), where P is the corrected number of neurons counted, A is the original number of neurons counted, M is the mean tissue thickness (20 μm), L is the mean cell diameter (in μm). The cell diameter may vary between each parcellated hypothalamic region, thus a distinct Abercrombie correction factor is applied for each respective region.

[5] Quantification of TH-ir neurons that coexpress native EGFP fluorescence (EGFP^{Vgat}) in TH-ir neurons.

[6] Percentage of TH-ir neurons that colocalized (Coloc.) with EGFP-f indicate the proportion of GABAergic TH neurons. No value will be provided if the mean of two or less than two TH-ir neurons was counted.

[7] Parcellated brain regions that did not contain a TH-ir neuron.

[8] Data are not available (n/a) from brain regions that either did not emerge following Nissl-based parcellations or were not parcellated in the *ARA*.

[9] Distribution of TH-ir neuron within this region revealed noticeable breakpoints or clustering within *ARA* levels.

General Discussion

In this dissertation, I explored the utility of Nissl-based analysis to clarify elements of a 'parts list' and 'wiring diagram' of brain regions implicated in feeding. Both chapters demonstrated that Nissl boundaries can be used to accurately and precisely describe distributions of traced connections and hypothalamic cell types. In Chapter 1, I clarified the existence of mPFC projections to the ventral medial thalamic nucleus, which can easily be confused for the zona incerta (ZI) when using other atlas registration methods. mPFC projections also supported a boundary between an anterior region of the LHA and its cell-sparse dorsal region at approximately −2.00 mm from Bregma. Nissl interpretations in chapter 2 allowed us to suggest a revised nomenclature given the finding that tyrosine hydroxylase neurons in the ZI were not found in the structure called the ZI "dopaminergic group." This revision also poses a question as to the identity of this compact group of small cells. It is clear, then, that expert mapping with Nissl-based interpretation is a valuable strategy for refining a parts list of the CNS and producing reliable wiring diagrams.

A major goal of the Khan lab is to describe spatial distributions of neuropeptides and brain region connections that are relevant to feeding behaviors. In that regard, it is important to consider whether the present work can be insightful toward an understanding of feeding behaviors. My investigations on mPFC connections were inspired by two reports that showed pharmacological stimulations of circumscribed mPFC areas can produce hyperphagia (Mena et al., 2011; Castro and Berridge, 2017). However, an astute reader would notice that the injection sites I examined here were not among the mPFC feeding and hedonic 'hotspots' described in those studies. The prelimbic area (PL), wedged between the ACAd and ILA, produced the strongest enhancement of feeding. Some of my additional work from the Khan lab aims to describe PL connections across the rostrocaudal axis (**Fig. 4**; also see Appendix); comparison of PL and ILA connections can be useful for contextualizing some behavioral findings.

Subsequent investigations of mPFC-driven hyperphagia have shown that the lateral hypothalamic area (LHA) was critical for this effect (Mena et al., 2013). mPFC-driven hyperphagia was also shown to correlate with increased Fos expression in a part of LHA dorsal-medial to the fornix. It is important to note that ILA projections do not terminate in this quadrant of LHA, ILA projections are primarily lateral to the fornix. Instead, the dorsal-medial quadrant is specifically targeted by axons originating from the caudal PL (**Figure 4**; for a wider-scale view of the topography of these PL connections in the forebrain, please consult the Appendix in this dissertation, which includes additional data). This observation is supported by retrograde tracer experiments in the dorsal-medial LHA (Hahn and Swanson, 2012) and dorsal-lateral LHA (unpublished observations by Toccoli et al., 2021). Taken together, mPFC projections to LHA appear to form some degree of medial-lateral selectivity, but the functional significance is less clear.

There is some work, primarily using Fos localization, that suggests medial-lateral specialization in the LHA. Hypocretin neurons in the dorsomedial, but not lateral LHA, have been associated with arousal (Estabrooke et al., 2001). Fos counts in this region increased as a function of behavior wakefulness, indexed by assessing of sleep/wake cycles, sleep deprivation, and administration of the psychostimulant methamphetamine. Caffeine and fear conditioning were also shown to specifically increase Fos counts in the dorsomedial LHA (Murphy et al., 2003; Sharko et al., 2017). We can tentatively propose that dorsomedial LHA contributes to the arousal state generally. The dorsolateral LHA, by contrast, is activated by cues that signal rewards such as drugs or food (Harris et al., 2005; Richardson and Aston-Jones, 2012). Recent work demonstrated a lateral LHA contribution to learning and prediction of rewards (Sharpe et al., 2017). Efforts to describe an anatomical basis for this medial-lateral specialization have pointed to more complexity (Iyer et al., 2018). Description of medial vs. lateral may be useful as a starting point, but such simplifications may also preclude a better understanding of the LHA. This conclusion is difficult to escape when we consider work that examines the LHA across

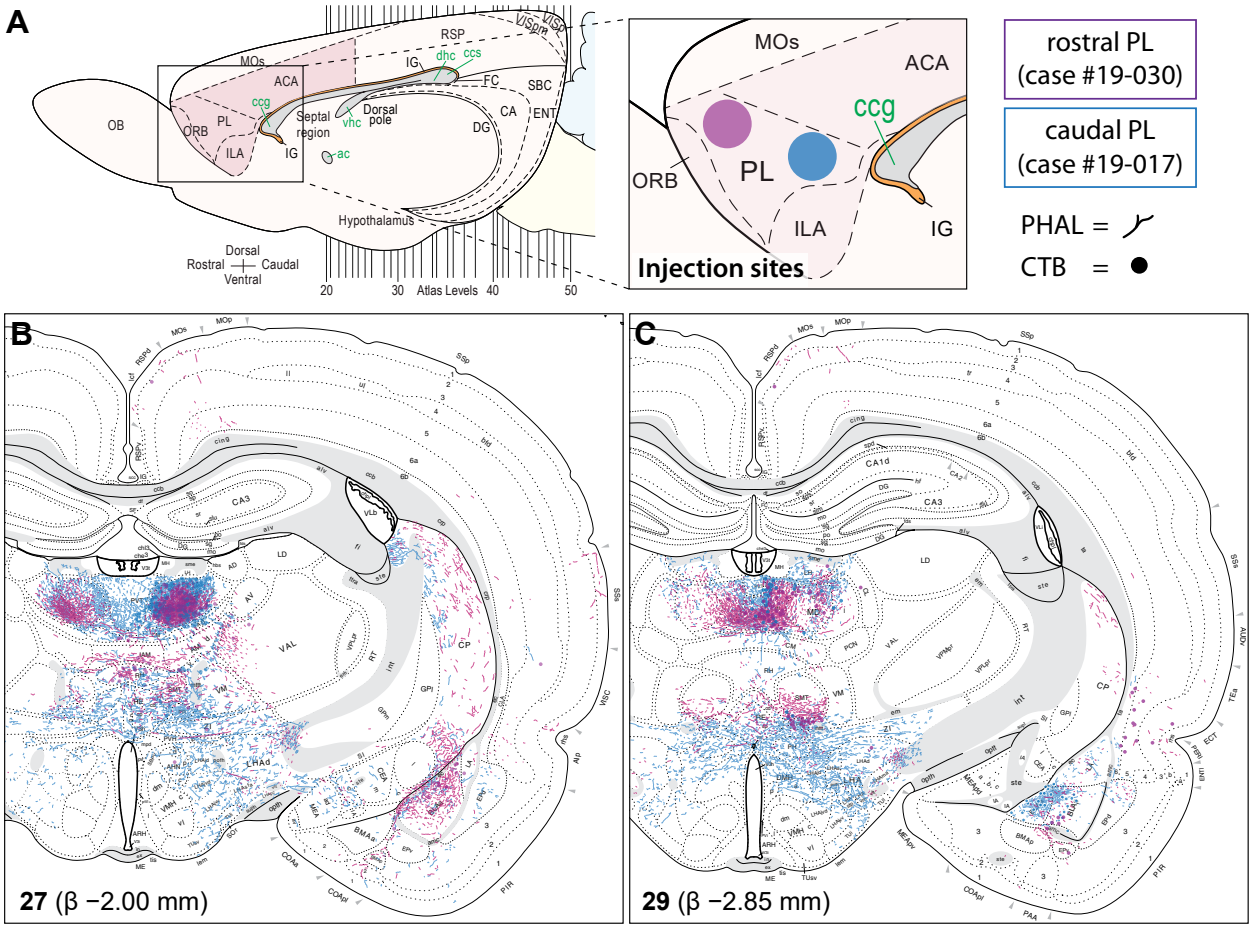

Figure 4. Analysis of prelimbic connections with diencephalon. (**A**) Schematic representation of injection site placements. Circle placements indicate PHAL and CTB injection sites in rostral (purple) and caudal (blue) parts of the prelimbic area. Sagittal templates were adopted from Swanson and Hahn (2020). (**B** and **C**) Mapped prelimbic connections in coronal atlas levels containing the lateral hypothalamic area. Lines represent PHAL-labeled axons and dots indicate individual CTB-labeled neurons. Color-coding of rostral and caudal prelimbic connections follow those used in (A).

three-dimensions, such as that presented here.

The role of dopaminergic neurons in the hypothalamus is much less clear. Chapter 2 showed that these neurons were mainly localized in hypothalamic regions adjacent to the third ventricle with the ZI and posterior hypothalamic nucleus being the main exceptions. These neurons primarily co-express proteins for vesicular transport of GABA, so any work that investigates the role of hypothalamic dopaminergic neurons would be incomplete without also assessing the role of GABA.

Contributions of hypothalamic dopaminergic neurons toward feeding behaviors has not been well established, but there is evidence to suggest a role. Earlier work has

shown increased extracellular dopamine concentrations in the LHA following overnight fasting (Meguid et al., 2000). Recently, stimulation of dopaminergic neurons in the arcuate hypothalamic nucleus (ARH) was shown to produce an orexigenic effect and these neurons were excited by circulating ghrelin (Zhang and van den Pol, 2016).

Zhang and van den Pol (2017) also showed that stimulation of ZI GABA neurons resulted in a pronounced binge-eating effect. We showed that dopaminergic neurons in the ZI were exclusively GABAergic, so it is important to consider whether the ZI dopaminergic neurons contribute to feeding behaviors. Of the ZI outputs, the projections to the paraventricular thalamus (PVT) were able to stimulate feeding (Zhang and van den Pol, 2017). Our preliminary findings using Cre-depenedent anterograde tracing of ZI Th projections has confirmed dopaminergic projections to the PVT. This conclusion is supported by earlier work that showed CTB injections to the PVT retrogradely labeled ZI neurons that co-localized tyrosine hydroxylase (Li et al., 2014). Nevertheless, whether dopamine from the ZI contributes to feeding has not been established.

The PVT is an important node to consider further for our discussion of feeding. Both ZI and dorsomedial LHA send projections to the PVT (Li et al., 2014), and the PVT sends dense projections to the nucleus accumbens (ACB) shell and mPFC (Vertes and Hoover, 2008). Stimulation of ZI axons in the PVT was shown to produce real-time place preference (Zhang and van den Pol, 2017), so it is possible that PVT neurons modulate hedonic processes via projections to mPFC and ACB. In light of this, it is worth noting that PVT axons in mPFC and ACB (Vertes and Hoover, 2008) are remarkably well-aligned with hedonic ‘hotspots’ described with DAMGO infusions (Peciña and Berridge, 2005; Castro and Berridge, 2017). Future work, including elaborations of some preliminary tract-tracing work on these regions that we conducted in the Khan laboratory (Negishi et al., 2022), should aim to determine whether ZI- and mPFC-evoked feeding involve the separable or identical networks.

Concluding Remarks

Work presented here offer several directions for follow-up studies. First, it is unclear why mPFC forms widespread reciprocal connections with thalamus. This is especially important given that most mPFC connections are formed with the thalamus. I also demonstrated mPFC connections with specific subdivisions of the lateral hypothalamic zone. Both the anatomy of connections and functional properties of these subdivisions are not well described. Our collaborative work with the Chee lab revealed that the A13 dopaminergic population is exclusively GABAergic. Follow-up work should be done to describe its full connectivity as it might differ from other ZI cell types, and experiments should aim to uncouple GABA and dopamine to understand their separate contributions to ZI functions.

Finally, the reader is spared from the sheer tedium and personnel-hours that went into producing structural maps and the training needed to interpret Nissl architecture. I hope that this work can be taken as a set of best practices for the validation of atlas registration, the use of transgenic animals, and reporting of anatomical data. I also hope that the reader is convinced of the value this type of work has in brain research, but some technical refinements are necessary for this to be viable. It is imperative to continue developing ways to automate the labor-intensive aspects of our work (identification of hybridized or traced cells and manual tracing of fibers). Automated atlas registration is another promising route, but all caveats concerning the use of black boxes apply. I worry that a shortage of qualified anatomists will leave the task of validation to the intuitions of engineers. The best way to avoid this is by introducing formal anatomical training as part of brain research curricula in graduate school.

Bibliography

Barbier, M., Fellmann, D., Risold, P.-Y. (2018). Morphofunctional organization of the connections from the medial and intermediate parts of the central nucleus of the amygdala into distinct divisions of the lateral hypothalamic area in the rat. *Front Neurol, 9*, 688. https://doi.org/10.3389/fneur.2018.00688

Brodmann, K. (1909). *Vergleichende Lokalisationslehre der Grosshirnrinde in ihren Prinzipien Dargestellt auf Grund des Zellenbaues* (Barth, Leipzig).

Brown, D., Altermatt, M., Dobreva, T., Chen, S., Wang, A., Thomson, M., Gradinaru, V. (2021). Deep parallel characterization of AAV tropism and AAV-mediated transcriptional changes via single-cell RNA sequencing. *Front Immunol, 12*, 730825. https://doi.org/10.3389/fimmu.2021.730825

Castro, D. C., Berridge, K. C. (2017). Opioid and orexin hedonic hotspots in rat orbitofrontal cortex and insula. *Proc Natl Acad Sci U S A, 114*(43):E9125–E9134. https://doi.org/10.1073/pnas.1705753114

Callaway, E. M., Luo, L. (2015). Monosynaptic circuit tracing with glycoprotein-deleted rabies virus. *J Neurosci, 35*(24), 8979–8985. https://doi.org/10.1523/jneurosci.0409-15.2015

Dong, H. W. (2008). *The Allen reference atlas: A digital color brain atlas of the C57BL/6J male mouse*. Hoboken, NJ: John Wiley & Sons.

Estabrooke, I. V., McCarthy, M. T., Ko, E., Chou, T. C., Chemelli, R. M., Yanagisawa, M., Saper, C. B., Scammell, T. E. (2001). Fos expression in orexin neurons varies with behavioral state. *J Neurosci, 21*(5),1656–1662. https://doi.org/10.1523/jneurosci.21-05-01656.2001

Gurdjian, E.S. (1927). The diencephalon of the albino rat. *J Comp Neurol, 43*, 1–114.

Kelley, A. E., Berridge, K. C. (2002). The neuroscience of natural rewards: relevance to addictive drugs. *J Neurosci, 22*(9), 3306–3311. https://doi.org/10.1523/

jneurosci.22-09-03306.2002

Khan, A. M. (2013). Controlling feeding behavior by chemical or gene-directed targeting in the brain: what's so spatial about our methods?. *Front Syst Neurosci, 7*, 1–49. https://doi.org/10.3389/fnins.2013.00182

Kirst, C., Skriabine, S., Vieites-Prado, A., Topilko, T., Bertin, P., Gerschenfeld, G., Verny, F., Topilko, P., Michalski, N., Tessier-Lavigne, M., Renier, N. (2020). Mapping the fine-scale organization and plasticity of the brain vasculature. *Cell, 180*(4), 780–795. https://doi.org/10.1016/j.cell.2020.01.028

Hahn, J. D., Swanson, L. W. (2012). Connections of the lateral hypothalamic area juxtadorsomedial region in the male rat. *J Comp Neurol, 520*(9),1831–1890. https://doi.org/10.1002/cne.23064

Harris, G. C., Wimmer, M., Aston-Jones, G. (2005). A role for lateral hypothalamic orexin neurons in reward seeking. *Nature, 437*(7058),556–559. https://doi.org/10.1038/nature04071

Hintiryan, H., Foster, N. N., Bowman, I., Bay, M., Song, M. Y., Gou, L., Yamashita, S., Bienkowski, M. S., Zingg, B., Zhu, M., Yang, X. W., Shih, J. C., Toga, A. W., Dong, H.-W. (2016). The mouse cortico-striatal projectome. *Nat Neurosci 19*(8), 1100–1114. https://doi.org/10.1038/nn.4332

Iyer, M., Essner, R. A., Klingenberg, B., Carter, M. E. (2018). Identification of discrete, intermingled hypocretin neuronal populations. *J Comp Neurol, 526*(18),2937–2954. https://doi.org/10.1002/cne.24490

Li, S., Shi, Y., Kirouac, G. J. (2014). The hypothalamus and periaqueductal gray are the sources of dopamine fibers in the paraventricular nucleus of the thalamus in the rat. *Front Neuroanat, 8*,136. https://doi.org/10.3389/fnana.2014.00136

Lein, E. S., *et al*. (2007). Genome-wide atlas of gene expression in the adult mouse brain. *Nature, 445*(7124), 168–176. https://doi.org/10.1038/nature05453

MacLean, P. D. (1952). Some psychiatric implications of physiological studies on

frontotemporal portion of limbic system (visceral brain). *Electroencephalogr Clin Neurophysiol, 4*(4), 407–418. https://doi.org/10.1016/0013-4694(52)90073-4

Madangopal, R. *et al*. (2022). Incubation of palatable food craving is associated with brain-wide neuronal activation in mice. *Proc Natl Acad Sci U S A, 119*(45), e2209382119. https://doi.org/10.1073/pnas.2209382119

Meguid, M. M., Fetissov, S. O., Varma, M., Sato, T., Zhang, L., Laviano, A., Rossi-Fanelli, F. (2000). Hypothalamic dopamine and serotonin in the regulation of food intake. *Nutrition, 16*(10),843–857. https://doi.org/10.1016/s0899-9007(00)00449-4

Mena, J. D., Sadeghian, K., Baldo, B. A. (2011). Induction of hyperphagia and carbohydrate intake by μ-opioid receptor stimulation in circumscribed regions of frontal cortex. *J Neurosci, 31*(9),3249–60. https://doi.org/10.1523/jneurosci.2050-10.2011

Mena, J. D., Selleck, R. A., Baldo, B. A. (2013). Mu-opioid stimulation in rat prefrontal cortex engages hypothalamic orexin/hypocretin-containing neurons, and reveals dissociable roles of nucleus accumbens and hypothalamus in cortically driven feeding. *J Neurosci, 33*(47),18540–52. https://doi.org/10.1523/jneurosci.3323-12.2013

Millhouse, O. E. (1969). A Golgi study of the descending medial forebrain bundle. *Brain Res, 15*(2), 341–363. https://doi.org/10.1016/0006-8993(69)90161-9

Murphy, J. A., Deurveilher, S., Semba, K. (2003). Stimulant doses of caffeine induce c-FOS activation in orexin/hypocretin-containing neurons in rat. N*euroscience, 121*(2),269–275. https://doi.org/10.1016/s0306-4522(03)00461-5

Negishi K, Montes LP, Ponce M, Wells Y, Khan AM. (2020/21). Comparison of rostral and caudal prelimbic cortical connections with the forebrain in the adult male rat. Program No. 254.05. Presented at the *Global Connectome Meeting of the Society for Neuroscience*. Online, Jan 11–13.

Negishi K, Montes LP, Oliveros C, Ponce MS, Wells YC, Khan AM. (2021). Standardized mapping and high-spatial resolution analysis of rostral and caudal prelimbic cortical connections in the endbrain (forebrain) of the adult male rat. Presented at

the Annual Meeting of the Society for Neuroscience. Online, Nov 8–11. [*Session P648: Central Circuits for Feeding: Anatomy and Function*].

Negishi K, Navarro VI, Guerra-Ruiz J, Sotelo D, Toccoli A, Khan AM. (2022). A topographically-defined cortico-striato-pallidal module with convergent projections to the lateral hypothalamic area. Presented at the *Annual Meeting of the Society for Neuroscience*, San Diego, CA, Nov 12–16.

Oh, S. W. *et al*. (2014). A mesoscale connectome of the mouse brain. *Nature, 508*(7495), 207–214. https://doi.org/10.1038/nature13186

Paxinos, G., Watson, C. (2014). *The Rat Brain in Stereotaxic Coordinates* (7th ed.). San Diego: Elsevier Academic Press.

Peciña, S., Berridge, K. C. (2005). Hedonic hot spot in nucleus accumbens shell: where do mu-opioids cause increased hedonic impact of sweetness?. *J Neurosci, 25*(50),11777–11786. https://doi.org/10.1523/jneurosci.2329-05.2005

Renier, N. *et al*. (2016). Mapping of brain activity by automated volume analysis of immediate early genes. *Cell, 165*(7), 1789–1802. https://doi.org/10.1016/j.cell.2016.05.007

Richardson, K. A., Aston-Jones, G. (2012). Lateral hypothalamic orexin/hypocretin neurons that project to ventral tegmental area are differentially activated with morphine preference. *J Neurosci, 32*(11),3809–3817. https://doi.org/10.1523/jneurosci.3917-11.2012

Sharko, A. C., Fadel, J. R., Kaigler, K. F., Wilson, M. A. (2017). Activation of orexin/hypocretin neurons is associated with individual differences in cued fear extinction. *Physiol Behav, 178*,93–102. https://doi.org/10.1016/j.physbeh.2016.10.008

Sharpe, M. J., et al. (2017). Lateral hypothalamic GABAergic neurons encode reward predictions that are relayed to the ventral tegmental area to regulate learning. *Curr Biol, 27*(14),2089–2100.e5. https://doi.org/10.1016/j.cub.2017.06.024

Simmons, D. M., Swanson, L. W. (2009). Comparing histological data from different brains: sources of error and strategies for minimizing them. *Brain Res Rev, 60*(2),349–367.

https://doi.org/10.1016/j.brainresrev.2009.02.002

Sun, L. *et al*. (2019). Differences in neurotropism and neurotoxicity among retrograde viral tracers. *Mol Neurodegener, 14*(1), 8. https://doi.org/10.1186/s13024-019-0308-6

Swanson, L. W. (2018). Brain maps 4.0—Structure of the rat brain: An open access atlas with global nervous system nomenclature ontology and flatmaps. *J Comp Neurol, 526*(6), 935–943. https://doi.org/10.1002/cne.24381

Swanson, L. W., Hahn, J. D. (2020). A qualitative solution with quantitative potential for the mouse hippocampal cortex flatmap problem. *Proc Natl Acad Sci U S A, 117*(6),3220–3231. https://doi.org/10.1073/pnas.1918907117

Tervo, D. G. R. *et al*. (2016). A designer AAV variant permits efficient retrograde access to projection neurons. *Neuron, 92*(2), 372–9382. https://doi.org/10.1016/j.neuron.2016.09.021

Toccoli, A., Sotelo, D., Navarro, V. I., Negishi, K., Khan, A. M. (2021). Standardized mapping and a high-spatial resolution comparison of the inputs and outputs of the anterior and dorsal regions of the lateral hypothalamic area in the adult male rat using the atlas framework of *Brain Maps 4.0*. Program No. P648.02. Poster presented at the Society for Neuroscience, virtual meeting.

Vertes, R. P., Hoover, W. B. (2008). Projections of the paraventricular and paratenial nuclei of the dorsal midline thalamus in the rat. *J Comp Neurol, 508*(2),212–237. https://doi.org/10.1002/cne.21679

Volkow, N. D., Wise, R. A. (2005). How can drug addiction help us understand obesity?. *Nat Neurosci, 8*(5), 555–560. https://doi.org/10.1038/nn1452

Watts, A. G., Kanoski, S. E., Sanchez-Watts, G., Langhans, W. (2022). The physiological control of eating: signals, neurons, and networks. *Physiol Rev, 102*(2), 689–813. https://doi.org/10.1152/physrev.00028.2020

Wickersham, I. R. *et al*. (2007). Monosynaptic restriction of transsynaptic tracing from single, genetically targeted neurons. *Neuron, 53*(5), 637–647. https://doi.

org/10.1016/j.neuron.2007.01.033

Wang, Q. et al. (2020). The Allen Mouse Brain Common Coordinate Framework: A 3D reference atlas. *Cell, 181*(4), 936–953. https://doi.org/10.1016/j.cell.2020.04.007

Zhang, X., van den Pol, A. N. (2016). Hypothalamic arcuate nucleus tyrosine hydroxylase neurons play orexigenic role in energy homeostasis. *Nat Neurosci, 19*(10),1341–1347. https://doi.org/10.1038/nn.4372

Zhang, X., van den Pol, A. N. (2017). Rapid binge-like eating and body weight gain driven by zona incerta GABA neuron activation. *Science, 356*(6340),853–859. https://doi.org/10.1126/science.aam7100

Appendix

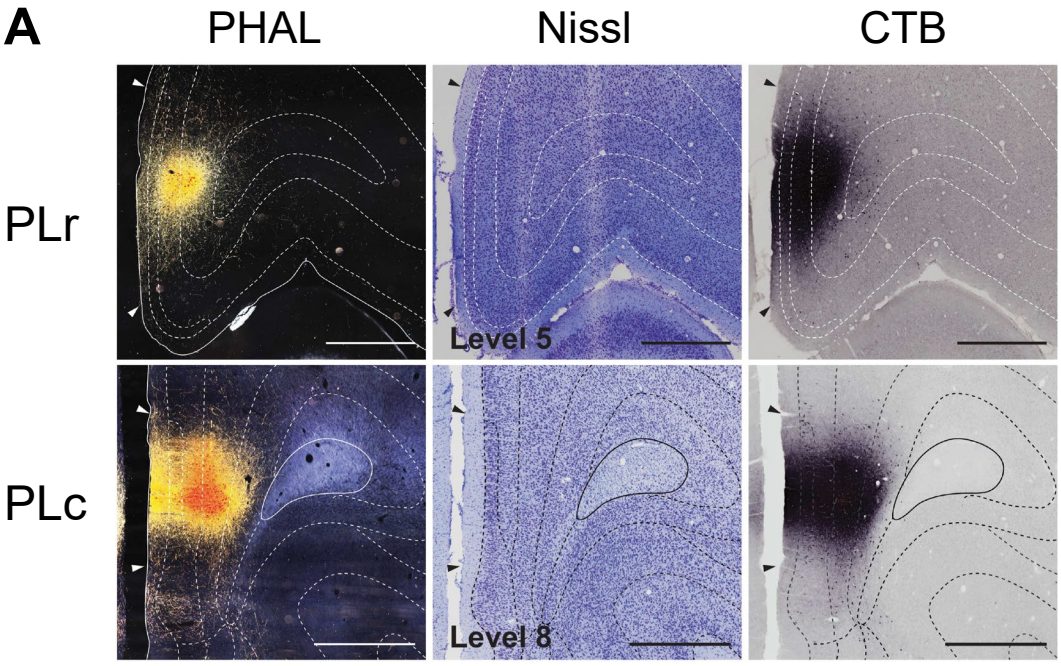

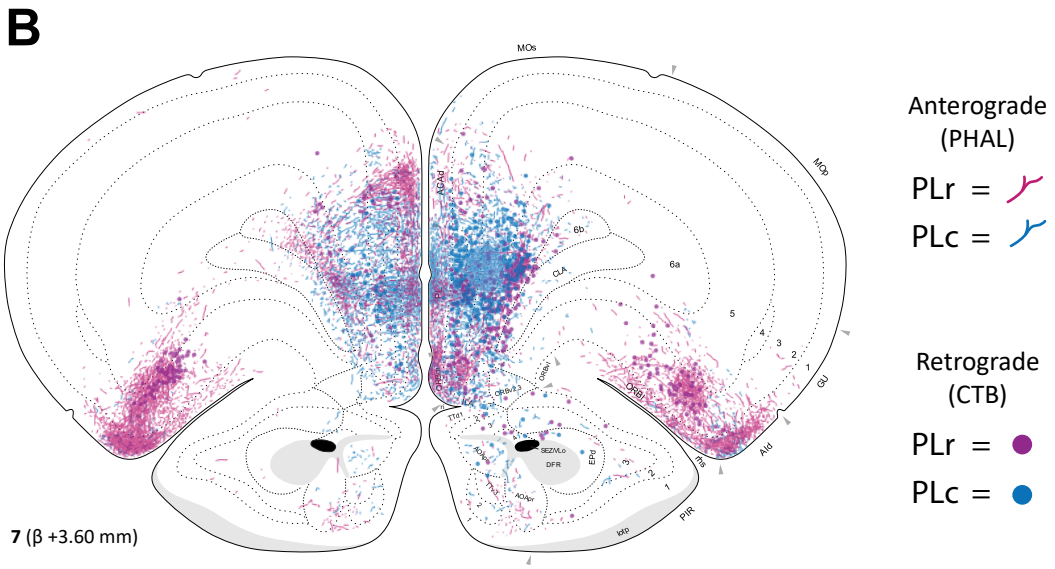

Comparison of input/output connections from rostral (PLr) and caudal (PLc) parts of the prelimbic area. (**A**) Photomicrographs showing injection sites in the prelimbic area. (**B**–**H**) Mapped connections of PLr (magenta; experiment # 19-030) and PLc (blue; experiment #19-017) throughout the forebrain. PHAL distributions are represented with lines and CTB neurons are shown as dots. Figures shown here are adapted from Negishi et al. (2020/21; 2021).

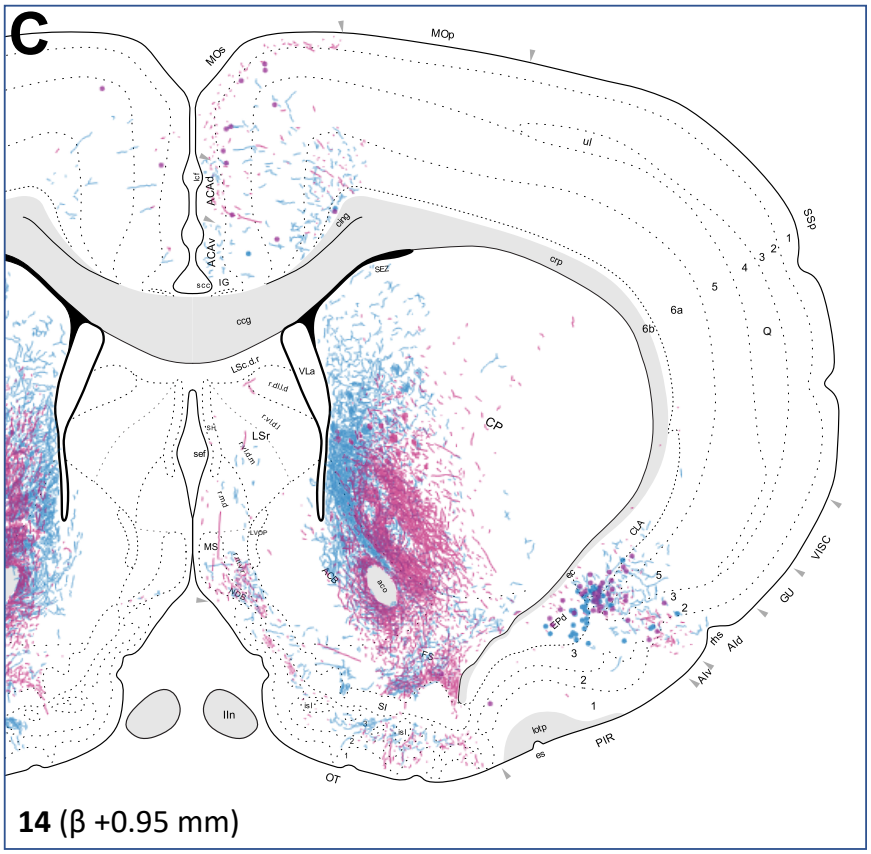

14 (β +0.95 mm)

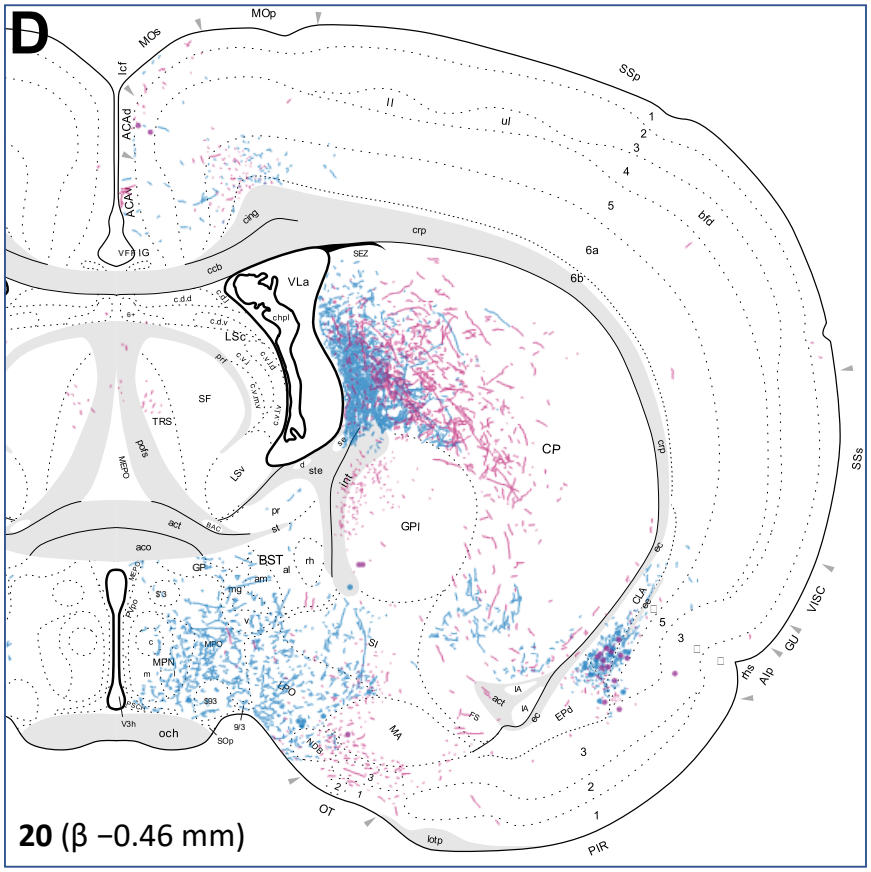

20 (β −0.46 mm)

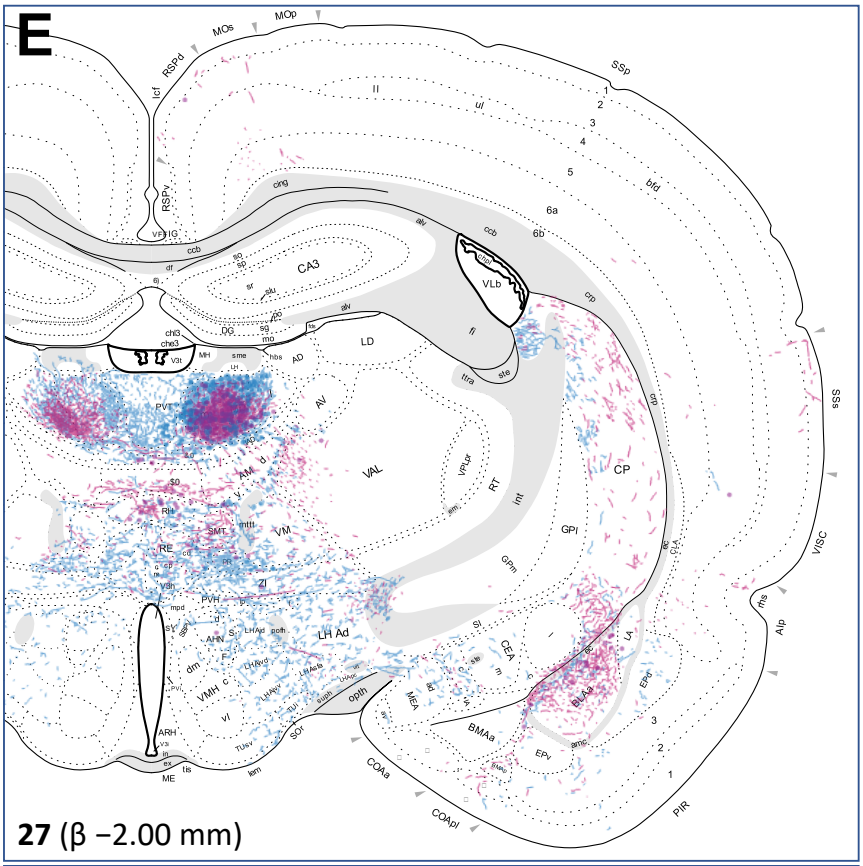

27 (β −2.00 mm)

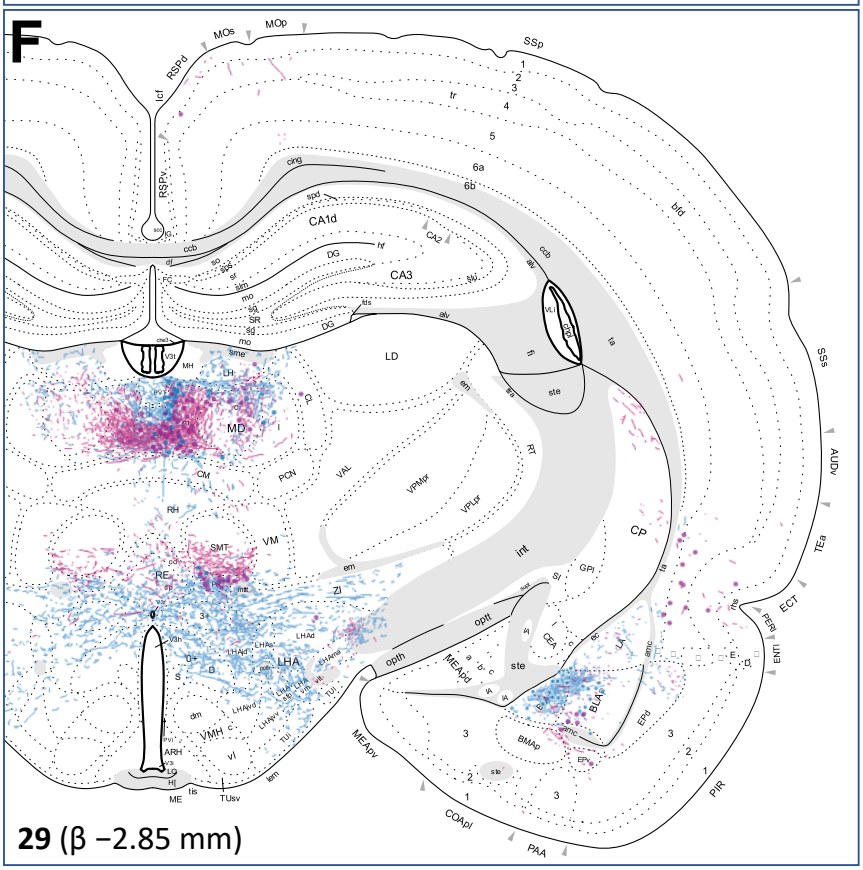

29 (β −2.85 mm)

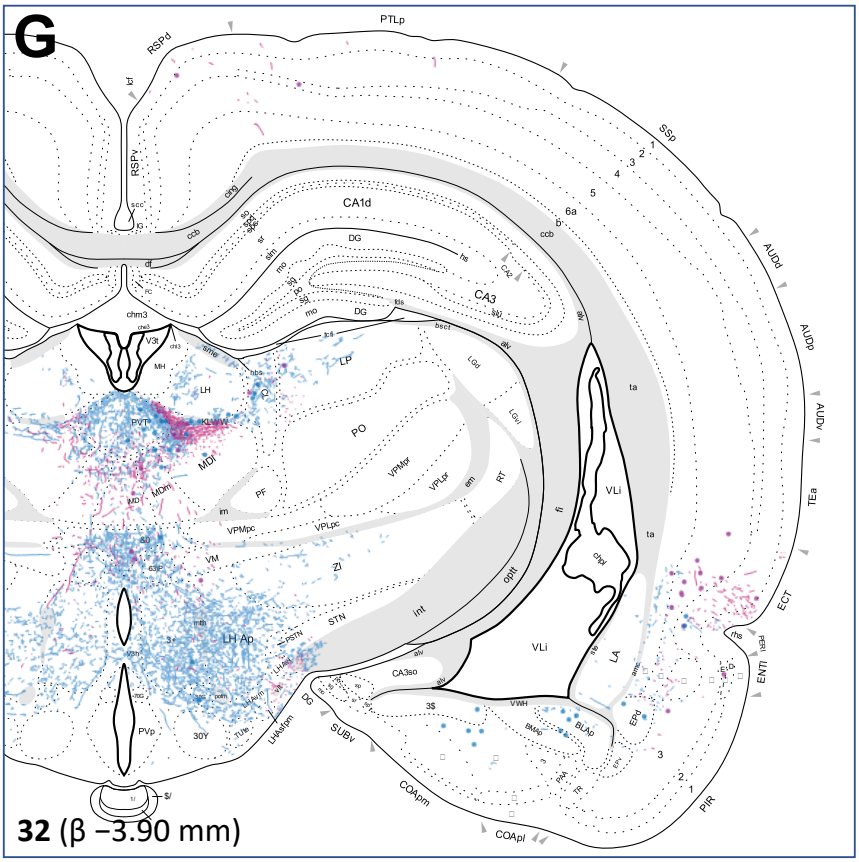
G
PTLp
RSPd
RSPv
CA1d
DG
CA3
LP
PO
VPMpr
VPLpr
VPMpc
VPLpc
VM
ZI
STN
int
VLi
LA
BLAp
CA3so
SUBv
COApm
COApl
PIR
ECT
ENTl
AUDd
AUDp
AUDv
TEa
32 (β −3.90 mm)

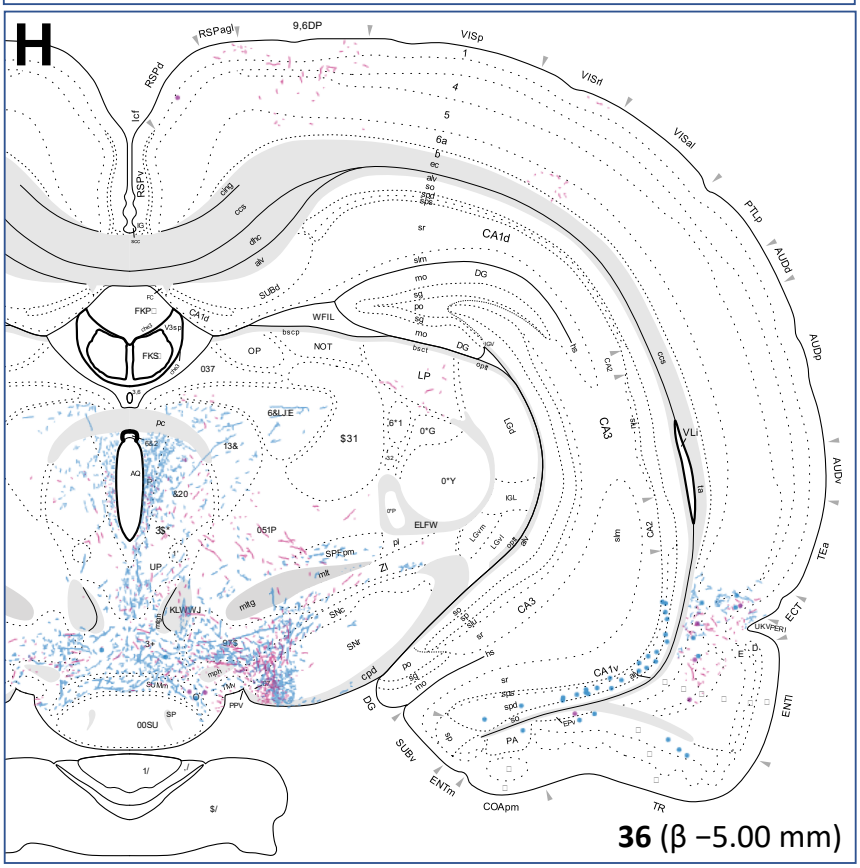
H
RSPagl
9,6DP
VISp
VISrl
VISal
PTLp
AUDd
AUDp
AUDv
TEa
ECT
ENTl
RSPd
RSPv
CA1d
SUBd
DG
CA3
LP
VLi
SUBv
ENTm
COApm
TR
36 (β −5.00 mm)

Vita

Kenichiro Negishi

Contact: lonestar.knegishi@gmail.com

My research interests center around the neural mechanisms of ‘wanting’ and ‘craving.’ The dynamics of these phenomena are best studied using the lens of addiction biology, so I am committed to gaining expertise in using animal models of addiction and relapse.

My graduate training was focused on using pathway tracing techniques to map neural connections in the rat. This amounts to almost a decade of experience in the use of atlas mapping techniques as well as surgical and histological skills necessary for high-resolution analysis of connections. Collaborative projects also allowed me to become familiar with the use of viruses and transgenic animals for atlas mapping in the mouse model using the Allen Reference Atlas. Through the course of my work I stumbled into a forebrain network, defined on the basis of structural connectivity, that includes cortical, striatal, pallidal, and diencephalic regions that were separately implicated in the wanting and craving associated with several motivated behaviors.

A long-term goal, and the subject of my independent research, is to formalize this structural ‘craving’ network and apply manipulations to probe its dynamics. I aim to receive training to use and develop behavioral models of relapse through my postdoctoral research. The Shaham lab is uniquely suited for this training given its leading role in the development of models used to study mechanisms of relapse. I hope to assist in developing models of relapse and become familiar with the conceptual and technical nuances of translational work that I can apply to my own research.